Rheological, Chemical and Mechanical Properties of Cementitious Materials with Nanoclays and Diutan Gum

Siwei Ma

Submitted in partial fulfillment of the

requirements for the degree of

Doctor of Philosophy

in the Graduate School of Arts and Sciences

COLUMBIA UNIVERSITY

2018

ABSTRACT

Rheological, Chemical and Mechanical Properties of Cementitious Materials with Nanoclays and Diutan Gum

Siwei Ma

Cement has three sequential states in most applications: fluid, setting and hardened. This thesis focuses on the effect of nanoclays and diutan gum on rheological, chemical and mechanical properties corresponding to the three states.

Water transport properties are critically important in many applications, such as oil well cementing and 3D concrete printing. The effect of nanoclays and diutan gum on water transport properties of cement pastes were investigated. Bleeding, water retention under suction pressure, and evaporation under air flow were measured. The nanoclay was found to reduce bleeding but had no effect on water retention or evaporation. The diutan gum was found to reduce bleeding, improve water retention, and decrease evaporation loss. The rheological properties of the pastes and their interstitial solution were also characterized to resolve the mechanisms underlying the water transport behaviors. Good correlation between the measured rheological parameters and water transport properties was found.

In addition to water retention, the static yield stress build-up plays a major role in the successful oil well cementing and 3D concrete printing. Linear models are commonly used to describe the early structural build-up of cement-based materials. However, some studies have shown that there exists a faster non-linear phase before the linear phase. A simple non-linear thixotropy model is presented to describe the structural

build-up process. It was quantified using static yield stress and storage modulus, which are measured through the stress growth protocol and small amplitude oscillatory shear (SAOS) tests, respectively. The effect of pre-shear, rest condition and nanoclay and diutan gum on the build-up behavior are studied. The results showed distinctly different trends between static yield stress and storage modulus. This may be attributed to the two different structures of fresh cement pastes, i.e. floc structures and C-S-H structures, measured by the stress growth protocol and SAOS test, respectively.

Phase characterization of cement paste was performed through synchrotron x-ray diffraction technique. This allowed for real-time, in-situ measurements of x-ray diffraction patterns to be obtained, and subsequently the continuous formation and decomposition of select phases over time (up to 8 hours). Phases of interest included alite, ferrite, portlandite, ettringite, monosulfate, and jaffeite (crystalline form of calcium silicate hydrate). The effects of elevated temperatures at elevated pressure, as well as the effect of nanomaterial addition were investigated. Rate of conversion of ettringite to monosulfate increased with increasing temperature, and monosulfate became unstable when temperatures reached 85ºC. The synchrotron x-ray diffraction setup appeared to have captured the seeding effect of nano-sized attapulgite clays at 0.5% addition by mass of cement, where acceleration in the rate of formation of portlandite and jaffeite was observed.

Finally, the investigated system was upscaled from cement paste to cement mortar incorporating the fly ash and the slag. The effect of the nanoclays on the mechanical properties was evaluated in comparison with the carbon nanotube. Compressive strength and tensile strength were evaluated. Results indicated that although the nanoclays are utilized primarily as a rheological modifier, they can also enhance mechanical properties.

TABLE OF CONTENTS

LIST OF FIGURES

LIST OF TABLES

ACKNOWLEDGMENTS

First and foremost, I would like to express my sincere gratitude to my advisor Professor Shiho Kawashima for her guidance, support, and encouragement. Under your mentoring, I have an opportunity to enjoy the exploration of the research topics without worrying about losing direction and focus. I am thankful for your time, ideas, and funding to support me through the rough road to finish this thesis.

I wish to extend my gratitude to my Ph.D. defense committee, Dr. Nathan Tregger from GCP Applied Technology, Professor Kejin Wang at Iowa State University, and Professor Huiming Yin and Professor Hoe I. Ling at Columbia University for taking their valuable time to participate my defense and review this dissertation.

I am hugely appreciative to our group members. The group has been a source of friendships as well as good advice and collaboration. With a special mention to Dr. Ye Qian, it is always great fun to discuss questions with you. I would like to express my sincere gratitude to the postdoctoral researchers: Dr. Seungmin Lim and Dr. Sujin Lee for the cooperation and help in the lab. I would also like to thank Jumari Robinson, Akiva Goldstein, Augusta C. Uwamanzu-Nna, and Yu Xie for their help on the experimental work.

My special thanks also go to the Carleton Lab managers, Dr. Adrian Brugger and Dr. Liming Li, for their enormous support of my experimental work. I am also grateful to the scientists at GSECARS, University of Chicago: Dr. Yanbin Wang and Dr. Tony Yu. It was fantastic to have the opportunity to work my research in your facilities.

Finally, I would like to express my most sincere appreciation to my family for their love, care, and sacrifice. I can hardly imagine myself accomplishing anything without your selfless devotion and support. To my parents, words are incapable of adequately describe my gratefulness for all you have done for me. Thank you for always being there for me. To my wife, I can never thank you enough, for your love, encouragement.

Dedicated to my parents and wife.

CHAPTER ONE

1. INTRODUCTION

1.1. BACKGROUND

Cementitious materials can be considered as both old and new. The Romans used hydraulic cement as a binding material with aggregates (rock, ceramic tile, and brick rubble) to build structures like the Pantheon dome, aqueducts, and pier, which still stand today [1], as shown in Figure 1. However, the technology behind the hydraulic cement was lost for hundreds of years in the dark ages. It can also be considered as a new material since the "modern" Portland cement was invented in England in the mid-19th century. Now, cement has been one of the most widely used infrastructural materials in the world, of which about 4100 million metric tons are produced per year. With the progress in cement science and technology, the properties of cementitious materials (e.g., strength, ductility, durability, and flowability) can be tailored and enhanced to meet different application purposes, such as oil well cementing and 3D concrete printing.

Figure 1. Ancient Roman concrete in marine environment. (PHOTO CREDIT: J. P. Oleson)

Portland cement is made from various raw materials containing primarily lime oxide (C), silica dioxide (S) alumina oxide (A) and iron oxide (F). These materials interact with each other during the production process and form a series of complex compounds, which mainly include tricalcium silicate (C_3S), dicalcium silicate (C_2S), tricalcium aluminate (C_3A), and tetracalcium aluminoferrite (C_4AF). Note that the chemical composition is traditionally written in shorthanded oxide notation, as shown in parentheses.

The classification of cement usually depends on its mineralogical composition and particle size. In ASTM C150/C150M Standard Specification for Portland Cement, it has designated five types of Portland cement, designated Types I-V. Type I is a general use cement. American Petroleum Institute specification 10A categorize oil well cement, which is used in the petroleum industry, as eight classes (Class A through Class H). Among them, API Classes A, B, and C cement are comparable to ASTM Types I, II, and III cement respectively which could be used in wells with depths up to 1800 m while Class G and H cement are usually specified for deeper oil wells.

The cement hardens when reacted with water. This process, called cement hydration, is a complicated exothermal process involving several different chemical reactions, such as C-S-H and ettringite formation, ettringite and monosulfate transformation. The overall progress of hydration without regard to the action of individual chemical reactions can be monitored by calorimetry, as shown in Figure 2. The calorimetry plot of hydration over time indicates four periods. The first stage is initial dissolution of solids and ettringite (Aft) formation that begins immediately upon wetting. The second stage is called the dormant period. The third stage is called the acceleration period. The rate-controlling step of hydration during this period is related to the heterogeneous nucleation and growth of C–S–H. The last stage is the deceleration period in which a diffusion process controls the rate of hydration.

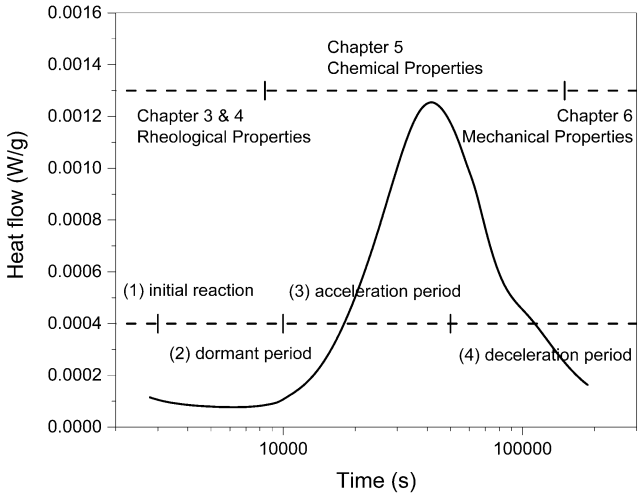

Figure 2. Representative hydration curves. The lower dashed line shows the four periods of cement hydration. The upper dashed line demonstrates the time range of each chapter of this dissertation.

1.2. MOTIVATION: OIL WELL CEMENTING

Cementing plays a critical role in the process of oil-well completion. Cement is pumped down the inside of the liner as a slurry and forced to come back up to fill the annular space between the liner and the borehole, as shown in Figure 3. The objective of cementing is to provide structural support and zonal isolation, which prevent gas migration between geological formations and prevent the escape of fluid to the surface. The failure of zonal isolation would cause loss of product, costly remedial jobs, and catastrophic blowouts like the deepwater horizon oil spill disaster [2].

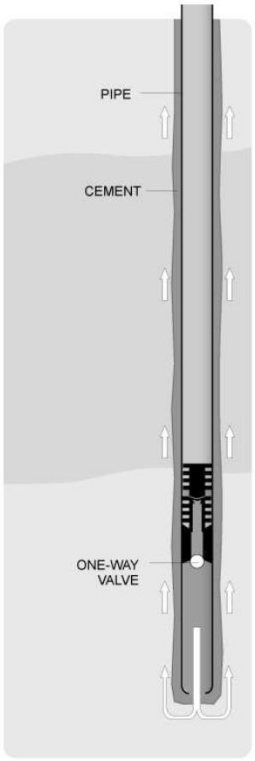

Figure 3. Cementing process: cement is pumped down through a one-way valve and fills the space between pipe and borehole [3].

The failure of zonal isolation may be attributed to several reasons, including lost circulation, fluid loss, and high temperature/pressure. In oil well cementing, loss of circulation occurs when drilling fluid or cement slurry flows into weak geological formations instead of returning up the annulus. The formation where

circulating fluid can be lost is called the thief zone. It has been shown that thixotropic cement slurries are effective for solving this issue [4]. After loss of circulation is detected, these slurries are prepared and pumped downhole to seal the formation. During pumping, its structure continuously breaks down, allowing it to flow. However, once it enters the thief zone, the velocity of the leading-edge decreases and the structure begins to recover. The resistance of the slurry to flow increases as its structure builds up, effectively plugging the thief zone. As a major factor for successful plugging is the rate of structural build-up, it is necessary to measure the relevant properties through suitable rheological methods and develop kinetics models to predict the build-up behavior immediately after the cessation of flow, especially during the first few minutes.

Fluid loss is another factor which could lead to cement failure. When oil well cement slurry is placed under pressure across a permeable rock formation, the water may be extracted by the rock formation [5]. This phenomenon may lead to the excessive difficulty in cementing work due to the increases in slurry viscosity. Water movement in a fresh suspension can result from suction pressure from the substrate, usually described as "water retention." Water retention behavior has been recognized as a critical factor for successful oil well cementing. It necessitates the evaluation of water retention of the thixotropic cement slurry and understanding the mechanism behind it.

The extreme oil well condition can also jeopardize the oil well cementing operation. For deep-water applications, downhole temperatures and depths can reach (and exceed) 180 ºC and 6000 m, respectively. There is also hydrostatic pressure and pumping pressure being exerted onto the material, which can reach up to 150 MPa. The premature loss of fluidity may make the bore unusable, and excessive delays in setting add to the cost of the operations. It is necessary to understand the phase evolution of the cement slurry during and after placement under down-hole conditions, as this has implications on the eventual sealing

ability of the cement sheath. Therefore, it is necessary to perform characterization under elevated pressure and temperature conditions.

1.3. MOTIVATION: 3D CONCRETE PRINTING

Additive manufacturing, generally known as 3D printing, was successfully applied in a large variety of domains, including industrial tooling and medical, in the last two decades. Its application in the construction industry was firstly introduced by Khoshnevis [6,7] using cement-based materials as the printing material and has since been developed steadily in recent years [8–10].

Unlike most extrusion-based 3D printing processes, in which materials are immediately solidified upon deposition, cement-based filaments are still in its fresh state [10]. For instance, the study [11] estimated that an interlayer time gap would be 19 min for a 108-square-meter house at a printing speed of 60 mm/s, which means the printed cement-based materials are in the fresh state far before the typical initial setting time of 3 – 5 hours. This highlights the importance of rheology, namely the control of shape stability and structural build-up rate of printed cement-based materials immediately after deposition.

The elimination of formwork is recognized as the major breakthrough of cement-based 3D printing. The absence of formwork can expand aesthetic freedom and reduce materials, labor and time, as the construction of formwork represents 35 – 60% of the overall cost of concrete construction [12]. However, for layer-based additive manufacturing, the freeform components exhibit relatively large exposed surface areas, which are susceptible to rapid evaporation of water. This can adversely affect material stability (i.e., the ability to stay homogeneous), hinder hydration and induce plastic shrinkage, ultimately impairing the

ultimate strength and durability of the printed structure. The surface moisture and bleeding rate of the fresh concrete are critical factors for the inter-layer strength of 3D printed elements [13]. Sanjayan et al. [13] demonstrated that moderate bleed water could be desirable in 3D concrete printing through improving surface moisture, which is the competition between bleeding and evaporation, thus increasing the inter-layer bond strength. Evaporation drying could be a major challenge for 3D concrete printing, which has no formwork to protect the material. Thus, this emerging technique requires a better understanding of water transport behavior.

1.4. MOTIVATION: VISCOSITY MODIFYING ADMIXTURES (VMAs)

To address the issues mentioned above in oil well cementing and 3D concrete printing, the usual practice of incorporating admixtures can be applied, which can manipulate the rheology and microstructure of the material. One class of admixtures that can be used are viscosity modifying admixtures (VMAs) [14], also known in the literature as viscosity enhancing admixtures (VEAs) [15] and stabilizing agents (STAs) [16]. In this dissertation, they are referred to as VMAs. They can be classified as inorganic VMAs, such as clays and colloidal silica, and organic VMAs, such as starch, cellulose ether, and gums.

1.4.1. NANOCLAYS

Attapulgite/palygorskite, a so-called “special clay,” is a magnesium alumino silicate clay with the theoretical formula of $Si_8Mg_8O_{20}(OH)_2(H_2O)_4 \cdot 4H_2O$ [17]. The preferred name according to the International Nomenclature Committee is palygorskite, although the name attapulgite is better known commercially [18]. It can be referred to as a nanoclay due to its dimension, 1.75 μm in length and 30 nm in

diameter [19]. A highly purified form of the attapulgite/palygorskite/nanoclay was the clay chosen for the study.

As clays have high water sorption capacity, they have been used as absorbents for grease, oil, water, and chemicals since the 1930s [20]. One widespread use, for instance, is as an absorbent for cat litter. The attapulgite clays can absorb cat waste effectively and prevent odors and bacterial degradation for several days [18]. The characteristic structure of nanoclay provides a significant amount of pore space and permits the absorption of water and other organic materials both on the exterior surface and also in the open channels of the nanoclay crystals [21].

As attapulgite can improve the colloidal and thixotropic properties of suspensions, another larger use is as a VMA in paints, suspension fertilizers, oil well drilling and cosmetics. These clays have also been used in the construction industry for applications such as slip-form paving, reducing formwork pressure of self-consolidating concrete, and more recently 3D concrete printing [7,11,22,23]. Attapulgite clays can significantly increase the yield stress and shape stability of fresh cementitious materials [24–26]. The studies [27,28] have shown that clays can increase the flocculation strength and floc size, which can explain the increase in yield stress over time [25,26]. Other researchers [24,29] have found clays to have detrimental effects on structural evolution, as captured through SAOS tests. Thus, the mechanisms underlying the clay's effect on structural build-up is still not fully understood.

Although primarily used as a VMA, it is necessary to investigate the effect of the clays on other performance properties at the addition levels of interest. In this dissertation, the phase evolution under elevated temperature and pressure, resistivity, compressive strength, tensile strength will also be investigated in addition to the rheological and water absorption properties.

1.4.2. DIUTAN GUM

Bio admixture has the long history of being used in building materials. For example, in his famous encyclopedia “De architectura libri decem,” Vitruvius (84–10 B.C.) described the use of biopolymers such as proteins for set retardation of gypsum and dried blood for air-entrainment [30].

Polysaccharide is a class of widely used bio admixture in building materials. They have almost universal occurrence in a living organism. For example, starch is the storage polysaccharide produced by most green plants, and the structural component of plants are formed primarily from cellulose. Polysaccharides are polymeric carbohydrate molecules composed of long chains of monosaccharides (also called simple sugars, the most basic units of carbohydrates). The types of linkages and monosaccharide units, as well as the existence of side groups, are the main affecting parameters on the solubility, viscosity and gelation properties.

The recent development of cementitious materials requires modifying the rheological properties of the cement mix. For instance, 3D printed concrete calls for low viscosity during pumping and high yield stress after deposition. To achieve this goal, polysaccharides show promise due to their interesting physicochemical features regarding thickening, stabilizing, binding and gelation. Some researchers identified four different working mechanisms of polysaccharides in cement pastes (Figure 4) [31]:

a) Water binding: polysaccharides are high hydrophilic. Their effective volume would increase in suspension due to the polysaccharide’s ability to fix part of the mixing water. It will increase the viscosity of the solution and further increase the macroscopic viscosity of the cement paste.

b) Polymer association and entanglement: at high concentrations, the chains of polysaccharides can entangle and increase the apparent viscosity of the suspension.

c) Depletion: non-adsorbed polymers are depleted from a "volume exclusion shell" around larger particles. The concentration difference leads to an increase in the osmotic pressure in the system, which brings the particles together. This could be at the origin of yield stress generated by the polymer in the system.

d) Bridging flocculation: the anionic and long-chain polysaccharides could adsorb on the cement particle surfaces and connect two or more cement particles together. This would increase the yield stress of cement pastes.

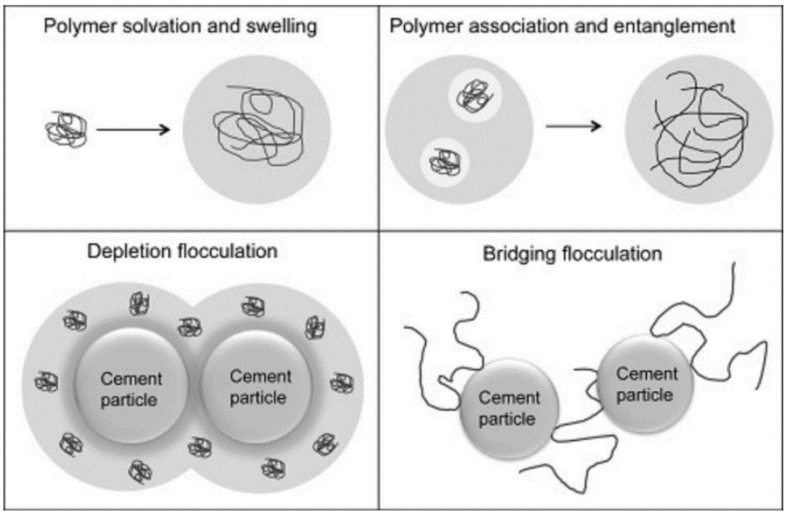

Figure 4. Working mechanisms of polysarccharides according to M. Palacios and R.J. Flatt [31].

Diutan gum is a high molecular weight, soluble, microbial and anionic polysaccharide produced by Sphingomonas bacteria in an aerobic, submerged fermentation [30]. Diutan gum consists of a repeat unit with β-1,3-d-glucopyranosyl, β-1,4-d-glucuronopyranosyl, β-1,4-d-glucopyranosyl, and α-1,4-l-rhamnopyranosyl, and a two-saccharide L-rhamnopyranosyl side-chain attached to the (1 → 4) linked

glucopyranosyl residue, as shown in Figure 5. Xu et al. [32] suggest a double helical molecular conformation of diutan gum. Carboxyl groups located on the backbone of the helix can stabilize the double helix, as well as promote associations between backbones. The interactions between the side chains located in the core of the helix modify the geometry of a double helix.

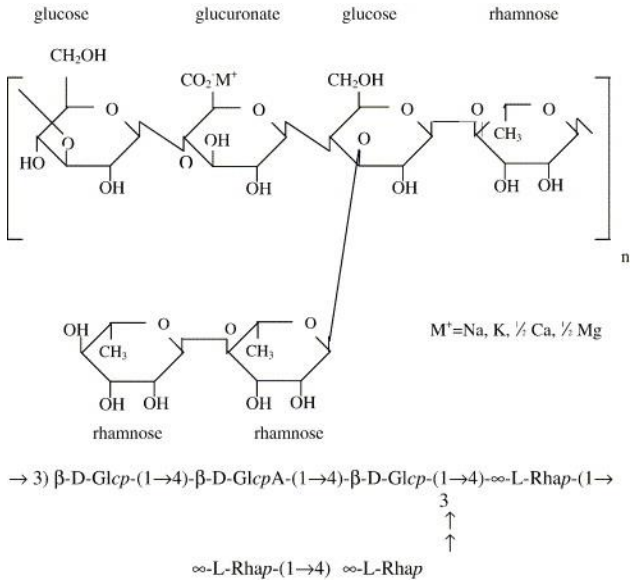

Figure 5. The molecular structure of diutan gum [33].

The adsorption is typically studied by adding the polymer to the cement paste, and after a period, filtering/centrifuging the system. The adsorbed amount is calculated by the difference between the concentration of polymer in the filtrate and its concentration before contact with cement. [33] finds that diutan gum has greater adsorption compared with hydroxypropyl methyl cellulose, which may be attributed to the anionic character of diutan gum, i.e., by the presence of the carboxylic acid functions on their molecular backbone, which is fully ionized at high pH. However, [34] revealed that welan gum, which behaves similarly with diutan gum because of the structural similarity, does not adsorb on the cement at all.

As a second-generation VMAs in the concrete construction industry, diutan gum's working mechanism and its interaction with cement particles still remain elusive.

1.5. ORGANIZATION

Chapter One provided the background and motivation of the work. Chapter Two gives a literature review of the study related to the present work. This includes the discussions of solid and liquid states of cement paste, the rheological parameters and existing experimental methods to characterize these two states, and synchrotron x-ray diffraction. Chapter Three studies the relationship between rheological properties and water transport properties in cement paste. Chapter Four proposes a non-linear build-up model to quantify the evolution of static yield stress and storage modulus. Chapter Five presents the phase evolution by using synchrotron XRD. Chapter Six determines the hardened properties of blended cement systems. And Chapter seven presents a summary of the key conclusions and possible topics of future work.

CHAPTER TWO

2. LITERATURE REVIEW

2.1. WATER TRANSPORT PROPERTIES

2.1.1. BLEEDING

Bleeding is the phenomena that water accumulates on the surface of the cement paste. The accumulated bleed water, expressed as a percentage of the net mixing water, is described in ASTM C232/C232M [1]. In the cement paste, there exist three forces that act simultaneously in a fresh cement paste, if we neglect cement hydration:

a) Brownian motion is the random motion of fine particle suspended in a fluid resulting from their collision with the fast-moving molecules in the fluid.
b) Colloidal attractive force: Van der Waals interactions were shown to dominate all other colloidal interactions in the case of cement pastes [2].
c) Gravity force.

Thus, [3] suggested the criterion of the appearance of the bleeding in cement pastes:

a) Brownian motion dominates attractive colloidal forces: In most types of cement, Brownian effects only play a minor role compared with the attractive colloidal interactions between cement grains. However, if Brownian motion dominates attractive colloidal forces at high admixture concentration, the cement paste would be very unstable, and the high degree of bleeding would occur.

b) Gravity dominates attractive colloidal forces: the gravity force which overcomes the resistance of colloidal force would drive the cement particle to settle. The cement system displays bleeding.
c) Colloidal attractive forces dominate gravity. The gravity force is not high enough to break the colloidal interactions network. The cement paste is stable, and there will be no bleeding.

If bleeding occurs, it can be considered as a self-weight consolidation process, i.e., the upward displacement of water through a compressible dense network of interacting cement grains instead of the settlement of individual cement grains in a dilute system. The consolidation process is controlled by the viscosity of the interstitial solution and the permeability of the porous medium, in this case formed by cement particles, as illustrated by Darcy's law for a consolidation process, i.e., fluid flow through porous media [4].

Tan et al. [5] derived a small-strain analytical solution based on self-weight consolidation process theory without considering the effect of hydration. Later, they proposed a finite-strain model which can account for the effect of hydration on bleeding [6]. Morris et al. [7] presented the linear finite- and small-strain analytical solutions of bleeding and found that the fitting by these two methods was virtually indistinguishable in the case of cement paste. By using the small-strain model, Ghourchian et al. [4] showed the bleeding test can be used as a simple method for measuring the permeability.

Bleeding water accumulates either through progressive consolidation of the solid skeleton, termed "normal bleeding," or through the formation of channels, which is usually characterized by a sudden increase in bleeding rate leading to a convex-shaped bleeding-time curve, termed "channeled bleeding" [5]. The effect of channels on the compressive strength is found to be negligible as the area of such channels is small compared to the total area as shown in Figure 6[8].

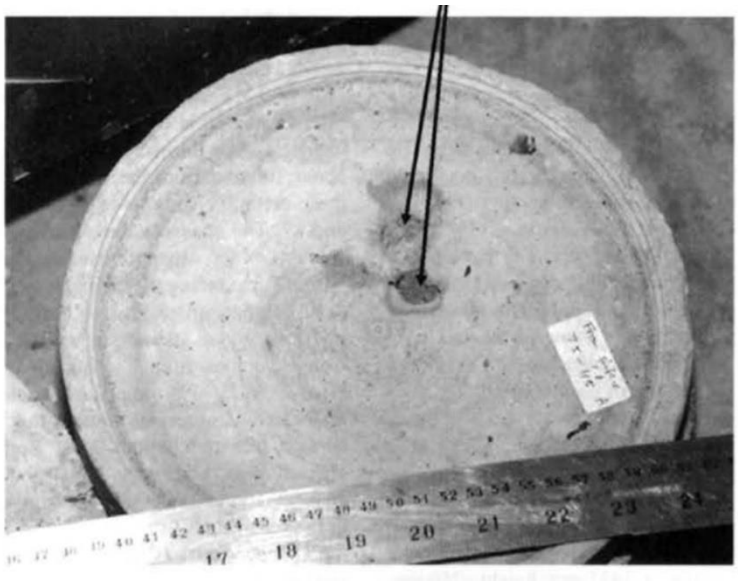

Figure 6. Bleeding channels (pointed with arrows) occurs in the concrete pile [8].

2.1.2. WATER RETENTION

Water movement in a fresh suspension can result from suction pressure from the substrate, usually described as “water retention.” For instance, when oil well cement slurry is placed under pressure across a permeable rock formation, the water may be extracted by the rock formation [9]. Water retention is also an important parameter to dry mix mortar which are mainly used for laying stones and bricks as adhesives [10]. When mortar is applied on a substrate, such as bricks and plaster, water may be absorbed by the substrate. The inadequate water retention capacity links to the deteriorated mortar- substrate bonding.

Two standard methods are used to measure the water retention capacity as follows:

2.1.2.1. STANDARD DIN 18555-7

In Standard DIN 18555-7 [11], the freshly-mixed mortar is in contact with filter paper. The suction behavior of an absorptive substrate is simulated by the filter paper. A good linear correlation is found with the use of filter paper and plaster as a dry porous substrate [12]. Thus, this method is reliable in simulating the actual water migration process that occurs through the interface between a fresh cement paste and a dry porous substrate. The absorbed water in filter papers is recorded.

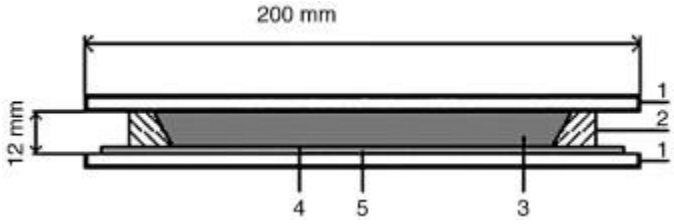

Figure 7. The arrangement of DIN 18555-7 (1: two plastic plates, 2: conical plastic ring, 3: mortar, 4: filter paper, 5: nonwoven tissue) [11].

2.1.2.2. ASTM C1506 STANDARD

In ASTM C1506 standard [13], the suction force is provided by a vacuum instead of a filter paper. The dish is filled with mortar, which is connected to a vacuum by a funnel. The sample is exposed to a vacuum of 50 mm of mercury for 15min. Loss of mixing water mass is recorded.

By comparison of these two methods, Patural et al. [14] showed that they are comparable as both methods gave rather close results. The degree of water retention can be calculated by the following equation for both standards:

$$WR \quad (\%) = \frac{W_0 - W_1}{W_0} \times 100$$

where W_0 represents the initial mass of mixing water, W_1 is the loss of mixing water mass.

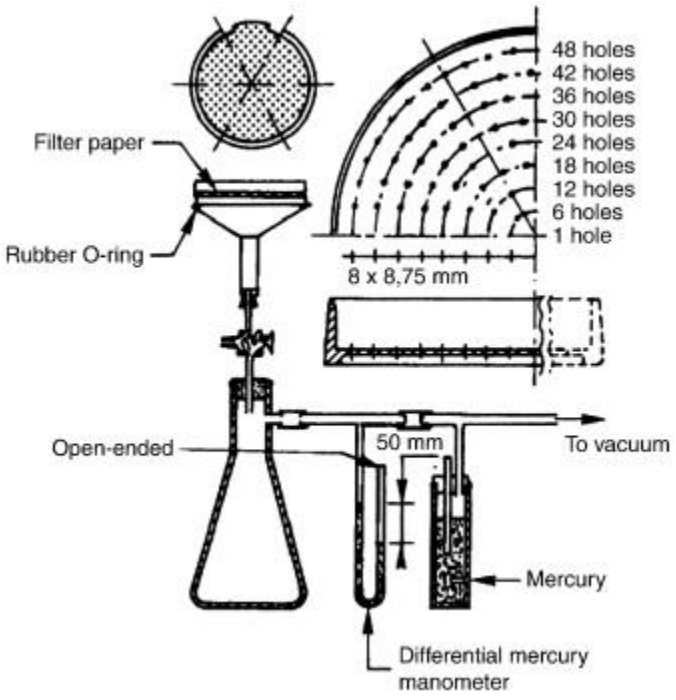

Figure 8. The arrangement of ASTM C1506 standard apparatus [13].

2.1.3. EVAPORATION

The water evaporation on the explored surface of concrete is accelerated under conditions such as high temperature, low relative humidity, high wind velocity and solar radiation. Lura et al. [15] explained the mechanisms governing the drying behavior of cementitious materials utilizing the drying model of gels presented by [16]:

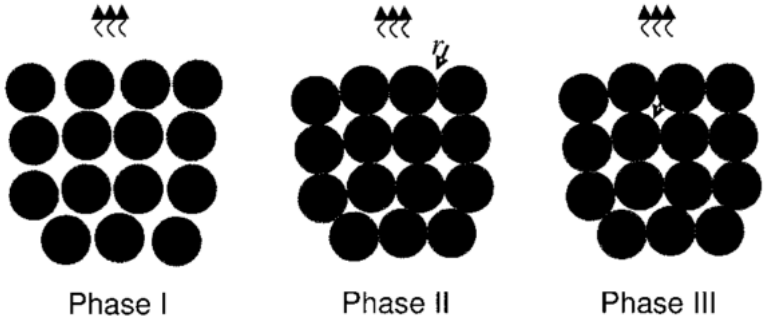

Figure 9. The phases of drying of cementitious materials [15].

First, there is evaporation of accumulated bleed water, where the rate of evaporation is the same as that of bulk water. ACI 305R-96, "Hot Weather Concreting" [17] gives a nomograph to predict the evaporation rate of bleeding water as a function of temperature, humidity and wind velocity. Paul J. Uno [18] clarified the background of ACI 305R-96 nomograph and offered an alternative nomograph and various formulas to predict an evaporation rate of surface water.

The second phase is a constant rate period where air-liquid menisci and capillary pressure develop in the top layers and compress the solid skeleton, resulting in the pore fluid surfacing and evaporating.

In the final phase, the capillary pressure can no longer compress the solid skeleton and water is drawn from the inside of the specimen. The evaporation rate decreases significantly. A critical point is defined as the boundary between second phase and final phase which marks the time point when the menisci fall below the surface of the specimen. The menisci provide the high internal stress caused by capillary tension. The plastic shrinkage cracking is most likely to occur at this critical point. Ghourchian [19] found that hydration

is the dominant factor in controlling the plastic shrinkage cracking. The reactive cement material with high bulk modulus increasing rate is less prone to plastic shrinkage cracking.

2.2. STATIC YIELD STRESS OF FRESH CEMENT PASTE

Rheology is the science of the deformation and flow of materials, both solids and liquids. Fresh state cement paste acts like a solid when the applied stress is smaller than a certain value (called yield stress) and behaves as a liquid when the stress is larger than the yield stress. In particular, the static yield stress marks the transition from the solid to the liquid regime. To understand the solid regime of cement paste and determine the static yield stress is critical for rheological characterization and application. For example, if the yield stress of an oil well cement slurry has not developed sufficiently to resist gas pressure from the surrounding well formation, the gas could penetrate the cement slurry and compromise oil well completion.

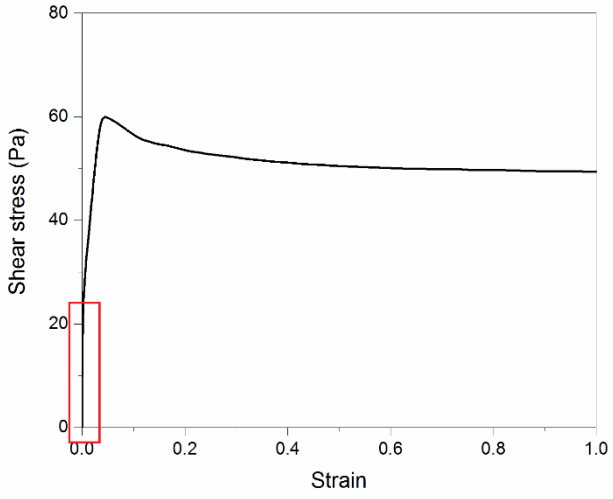

Figure 10. Shear stress as a function of shear strain of a cement paste sample

As shown in Figure 10, the shear stress progressively develops to a static yield stress value and then decays to an equilibrium value, which is representative of steady-state flow. The static yield stress marks a transition between solid-like and liquid-like behavior. Another far less visible feature is the high elastic modulus on the first few tenths of % strain, as shown in the red box in Figure 10. As shown in a previous study [35], there exist two "structures" with different scales in cement pastes that can be attributed to the origin of yield stress. They will be described briefly here:

1. The static yield stress of cement paste is governed by particle force and particle arrangement from a first principle analysis of static yield stress as proposed by R.J. Flatt and P. Bowen [36]. The particle forces include repulsive electrostatic forces, van der Waals forces, and Brownian force. Repulsive electrostatic forces alone are generally insufficient alone to prevent agglomeration due to van der Waals forces [37]. Brownian effects only play a minor role in the case of cement pastes [38]. Thus, Van der Waals interactions were shown to dominate all other colloidal interactions. Moreover, distinguishing the particle forces and discussion of particle arrangement is out of the scope of this study. We can describe yield stress increase as a general flocculation process, which is in accordance with other publications [39,40]. The static yield stress increases at rest due to flocculation, and apparent viscosity decreases under shear flow due to de-flocculation [40].
2. As shown in the red box in Figure 10, the high elastic modulus on the first few tenths of % strain indicates a rigid interaction which is different with the colloidal interaction. The feature can be associated with calcium silicate hydrate (C-S-H) "bridges" at the pseudo contact zones between cement particles [35,41].

Various methods have been developed to measure the static yield stress from rheological methods to conventional field tests.

2.2.1. VICAT NEEDLE TEST

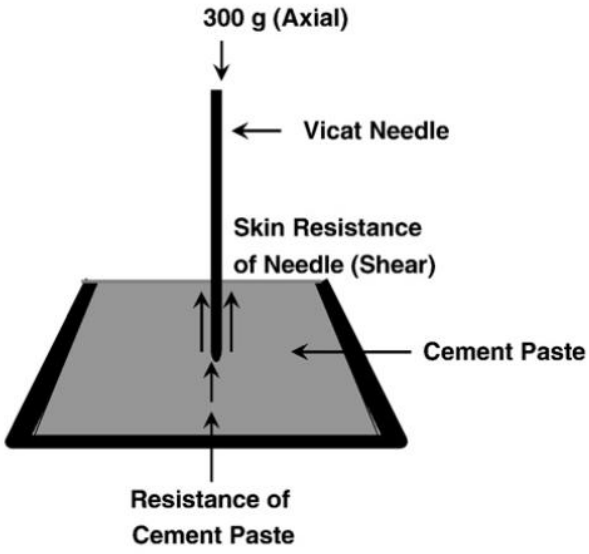

Figure 11. A schematic illustration of the Vicat Test [42].

The Vicat needle test consists in letting a loaded needle (300 g, 1 mm in diameter) penetrate a hydrating sample and measuring the depth of penetration. Repeated tests can be performed at different positions until the sample is too hard for the needle to penetrate it.

The test is usually used to determine the setting time of cement materials. The start and end of the setting are defined by standard penetration depths, which are 25 mm for the Vicat initial time of setting and 0 mm for the final time of setting. If the shearing is static, some researchers linked the depth information with "yield capacity" by using the equation [42]:

$$\tau_0 = \frac{F}{2\pi rh + 2\pi r^2} \quad (1)$$

where: F is the axial force exerted by the needle, and r and h (mm) are the radius and depth of penetration of the needle, respectively.

If the flow is static, the calculated yield stress does not depend on the needle mass. However, Sleiman et al. [43] found the different mass of needles provide different "static yield stress" results. By comparison with static yield stress results by using vane geometry, the discrepancy further highlights assumptions are not suitable for fresh state cement paste. In the Vicat test, the speed of needle penetrates the cement paste could be very high – the shear rate can be as high as 600 1/s. In this case, the flow cannot be considered as static. Another concern is the end effect where flow under the needle is very complicated. The assumption that shear radius is the same as needle radius may not be true.

2.2.2. MODIFIED VICAT TEST

To overcome the drawback of the Vicat test, the static Vicat test was proposed [43]. A needle is rigidly attached below a fixed support and is immersed into the cement paste. The apparent mass of the needle is recorded. The apparent mass M(t) can be deduced from the static equilibrium of the needle in the cement paste:

$$M(t) = (F_{gravity} - F_{buoyancy} - F_{shear})/g \quad (2)$$

The static yield stress at the surface of the needle can be deduced from this apparent mass evolution using the following relation:

$$\tau_0(t) = \frac{g}{2}\left(\frac{\Delta M(t)}{2\pi r h} - r\rho\right) \quad (3)$$

Where r and h (mm) are the radius and depth of penetration of the needle, respectively. g is gravitational acceleration. ρ is the material density. ΔM is the mass variation induced by needle immersion.

This measurement method can successively evaluate the static yield stress evolution during the dormant period [43]. The static yield stress agrees with the results obtained by conventional rheometry method. The modified Vicat test was, therefore, an interesting alternative to conventional rheometry as it remains cheap and straightforward.

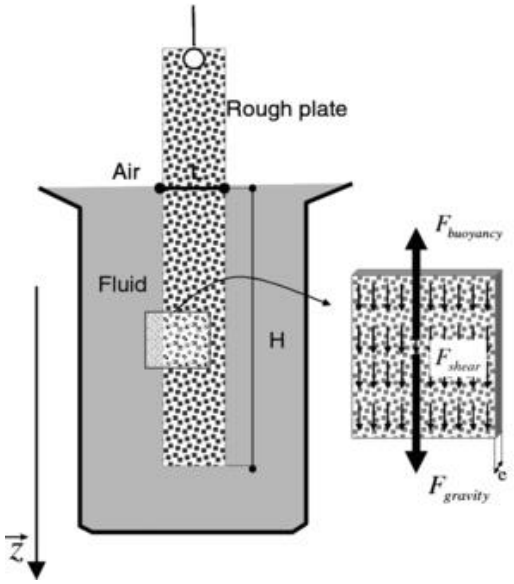

Figure 12. Static equilibrium of the immersed object in a fluid [44]. The other immersed objects can be a needle, steel rebar and plate [45].

2.2.3. DIRECT SHEAR TEST

The direct shear test is widely used in geotechnical applications to determine the soil mechanics parameters, i.e., cohesion (C) and angle of internal friction (ϕ) in accordance with ASTM D3080 [46]. Assaad et al. [47] assess the feasibility of this test to evaluate static yield stress of cement paste and found that the value of cohesion resembles the value of static yield stress determined using the rheological method ranging from kPa to just a few Pa. The cohesion (C) is a parameter similar in nature to the static yield stress ($\tau 0$).

A direct shear test apparatus shearing box is comprised of two separate halves filled with compacted cement paste. In this test, two halves are made to slide along each other at a certain constant velocity. The cement paste distorts along with a linearly increasing shearing force up to a maximum value, then a non-linear decay towards a steady state region. The shearing plane occurs in the middle of the material itself along a pre-defined interface represented by the horizontal surface area of the shearing box. The cohesion (or the static yield stress) is calculated by dividing the shear force by the specimen's cross-section area.

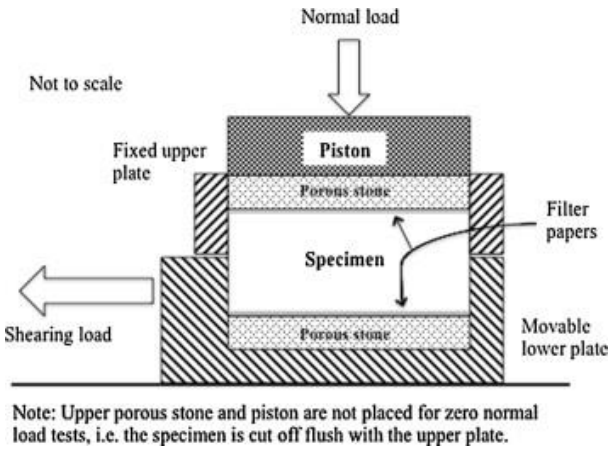

Figure 13. A schematic illustration of the direct shear test [47].

In literature, the direct shear test has often been employed to test highly cohesive pastes due to ease of sample preparation and absence of the artifacts, such as shear localization and wall slip, compared to conventional shear-driven rheometers [48]. Thus, this technique can be readily adopted to evaluate the yield stress of 3D printed concrete [49]. Lu et al. [50] used the direct shear test to verify a constitutive model developed for predicting yield stress of cementitious materials.

2.2.4. UNIAXIAL UNCONFINED COMPRESSION TEST

Uniaxial unconfined compression test (ASTM D2166 [51]) is another widely used geotechnical method, which can be adopted to determine the static yield stress of cementitious materials. In the test, the cement sample is filled into a steel cylindrical mold. After consolidating, the sample is carefully demolded. During the test, a constant axial load is applied until sample failure, and the maximum compressive stress (τc) is recorded. τc obtained from uniaxial unconfined compression test is also called green strength [28]. Researchers utilized uniaxial unconfined compression test to evaluate the shape stability of cement-based extruded materials [52]. If the height-diameter ratio is high enough to guarantee a diagonal shear failure plane to form, the static yield stress ($\tau 0$) is calculated as one-half of the measured maximum compressive stress [53].

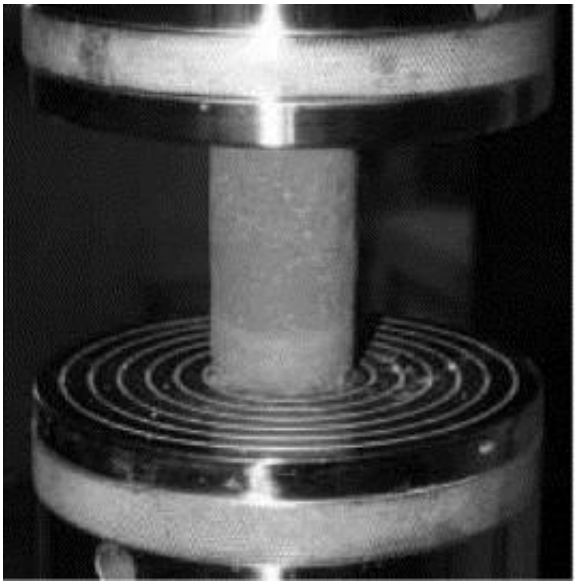

Figure 14. Uniaxial unconfined compression test of fresh state cement mortar [52].

Such measurements are only feasible with highly cohesive materials that can resist the deformation under its self-weight and self-stand in a vertical position. Thus, the uniaxial unconfined compression test can be used to evaluate the static yield stress of 3D printed concrete [49], including strength development (or structural build-up/thixotropy) over time [49,53]. The rate of strength development measured by this method has been found to be equal to the results of the direct shear test [49]. Assaad et al. [53] evaluated the effect of cement content, the w/c, and the addition of VMA or silica fume on the yielding behavior of cementitious paste through uniaxial unconfined compression tests.

2.2.5. RHEOLOGICAL TEST: CREEP TESTS

Creep test is usually considered the most accurate method to determine the static yield stress as it is independent of applied shear rate/stress rate. In creep test, a shear stress is applied instantaneously to the material, then maintained constant for a period.

For thixotropic materials like cement paste, if the applied stress is below the critical value, the fluid does not flow, and viscosity can be considered as infinity. If the applied stress is above a critical value, even relatively slightly, the viscosity decreases to a low steady-state value. This phenomenon is called "viscosity bifurcation," or "avalanche behavior" [54].

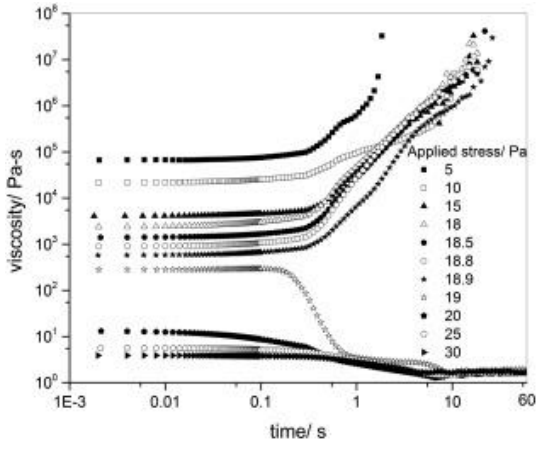

Figure 15. Viscosity bifurcation of cement pastes under creep at various shear stress [25].

For a small increase in stress from below to beyond the static yield stress (τ_0), the shear rate increase from zero to a finite value apparently larger than a "critical shear rate" ($\dot{\Upsilon}_{cr}$). Creep test can also identify a critical strain (γcr) defined as maximum deformation reachable in the solid regime.

2.2.6. RHEOLOGICAL TEST: STRESS GROWTH TEST

We perform stress growth measurements by applying deformation at a sufficient low constant shear rate. The shear stress progressively develops to a maximum value and then decays to an equilibrium value, as shown in Figure 10. The static yield stress is defined as the peak shear stress value [55]. It gives the profile of the solid regime. The peak stress value is considered as static yield stress and the strain corresponding to yield stress can be considered as "critical strain" (γ_{cr}). The peak defined by the maximum measured stress value depends on the shear rate applied [56]. However, as it is easier to practice than the creep test, it is often employed as a reference test to give an approximation of the yield stress that enables the comparison with other testing methods.

In order to capture the time dependence of the static yield stress, this test has to be repeated many times for various resting time, with each experiment providing only a single point of the static yield stress vs. time relationship. As this method is destructive, we should prepare a new sample for each yield stress measurement. As a more rapid and nonperturbative method would be preferred, the elastic modulus method measurement method, which is also called small amplitude oscillatory shear (SAOS) test, is implemented.

2.2.7. SMALL AMPLITUDE OSCILLATORY SHEAR (SAOS)

In the solid regime, cement paste behaves like a viscoelastic material. In order to evaluate the viscous and elastic behaviors separately, an oscillatory strain ($\gamma = \gamma_0 \sin(\omega t) = \gamma_0 \sin(2\pi f t)$) is applied and the stress response is recorded. If the strain is sufficiently low so that the particles in the suspension remain close to each other, the microstructure is not disturbed, and the material can recover elastically. In this case, when cement is probed in its linear regime, the stress response is of the form:

$$\tau = \gamma_0[G' \sin(\omega t) + G''\cos(\omega t)] \quad (4)$$

where G' is the storage modulus, G'' is the loss modulus. γ_0 is maximum strain amplitude, t is time, ω is angular frequency in rad/s, and f is the frequency in Hz.

As an initial step, a strain sweep is conducted to determine the linear viscoelastic domain (LVED), where within the LVED the storage modulus G' is independent of the applied shear strain amplitude. Frequency must also be considered to find the LVED. If the frequency is too high, the structure cannot recover, and the measured LVED will be inaccurate. Therefore a frequency sweep is performed, as well.

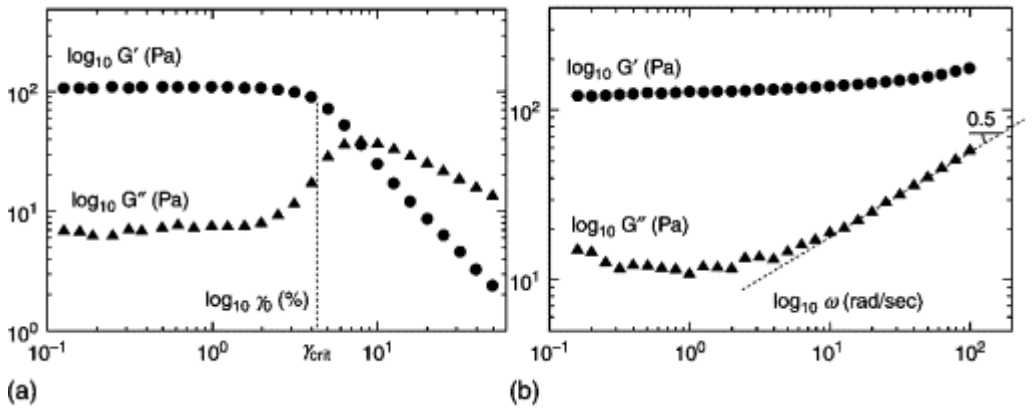

Figure 16. (a) G′ and G″ vs. strain measured in a dense colloidal suspension during a strain sweep; (b) G′ and G″ vs. frequency in the linear regime, measured in the same suspension during a frequency sweep oscillatory experiment [57].

If the tested material remains in the LVED, the oscillatory test can be considered as a non-destructive method. Note that in many thixotropic systems such as bentonite suspensions and mustard, measurement of storage modulus through SAOS shows quantitatively similar evolution as that of static yield stress

[58]. Thus, as a less time consuming, non-perturbing test, it can be considered as a desirable approach to characterize stress-bearing ability over time for these thixotropic systems. However, its validity in the cement paste system needs to be further verified, especially with the addition of VMAs in the system.

2.3. DYNAMIC YIELD STRESS OF FRESH CEMENT PASTE

Static yield stress, which marks the transition from the solid to the liquid regime, is the minimum stress that should be overcome to initiate flow from rest. Dynamic yield stress, which corresponds to the transition from the liquid to the solid regime, marks the maximum stress needed to terminate flow. Typically, the static yield stress will be larger than the dynamic yield stress, since the flow induces the disturbance of the sample and the structure breaks down [59]. Qian et al. [60] attributed the discrepancy between dynamic and static yield stress to thixotropy by measuring dynamic yield stress and static yield stress of mortars through constant applied angular velocity and creep recovery, respectively.

Fourmentin et al. [59,61] gave a simple way to distinguish the static and dynamic yield stress by using the flow curve. During the increasing ramp, as shown in the upward arrow in Figure 17, the stress reaches a stress plateau that corresponds to the transition between the solid and the liquid regime: it may be considered as the "static" yield stress of the material. Since the cement paste is thixotropic, the apparent viscosity decreases with the flow duration during the decreasing ramp. It leads to the lower stress compared with the increasing curve. Finally, the decreasing curve ends by a stress plateau, which may be considered as the "dynamic" yield stress.

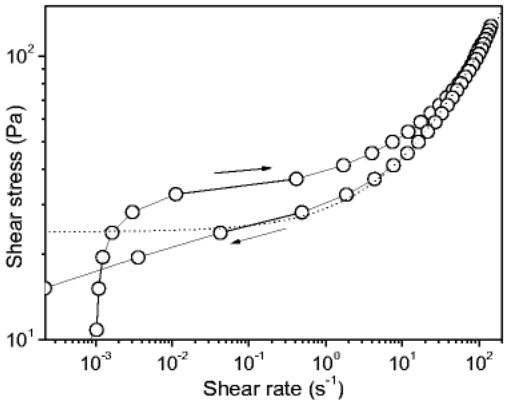

Figure 17. Apparent flow curve obtained from a shear rate sweep for a cement paste [61].

Various methods have been developed to measure the dynamic yield stress from rheological methods to conventional field tests.

2.3.1. SLUMP TEST

The slump test (ASTM C-143) is the most commonly used method to evaluate the workability of cementitious materials. In the slump test, the conical shaped mold is filled with a fresh mix. Then, the mold is lifted and the material flows. The decreased height of material after lifting the mold is defined as slump (Figure 18).

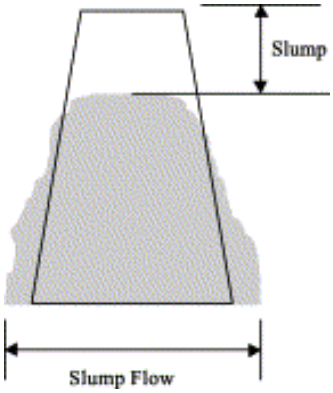

Figure 18. Slump test. The cone is filled with concrete and then lifted. The decreased height of material after lifting the mold is defined as slump [62].

Slump test is a "stoppage test," where if the shear stress in the sample is lower than the dynamic yield stress, the flow stops and the sample retains its shape. Thus, the final shape of the sample is directly related to the dynamic yield stress. Several published studies have shown the strong correlation between slump value and the dynamic yield stress by using different conical geometries from Abrams cone to mini-cone [62–64]. By using the analytical approach, Roussel et al. [63] found that it is possible to determine the yield stress (τ_0) using the slump test if there is a large or a small slump (note that this analysis does not take in account the thixotropic effect of cementitious materials) :

$$\text{If H<< R, } \tau_0 = \frac{225\rho g\Omega^2}{128\pi^2 R^5} \tag{5}$$

$$\text{If H>>R, } \tau_0 = \frac{(H_0 - S)\rho g}{\sqrt{3}} \tag{6}$$

Where R and H are the final radius and height of the sample. ρ is the material density. g is the gravitational acceleration. Ω is sample volume. H0 is the initial sample height. S is the slump value.

Tregger et al. [65] found that equation (5) underestimates the dynamic yield stress of highly flowable cement paste that is formulated from typical SCC mixtures. The discrepancies between theory and experiment may be due to the difference between the rheological protocol and actual shearing experienced by the material during the slump test.

2.3.2. INCLINED PLANE TEST

There are two ways to carry out the inclined plane test. The first one can be categorized as “initiation test” in which one progressively lifts the plane up to the critical slope for which a flow is observed. The shear stress at the critical slope is linked to static yield stress. Khayat et al. [66] used the inclined plane test to evaluate the static yield stress of self-consolidating concrete. However, the determination of this critical slope is delicate and would certainly lead to large experimental errors [67].

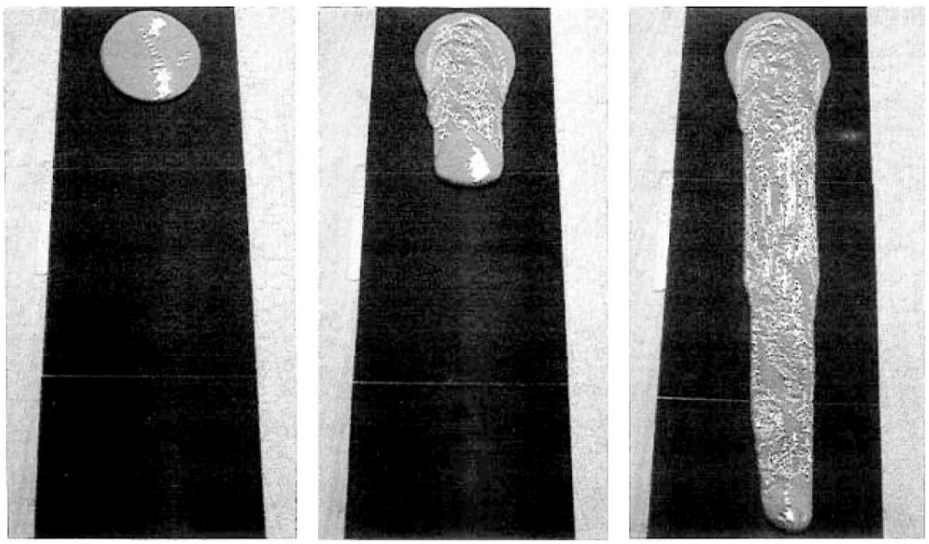

Figure 19. An inclined plane test on a clay suspension sample [54].

The second way can be categorized as “stoppage test.” The material flows on the inclined plane at a given slope. Then, the flow stops if the shear stress in the sample is lower than the dynamic yield stress. The dynamic yield stress can then be calculated by using the equation:

$$\tau_0=\rho\cdot g\cdot h\cdot \sin\alpha \quad (7)$$

where ρ is the sample density, g is the gravitational acceleration, h is the characteristic height of the spread sample and α is the angle of the plane.

2.3.3. RHEOLOGICAL TEST: FLOW CURVE TEST

Flow curve, the relationship between the shear stress and shear rate, is the most common measurement to determine the dynamic yield stress of fresh state cement materials. Several tests, such as a linear/stepwise increase and decrease of shear rate/shear stress, can be applied to obtain the flow curve. A typical flow curve is shown in Figure 20.

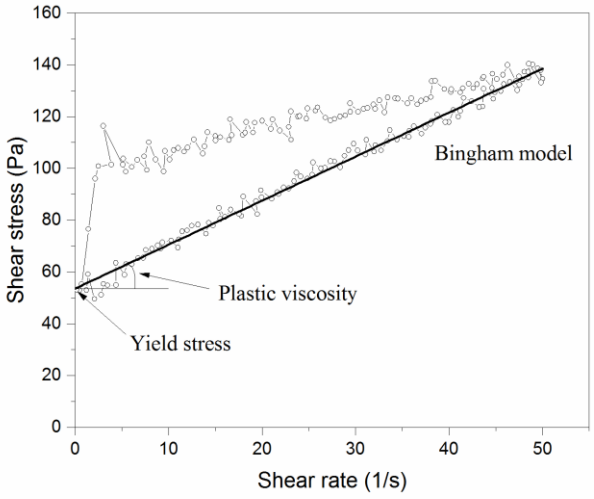

Figure 20. A typical flow curve with Bingham model.

Various rheological models can be chosen to describe the flow curve results. The Bingham, Herschel–Bulkley and modified Bingham models (Figure 21) are commonly used for cement-based materials. The dynamic yield stress is the intercept with the vertical axis (when the shear rate is zero).

$$\tau = \tau_0 + \eta_{pl}\dot{\gamma} \tag{8}$$

$$\tau = \tau_0 + K\dot{\gamma}^n \tag{9}$$

$$\tau = \tau_0 + \eta\dot{\gamma} + c\dot{\gamma}^2 \tag{10}$$

where τ is shear stress, $\dot{\gamma}$ is sthe hear rate, τ0 is dynamic yield stress, and ηpl is plastic viscosity. n is power function for the shear rate. c is consistency parameter.

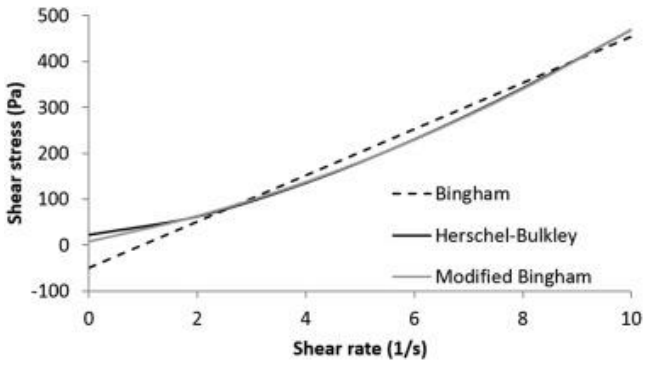

Figure 21. Bingham, Herschel–Bulkley and modified Bingham model applied to the same rheological result [68].

2.3.4. RHEOLOGICAL TEST: TACK TEST

In this test, the top plate was displaced at a constant velocity, and the normal pulling force was recorded[69][70]. Figure 22 shows a representative normal force evolution measured by the tack test. The maximum normal force (F_{max}) is the adhesive strength, which is due to viscous dissipation and static cohesion. Some publications [70,71] have established the relationship between maximum normal force with a dynamic yield stress and plastic viscosity in squeeze flow. If the pulling velocity is sufficiently low, the plastic viscosity item can be dismissed. Then the expression becomes:

$$\tau_0 = \frac{3h_m F_{max}}{2\pi R^3} \tag{11}$$

where F_{max} is the maximum normal force, R is the radius of mortar sample, h_m is the plate distance at the maximum normal force F_{max}, and V is the pulling velocity of the plate.

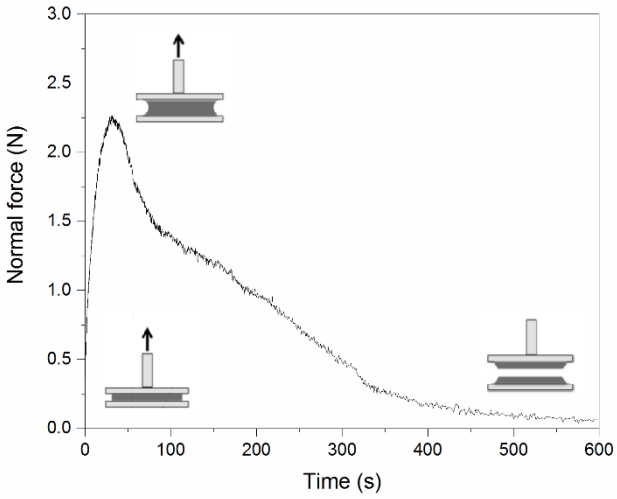

Figure 22. Typical normal force evolution obtained during the tack test.

2.4. VISCOSITY OF FRESH CEMENT PASTE

Concrete has been referred to as “liquid stone” [72]. Before setting and hardening, concrete acts like liquid, which can flow through pumping and tremie to fill a mold or formwork. Self-consolidating concrete was first developed in 1988 in Japan [73]. It is a highly flowable concrete that eliminates the need to apply any external vibration during casting.

Apparent viscosity is defined as the ratio between shear stress and shear rate. It is a measurement of the flowability that is related to the construction process, such as the time needed to empty a truck or fill a given formwork [74]. Another rheological parameter, which is used to describe flowability, is plastic viscosity. Plastic viscosity is the slope of the shear stress-shear rate relationship as described by the Bingham model. Plastic viscosity represents the viscosity of a cement paste when extrapolated to infinite shear rate based on the mathematics of the Bingham model. The relationship between apparent viscosity and plastic viscosity is as follows:

$$\eta = \eta_{pl} + \tau_0/\dot{\gamma} \tag{12}$$

2.4.1. SLUMP FLOW

The slump flow test is performed to measure the workability of highly flowable cement materials. Similar to the slump test, the cone is filled with concrete. Then, the cone is lifted. The diameter of the spreading concrete is measured in accordance to ASTM C 1611 [75]. As shown in section 2.3.1., the final diameter of the spread cementitious material is largely dependent on the yield stress instead of viscosity. Tregger et al. [65] found that the time it takes for the flow to reach the final diameter is related to the ratio between

the viscosity and yield stress. They further proposed an expression for determining the plastic viscosity based on the dynamic yield stress and time to final diameter:

$$\eta_{pl} = \tau_0 \, (6.41 \times T_f - 1.94) \times 10^3 \tag{13}$$

Where η_{pl} is plastic viscosity, τ_0 is dynamic yield stress, Tf is the time to final diameter.

2.4.2. RHEOLOGICAL TEST: CONSTANT SHEAR RATE

When we apply a constant shear rate on thixotropic materials, the viscosity would exhibit a decay and then eventually reach a constant value, which is called equilibrium apparent viscosity. From low shear rate to high shear rate, the microstructure is stronger than the steady state at a high shear rate, so the instantaneous stress is higher than the equilibrium value at the high shear rate. The shear stress will increase to a peak value and then decrease due to "structural breakdown" to an equilibrium state. From high shear rate to low shear rate, the microstructure is weaker than the steady state at a low shear rate, so the instantaneous stress is lower than the equilibrium value at the low shear rate. It takes time for "structural buildup" and for the shear stress to increase to a new equilibrium value.

Tattersall described cement "structural breakdown" by an exponential expression in 1954 [76]. Cheng and Evans [77] proposed an empirical thixotropy model to describe both "structural breakdown" and "structural buildup" behaviors. Based on the same assumptions as Cheng and Evans, Roussel [39] presented a model to quantify the thixotropic effect of cement paste, as shown in Figure 23.

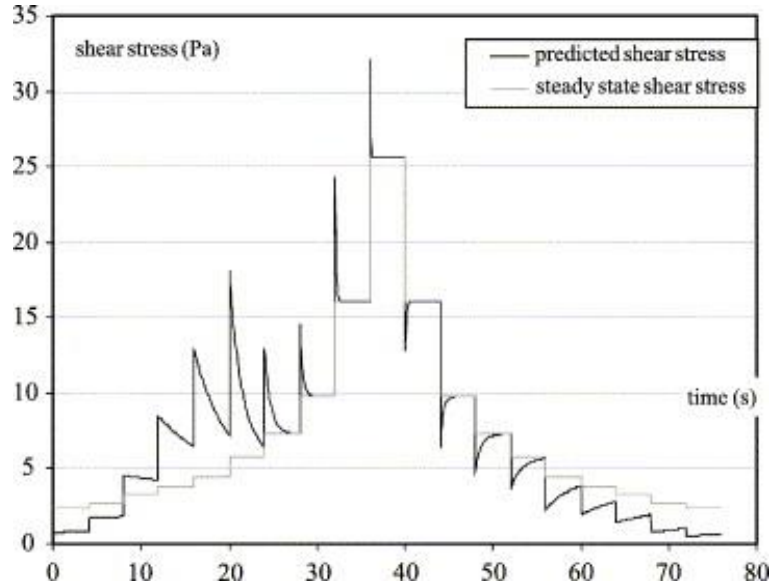

Figure 23. Evolution of the shear stress in term of time in the step-wise shear rate test [39].

2.5. SYNCHROTRON X-RAY DIFFRACTION

X-rays, which are electromagnetic waves, interact only with charged elementary particles - electrons and protons. Proton has the same charge as an electron, but its mass is 1836 times greater than electron mass. Therefore, X-rays interact mainly with electrons in atoms. When X-rays strike electrons, they make the electrons move. The movement of these charges re-radiates waves with the same frequency. These re-emitted wave fields interfere with each other either constructively or destructively, producing a diffraction pattern on a detector, determined by Bragg's law:

$$2d\sin\theta=n\lambda \tag{14}$$

where d is the spacing between diffracting planes, θ is the incident angle, n is any integer, and λ is the wavelength of the incident X-rays.

By measuring the angle (θ) where these bright spots (a diffraction pattern) occur on a detector as shown in Figure 24, the atomic spacing (d) can be determined by Bragg's law. The brightness of these spots is related to the amount of the crystalline phase. Diffraction data are usually presented as a diffractogram, in which the diffracted intensity or "brightness" is shown as a function either of the scattering angle 2θ or as a function of the atomic spacing (d).

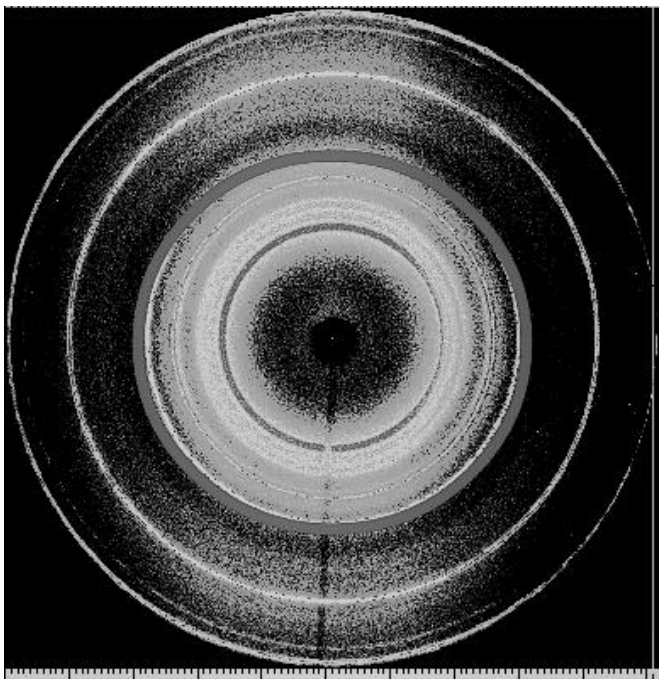

Figure 24. XRD pattern of fresh state cement sample

X-ray diffraction is a strong tool for identifying the crystalline phase in cementitious materials. However, to probe the crystalline phase change during first few hours of hydration, X-ray diffraction results captured by a conventional Bragg-Brentano diffractometer (Figure 25) require the additional sample preparation procedure and hydration arrest, which would lead to decomposition or alternation of hydrated aluminate phases. To avoid this issue, transmission geometry (Figure 25) in sealed sample tubes could be used to obtain X-ray diffraction diagrams from the pastes without drying and grinding of the samples. However, it is limited by the attenuation of the beam passing through the sample. This is a particularly severe problem

for the relatively long wavelength X-rays used in laboratory diffractometers. Even with only about 0.2 mm sample thickness, X-ray transmission efficiency was probably only ~10%, leading to long data acquisition times [78].

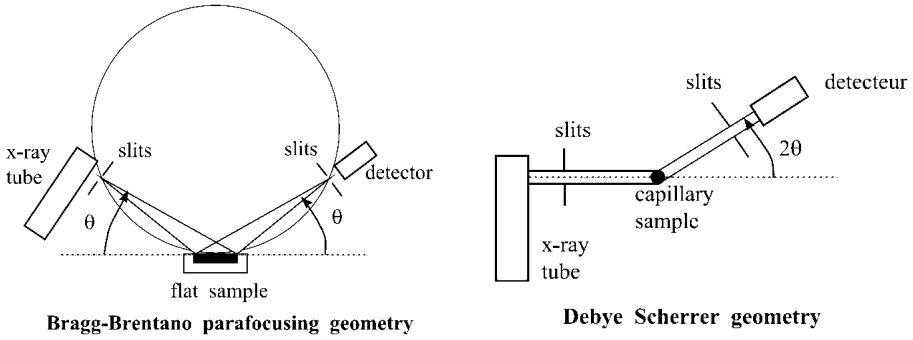

Figure 25. Bragg-Brentano geometry (left) and transmission geometry (right).

The direct observation of rapid crystalline phase changes in dense cement pastes on the time scale of seconds has only now become possible through the use of high-energy X-rays from synchrotron sources. In synchrotron radiation, electrons are accelerated to extremely high speeds, injected in the synchrotron ring to move in a large circle. As the electrons pass through magnets around the ring, they lose energy in the form of light, emitted as a narrow pencil directed forward. The high spatial resolution, high data collection speed, and high sample penetration allow the in-situ hydration studies of a "bulk" cement sample.

CHAPTER THREE

3. EVALUATION OF WATER TRANSPORT OF FRESH CEMENT PASTES

3.1. INTRODUCTION

Water transport property is the ability of water to move through the matrix of porous materials in response to a gradient of pressure. In concrete practice, water transport covers several different behaviors including bleeding, evaporation, and water loss from the fresh cement mixture into the substrate.

Bleeding describes the phenomena when water rises or bleeds to the surface once the fresh concrete is placed. Free water escapes from cement particle flocs and flows out due to a density difference between the water and cement grains. [79] summarized the criteria for the occurrence of bleeding. If colloidal attractive forces dominate gravity, there will be no bleeding. If gravity dominates colloidal attractive forces, bleeding occurs. The bleeding process is controlled by the viscosity of the interstitial solution and the permeability of the porous medium, in this case formed by cement particles, as illustrated by Darcy's law for a consolidation process, i.e. fluid flow through porous media [80].

In most cases, bleeding is considered to be undesirable. Excessive bleeding weakens the bond between the cement matrix and the subsurface of aggregates, which induces a nonuniformity in strength [81]. This has a major impact on the long-term durability of concrete. However, concrete mixtures with an inherent low rate of bleeding or low quantity of bleed water are susceptible to plastic shrinkage, which appears in concretes with large, exposed surface areas, such as decks, pavements, and floors. Sanjayan et al. [13] demonstrated that moderate bleed water could be desirable in 3D concrete printing through improving surface moisture, which is the competition between bleeding and evaporation, thus increasing the inter-

layer bond strength. Evaporation drying could be a major challenge for 3D concrete printing, which has no formwork to protect the material.

The present work aims to evaluate the water transport behavior and rheological properties of cement pastes incorporating nanoclay and diutan gum through measurements of bleeding, water retention, water loss to evaporation and steady-state shear rheology.

3.2. MATERIALS AND METHODS

3.2.1. MATERIALS

The cement used was a Type I Portland cement and its chemical and mineralogical compositions are reported in Table 1. The Blaine fineness is 402 m^2/kg. Distilled water was used in all mixes.

Chemical Oxide	SiO_2	Al_2O_3	Fe_2O_3	CaO	MgO	SO_3	Loss on ignition
Cement (%)	19.27	4.68	3.51	63	3.21	2.72	2.09

Table 1. Chemical composition of Type I Portland Cement.

Two VMAs were investigated – a clay and a gum. A highly purified form of the mineral attapulgite, or palygorskite, was the clay chosen for the study. Attapulgite/palygorskite is a magnesium alumino silicate clay with the theoretical formula of $Si_8Mg_8O_{20}(OH)_2(H_2O)_4 \cdot 4H_2O$ [20]. The preferred name according to the International Nomenclature Committee is palygorskite, although the name attapulgite is better known

commercially [18]. It is needle-like in structure – 1.75 μm in length and 30 nm in diameter [19]. Therefore, it can be referred to as a nanoclay. To disperse the nanoclay, it was blended with water in a Waring blender for 3 min to produce a suspension.

A commercially available diutan gum gel whose solid content is 1% by mass was the gum chosen for this study. The commercial gel is formulated to likely include superplasticizers. Diutan gum is a polysaccharide produced by Sphingomonas bacteria in fermentation [30]. It has high molecular weight and anionic charges. It could bind positively charged cement particles to increase viscosity, which is utilized for various applications in the construction industry and the petroleum industry [82].

All cement pastes were prepared using a hand mixer at a speed of 540 rpm. Cement pastes with nanoclay were prepared by adding the cement to the nanoclay suspension, then mixing for 3 min. Cement pastes with diutan gum were prepared by adding cement to water, mixing for 1.5 min, adding diutan gum gel, then mixing for another 1.5 min. Thus, the pastes prepared with the nanoclay and the diutan gum both had a total paste mixing time of 3 min. Pastes were prepared with a water-to-cement (W/C) ratio of 0.34, 0.44 or 0.6, depending on the test.

3.2.2. WATER TRANSPORT MEASUREMENTS

3.2.2.1. BLEEDING EXPERIMENTS

Just after mixing, pastes were poured into test tubes 29.4 mm in diameter and placed on a surface free of any vibration. After placement, the tube was sealed to prevent any water evaporation. The bleed water was

then extracted with a pipet at 20 min intervals during the first 60 min, then at 60 min intervals for the remainder of the test. To avoid disturbing the fresh suspension, a new sample was prepared for each time interval. Tested pastes had a W/C ratio of 0.6.

3.2.2.2. WATER RETENTION EXPERIMENTS

A modified version of the filter paper method (DIN 18 555-7 [83]) was used to estimate the water retention capacity of the cement paste. [84] validated that the filter paper method is reliable in simulating the actual water migration process that occurs through the interface between a fresh cement paste and a dry porous substrate. A plastic ring (inner diameter 37.4 mm, height 5.7 mm) was placed on top of a stack of creped, fast flow filter paper (Grade 415, VWR, USA) – the schematic is shown in Figure 26. Fresh cement paste was cast into the ring and left there for 20 min. Then, the ring and cement paste were carefully removed from the filter paper. The water retention capacity was calculated from the mass difference of the filter papers before and after the test, as follows:

$$\text{Water retention (\%)} = (1-W_{abs}/W_0) \times 100 \quad (15)$$

where W_{abs} is the water absorbed by the filter paper and W_0 is the mixing water in the cement paste sample. Tested pastes had a W/C ratio of 0.34.

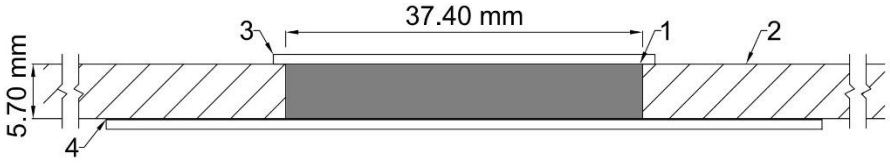

Figure 26. Test setup for determining the water retention of freshly-mixed cement pastes (1. Cement paste, 2. Plastic ring, 3. Cap to prevent evaporation, 4. Filter papers)

3.2.2.3. EVAPORATION WATER LOSS

A container (height of 47.5 mm, the diameter of 63 mm) was filled with cement paste, placed on a balance, and the mass loss was continuously measured. A commercial fan was positioned approximately 1 m from the setup. The condition was set to 25°C and 10% relative humidity. The mass loss data was smoothed by applying the Savitzky-Golay method of polynomial order 2 and points of window 20 by Origin software [85]. Tested pastes had a W/C ratio of 0.34, 0.44, and 0.6.

3.2.3. RHEOLOGICAL MEASUREMENTS

3.2.3.1. APPARENT VISCOSITY AND YIELD STRESS OF CEMENT PASTES

Shear rheological tests were performed in a stress-controlled rotational rheometer (HAAKE MARS III, Thermo Fisher Scientific, USA) with a 4-blade vane geometry set at a constant temperature of 25°C. The dimensions were as follows: vane diameter 22 mm, outer cup diameter 26.4 mm, and depth 16 mm. The surface of the outer cylinder was covered with 150-grit adhesive sandpaper to prevent slip.

As fresh cement pastes are thixotropic, it was necessary to pre-shear the pastes to ensure that all samples were at a reproducible reference state (i.e. equilibrium) at the start of each test. To obtain the static yield stress, the stress growth protocol was performed, where deformation was applied at a constant shear rate of 0.1 1/s. The shear stress progressively develops to a maximum value and then decays to an equilibrium value. The static yield stress is defined as the peak shear stress value [55]. As this method is destructive,

we prepared a new sample for each yield stress measurement. And the equilibrium value obtained during the pre-shear was taken to be the apparent viscosity. Tested pastes had a W/C ratio of 0.34 and 0.6.

3.2.3.2. INTERSTITIAL SOLUTION VISCOSITY

The cement paste pore solution was extracted using a centrifugation approach. Within 10 min after initial cement water contact, prepared cement paste was loaded into vials (36 mL paste in 1.5 mL vial) and centrifuged for 5 min at 4650 rpm. Then, the supernatant was collected, transferred to new vials, then centrifuged again for 5 min at 14500 rpm. The apparent viscosity of the final interstitial solution was tested by a rheometer with a parallel plate setup (diameter 17.5 mm). A logarithmic, increasing shear rate ramp from 1 1/s to 100 1/s was applied over 1000 s. Although a relatively long testing time was applied, inertial effects on the measured viscosity at low shear rates cannot be eliminated in the case of low viscosity polymer solutions (Figure 27) [86]. Theoretically, the shear rate does not have any effect if the solution behaves as a Newtonian fluid. At high diutan gum dosages, the viscosity value starts to depend on the shear rate as shear thinning occurs. In our case, at a relatively high dosage of 4%, the interstitial solution viscosity decays to equilibrium at 100 1/s. Therefore 100 1/s was selected to obtain the apparent viscosity of the studied polymer solution.

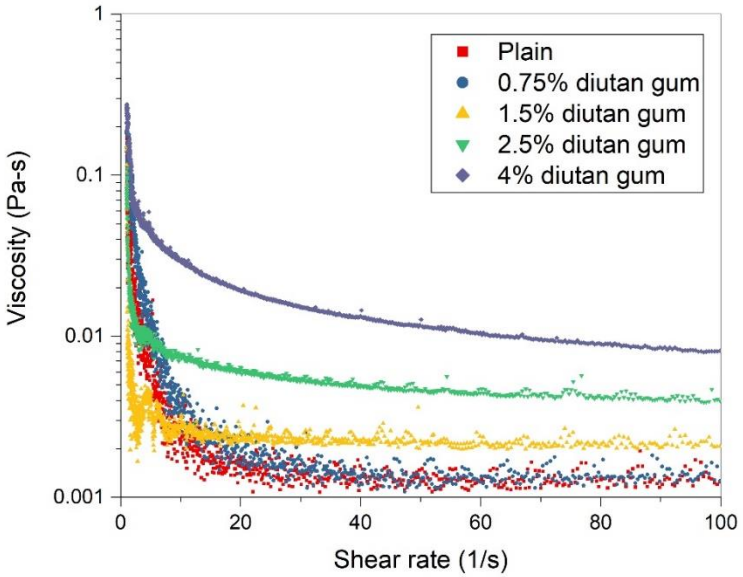

Figure 27. The representative viscosity of diutan gum in solution for various dosages in the polymer as a function of the shear rate. W/C=0.34.

In all the tests, at least three samples per mixture were tested, and the average was taken to be the representative value. Error bars are included in all plots.

3.3. RESULTS AND DISCUSSION

3.3.1. BLEEDING AND RHEOLOGICAL PROPERTIES (W/C=0.6)

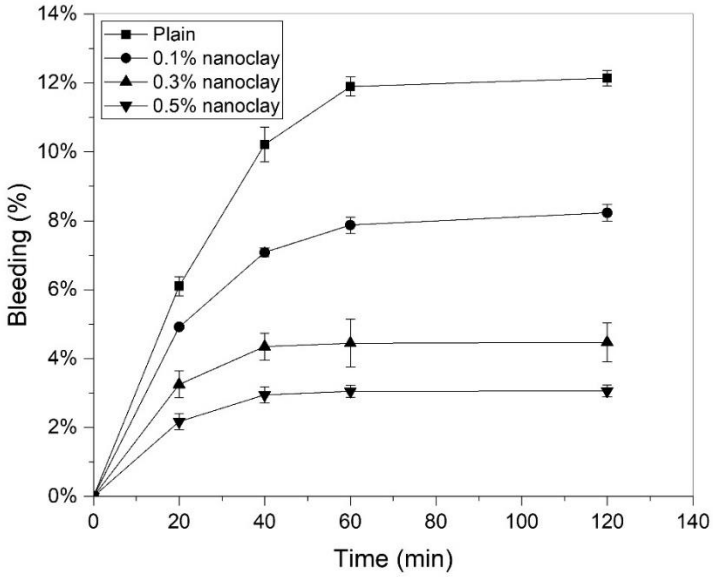

Figure 28. Bleeding behavior with different nanoclay addition. W/C=0.6.

Bleeding evolution was monitored for fresh cement pastes modified with different additions of nanoclay and diutan gum. Results of bleeding were correlated with those of static yield stress. Bleeding water accumulates either through progressive consolidation of the solid skeleton, termed “normal bleeding,” or through the formation of channels, which is usually characterized by a sudden increase in bleeding rate leading to a convex-shaped bleeding-time curve, termed “channeled bleeding” [87].

As shown in Figure 28, the plain cement paste and nanoclay modified cement paste shared similar bleeding features as normal bleeding – the bleeding rate is initially constant, followed by a period of diminishing rate before reaching equilibrium. In this case, bleeding can be considered as the process of self-weight

consolidation [87]. The permeability of cement pastes can be derived from the bleeding rate during the constant rate period utilizing Darcy's law:

$$K = Q\,\mu_0/Ag\Delta\rho \tag{16}$$

where K is the permeability of cement paste, Q is the water accumulation rate on the sample surface, A is the cross section of the test tube, μ_0 is the viscosity of the interstitial fluid, $\Delta\rho$ is the density difference between the particles and the liquid, and g is gravitational acceleration. Please note that this equation assumes that the inter-particle forces and other physical-chemical forces are independent of sample depth. As shown in Figure 29, the nanoclay does not have any notable effect on the viscosity of the interstitial fluid. Therefore rate of bleeding depends only on the permeability of the cement paste.

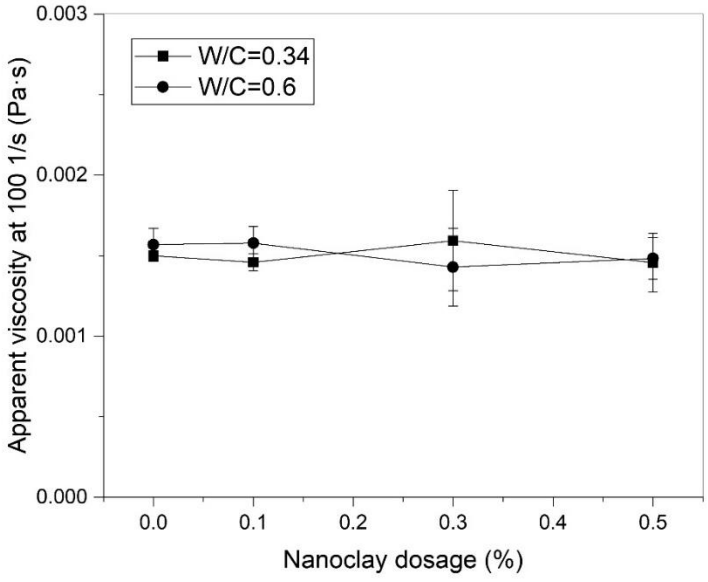

Figure 29. Effect of nanoclay on apparent viscosity of the interstitial solution.

The calculated permeability is shown in Figure 30. [27,28] suggested nanoclay can increase flocculation

strength and floc size, which may be attributed to the highly charged particle behavior. The nanoclay carries a negative charge on the faces and a positive charge on the ends [88]. Nanoclays tend to associate with each other by electrical attraction between positively charged edges and negatively charged surfaces, or absorb on oppositely charged surfaces of cement particles (i.e. C_3S is positively charged in cement suspensions [89]). Also, the fine size and high specific surface area of nanoparticles can provide more contact points and make the suspension structure more interconnected. The resultant structure has higher particle interactions (number and intensity), thereby lowering the permeability (Figure 30). This also leads to an increase in static yield stress, as shown in Figure 31, which is in agreement with previous work [25,90]. To add, clays have been found to refine the microstructure of hardened cement-based systems, as well [91,92].

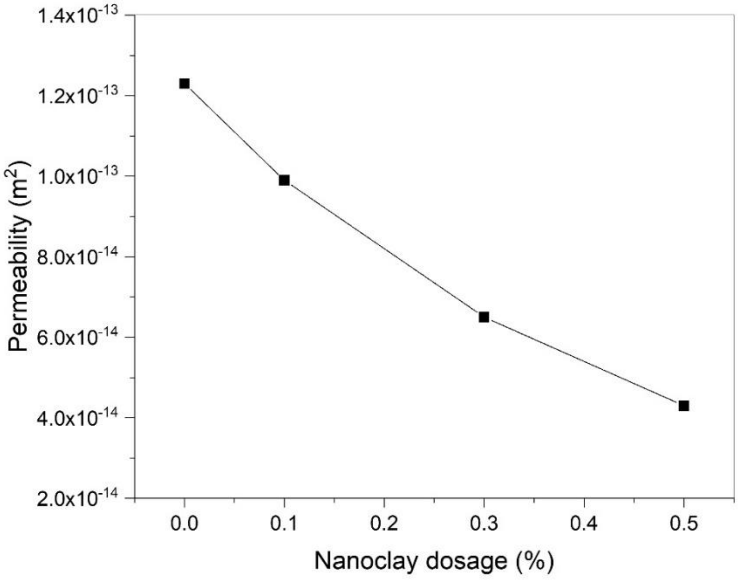

Figure 30. Permeability of cement pastes in bleeding test as a function of nanoclay dosage. W/C=0.6.

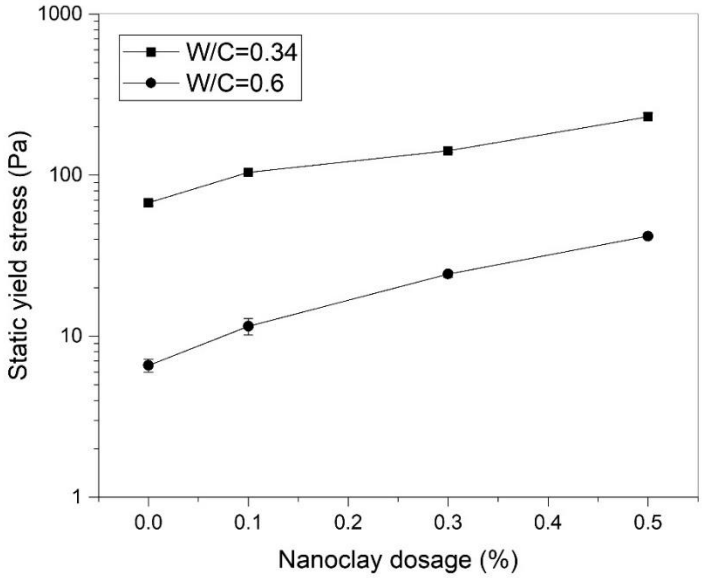

Figure 31. The static yield stress of cement pastes as a function of nanoclay dosage.

In addition to slowing the rate of bleeding, nanoclay addition caused the pastes to reach equilibrium earlier, i.e., 0.5% nanoclay paste reached equilibrium approx. 20 min earlier than plain cement (Figure 28). Bleeding stops when local gravitational forces due to the density difference between cement and water are compensated by the particle interactions, which increases with the local solid volume fraction. Due to its high specific surface area and surface charges, nanoclays induce stronger particle interactions, increase rate of thixotropic rebuilding, and introduce seeding effects, all of which will reduce the difference between local gravitational forces and particle interactions [93,94].

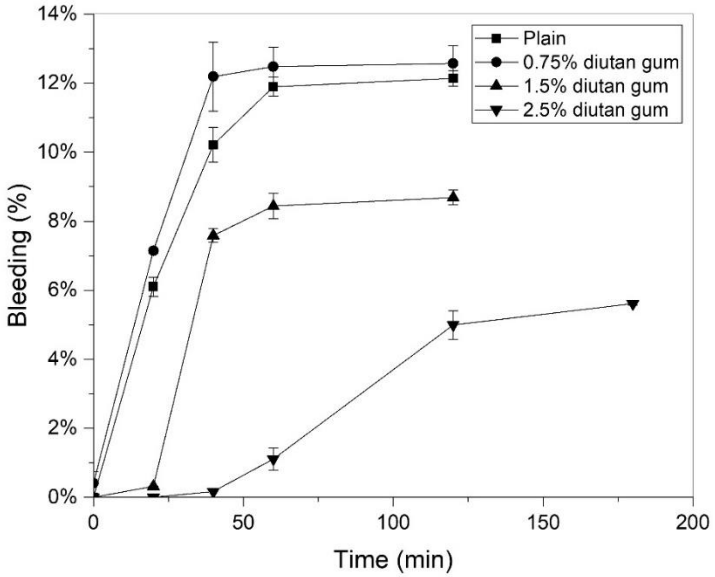

Figure 32. Bleeding behavior with different diutan gum dosages. W/C=0.6.

As shown in Figure 32, in contrast to the monotonic decrease observed with the addition of nanoclay (Figure 28), the diutan gum exhibited a more complex behavior. At a small addition (0.75%), the equilibrium bleeding level increased slightly. Beyond a critical concentration, the addition of diutan gum started to alleviate bleeding until there was no visible bleeding at 4% dosage (not plotted). At concentrations of 0 and 0.75%, the bleeding can be considered as "normal bleeding." At concentrations of 1.5% and 2.5% the bleeding initially progressed at a constant bleeding rate before a sudden increase occurred, after which equilibrium was eventually reached, resulting in a convex bleeding-time curve. This marks channel formation in the cement paste [95,96]. During bleeding, the interstitial solution flows upward and induces a viscous drag force on the cement particles. [96] suggested the viscous drag force causes a progressive local reorganization of the cement paste system. This reorganization leads to the formation of preferred water extraction channels. Research exploring the polysaccharide effect on interstitial solution viscosity suggests the existence of an "overlapping concentration" [14,86,97]. Below the overlapping concentration, individual polymer molecules exist in pore solutions as isolated coils. Above the overlapping concentration,

an exponential rise in viscosity is found as the coils begin to come into contact with one another. This is observed in Figure 33, which shows the viscosity of the interstitial solution of pastes modified with diutan gum. Here, the overlapping concentration is between 0.75% and 1.5%, above which the viscosity increases significantly.

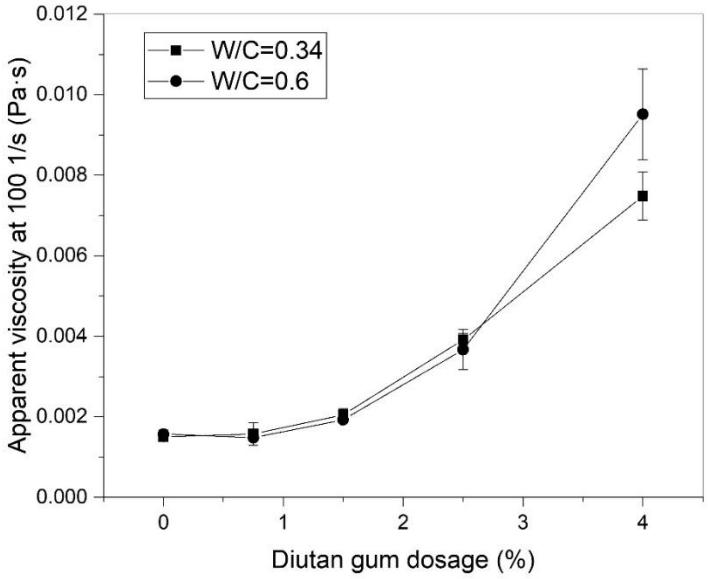

Figure 33. Effect of diutan gum on apparent viscosity of interstitial solution.

The permeability of diutan gum can be calculated by utilizing the bleeding rate during the constant bleeding period. The permeability values are plotted in Figure 34.

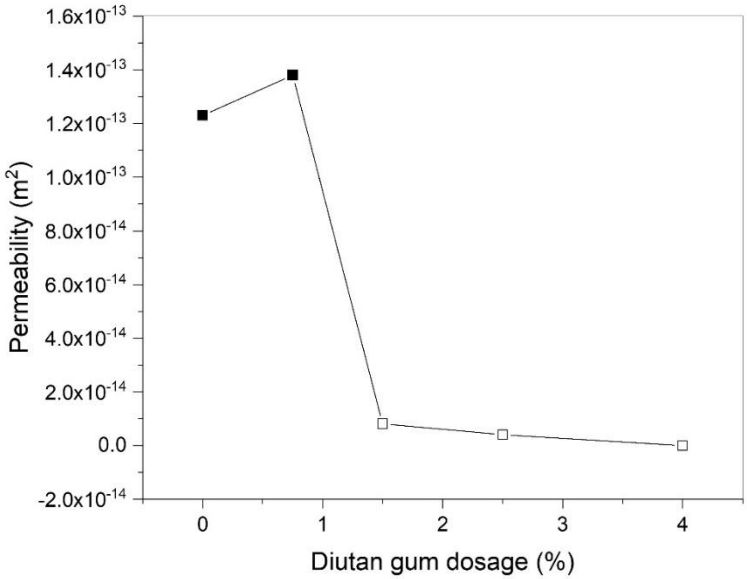

Figure 34. Permeability of cement pastes in bleeding test as a function of diutan gum dosage. As the interstitial solutions start to show shear thinning behaviors at high diutan gum dosages, the permeability can only be estimated approximately by equilibrium viscosity value as marked by open symbols. W/C=0.6.

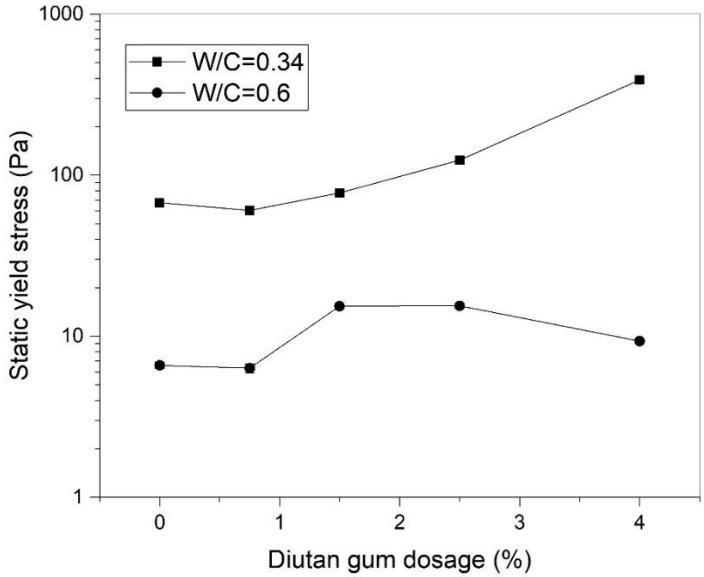

Figure 35. The static yield stress of cement pastes as a function of diutan gum dosage.

Below the overlapping concentration, the permeability increased from 1.23×10^{-13} m^2 to 1.38×10^{-13} m^2 and static yield stress decreased from 6.6 Pa to 6.33 Pa with 0.75% diutan gum addition compared to plain cement paste. This indicates less particle interaction in the structure of the cement paste (number and intensity) with isolated coils existing in the pore solution.

Above the overlapping concentration, at a concentration of 1.5%, the static yield stress increased and the permeability of the cement paste decreased dramatically due to interpenetration and entanglement of the polymer coils. As the concentration was increased further, the addition of diutan gum led to differing effects – a decrease of static yield stress with decrease in permeability. At 4%, the decrease in static yield stress was even more pronounced and there was no apparent bleeding. Thus, the absence of bleeding cannot be attributed to increased colloidal interparticle forces to resist gravity. Besides, the high interstitial solution

viscosity can only slow down the bleeding rate according to Darcy's law, not prevent it (assuming before set). There is another key factor that is responsible for the absence of bleeding. [98,99] reported that the polysaccharide aggregates that form above the overlapping concentration could induce jamming and obstruct flow through the cement paste suspension. The flow can be fully stopped if the concentration of polymer aggregates reaches a critical level [98,99]. Thus, the absence of bleeding may be attributed to diutan gum aggregates, which block the water flow path completely.

3.3.2. WATER RETENTION AND RHEOLOGICAL PROPERTIES (W/C=0.34)

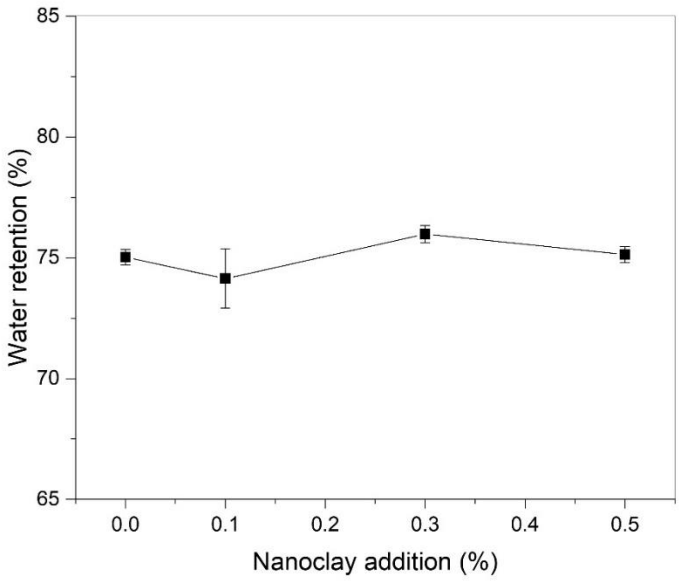

Figure 36. Water retention as a function of nanoclays dosage. Water-cement ratio is 0.34.

The water retention of fresh cement pastes modified with different additions of nanoclay and diutan gum was monitored. Results of water retention are correlated with those of paste and interstitial solution

viscosity. As clays have high water sorption capacity, they have been used as absorbents for grease, oil, water, and chemicals since the 1930s [20]. The characteristic structure of nanoclay provides a significant amount of pore space and permits the absorption of water and other organic materials both on the exterior surface and also in the open channels of the nanoclay crystals [21]. At 0.5% addition, assuming a nanoclay water sorption capacity of 200% by mass, from [100], the water retention should be approx. 3% higher than that of plain cement paste. However, as shown in Figure 36, water retention is independent of nanoclay dosage. A potential explanation is that the water sorption capacity in [100] was measured using plain water. When incorporated in cement pastes, as in the present study, the ions in the interstitial solution could modify the surface properties of the nanoclay [101], resulting in the deviation of the water sorption capacity.

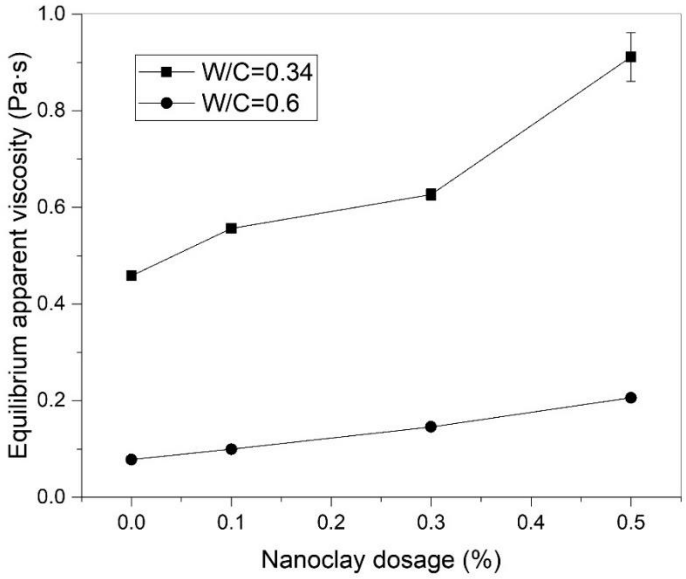

Figure 37. Equilibrium apparent viscosity of different nanoclay dosages under pre-shearing.

The relationship between the rheological properties of cementitious materials and their capacity to retain water has been widely studied [102]. Water retention capacity of cement-based materials is commonly

explained through mortar viscosity [102,103]. By comparing apparent viscosity (Figure 37) and water retention (Figure 36) of nanoclay modified cement pastes, the two parameters do not have the same tendency – apparent viscosity increases while water retention stays the same with nanoclay addition. However, water retention and viscosity of the interstitial solution (see Figure 29) have the same tendency, where neither parameter changes with nanoclay addition.

Although the nanoclay decreases the interstitial fluid mobility in the cement sample, as discussed in section 3.3, it does not affect the water transport in water retention tests, as shown in Figure 36. In both tests, water moves through the porous matrix of the cement paste in response to a gradient of pressure: local gravity forces induced by the density difference between cement and water in the bleeding test and suction force introduced by the filter paper in the water retention test. However, Darcy's law cannot be applied to the water retention results because the paste undergoes drying (approx. 25% of water is pulled from the cement paste by the filter paper) and Darcy's law requires the paste to be saturated. In this case, the influence of permeability on water loss is complex and needs further investigation.

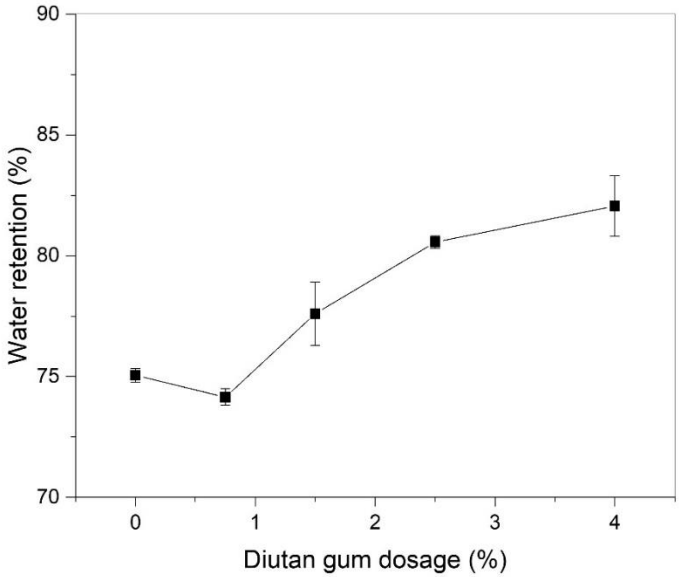

Figure 38. Water retention as a function of diutan gum dosage. Water-cement ratio is 0.34.

Like nanoclay, results clearly show that the water retention (Figure 38) and viscosity (Figure 39) of cement pastes with diutan gum do not show similar tendencies. Therefore paste viscosity is insufficient to explain water retention. Instead, some studies have shown that increase in interstitial solution viscosity correlated well with increase in water retention [104]. This is consistent with what we observed in pastes with both nanoclay and diutan gum addition (Figure 33 and Figure 38, respectively). Moreover, some studies highlighted the formation of polymer aggregates as the origin of higher interstitial solution viscosity and higher water retention [86,98]. To better understand the behavior of diutan gum in cement mixes, we examined the rheological results with different diutan gum concentration.

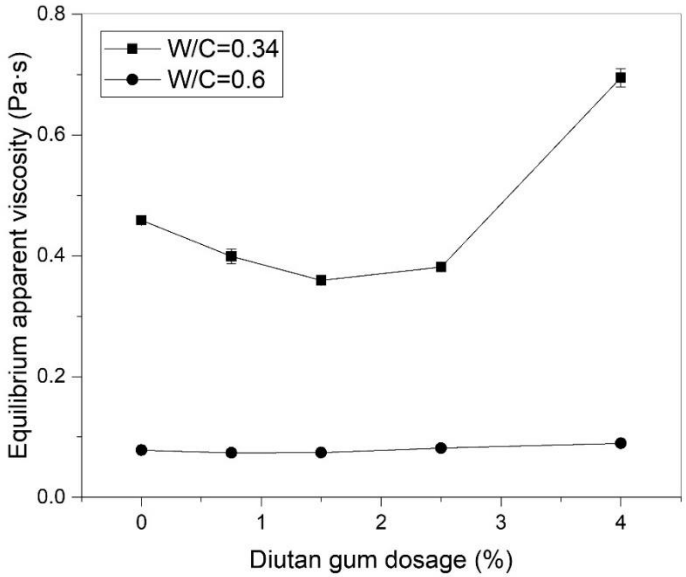

Figure 39. Equilibrium apparent viscosity of different diutan gum dosage under pre-shearing.

Below the overlapping concentration, there was a decrease in equilibrium apparent viscosity, as shown in Figure 39. The lower final equilibrium apparent viscosity may be due to the alignment of polymer molecules. However, a sharp increase in the equilibrium viscosity occurs at 4% addition. As discussed previously, higher polymer additions led to increased interstitial solution viscosity (Figure 33), indicating that polymer aggregates form at these concentrations [14,97–99]. It is hypothesized that the polymer aggregates existing in interstitial solutions may bridge with cement particles to form a strong polymer-cement network that is difficult to break down by shearing, resulting in an increase in apparent viscosity (Figure 39) and static yield stress (Figure 35).

In comparing W/C ratio 0.34 and 0.6, if we look at the static yield stress results, the addition of diutan gum had differing effects: a remarkable increase with W/C ratio 0.34 and a significant drop with W/C ratio 0.6. As mentioned above, the former may be attributed to the formation of a strong polymer-cement

network, which cannot be broken down under applied shear. In the latter case, as the system is more diluted, the diutan gum aggregates may form but are not strong enough to resist the shearing. Furthermore, the formed aggregates can increase the distance between cement particles, which will lead to a decay of colloidal force.

3.3.3. EVAPORATION WATER LOSS (W/C=0.34 AND 0.6)

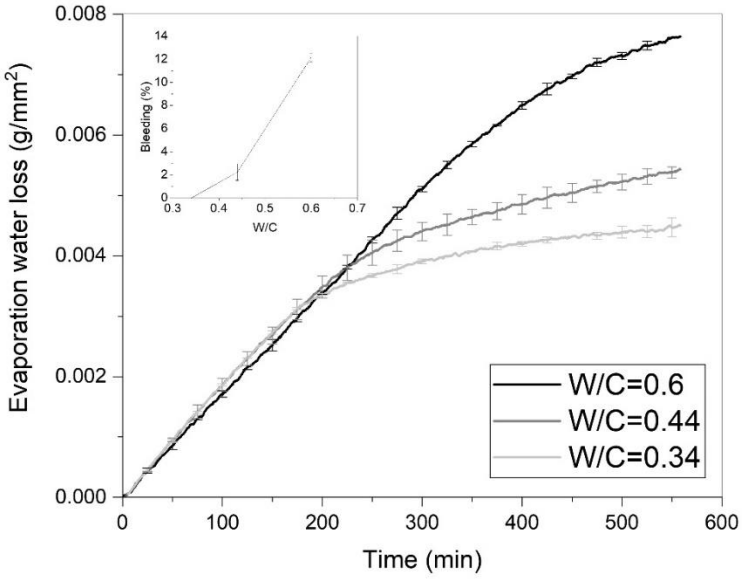

Figure 40. Specific mass change with different W/C ratios.

The effects of W/C ratio and the addition of nanoclay and diutan gum on the rate of evaporation of fresh cement pastes were investigated. Lura et al. [105] explain the mechanisms governing the drying behavior of cementitious materials utilizing the drying model of gels presented by [106]. First, there is evaporation of accumulated bleed water, where the rate of evaporation is the same as that of bulk water. The second phase is a constant rate period where air-liquid menisci and capillary pressure develop in the top layers and

compress the solid skeleton, resulting in the pore fluid surfacing and evaporating. In the final phase, the capillary pressure can no longer compress the solid skeleton and water is drawn from the inside of the specimen. The evaporation rate decreases significantly.

Figure 36 shows the effect of W/C ratio on evaporation water loss. Immediately after placement, at W/C=0.44 and 0.6 water accumulated on top of the sample because the bleeding rate was faster than the evaporation rate (shown in the inset in Figure 36). Thus, after the sample was exposed to air flow, the rate of water loss from the cement paste was close to the rate of free evaporation of water. Once the bleed water dried out (for example, the sample dried out at around 190 min at W/C=0.6), water loss continued at a constant rate as water was pushed to the surface and the sample experienced compression due to the formation of air-liquid menisci. The rate of constant evaporation period was independent of the W/C ratio, and the bleed water did not affect the evaporation rate. However, the lower W/C ratio shortened the duration of the constant rate period. One possible explanation is that a higher W/C ratio causes a higher degree of dilution of cement in the suspension, which may result in a lower rate of hydration and reduced/retarded heat of cement hydration in early ages [107]. This test is insufficient to fully understand the role of admixtures on evaporation loss, and thus motivates further study implementing techniques, e.g. neutron diffraction, to track water movement.

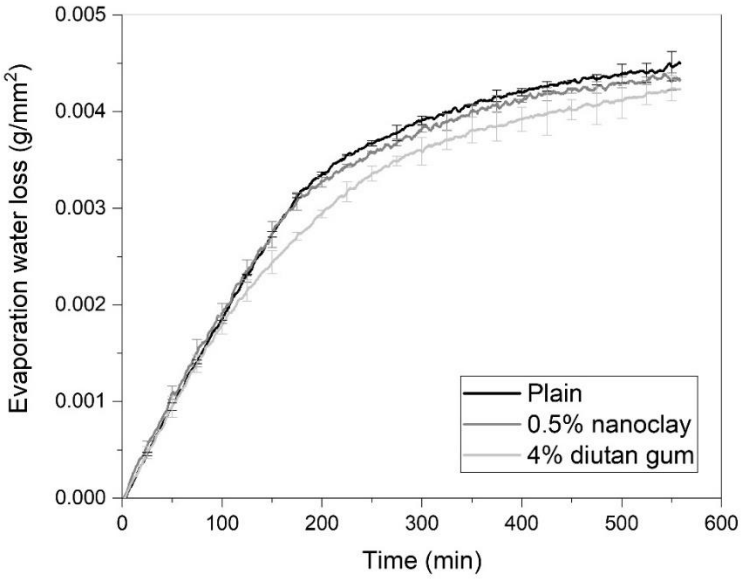

Figure 41. Evaporation with nanoclay and diutan gum. W/C=0.34.

As shown in Figure 41, the nanoclay did not have a notable influence on evaporation water loss at W/C = 0.34. From the above results and analysis (section 3.3), the nanoclay provides more particle interactions (number and intensity), higher flocculation strength and more contact points. However, due to the relatively high pressure gradient applied to the samples, these interactions do not resist water loss due to evaporation. The diutan gum sample had the same evaporation rate as the plain cement in the first hour. But after that, it showed a faster deviation from the linear evaporation period and went on to exhibit a lower evaporation rate. [108] demonstrates the formation of fibrillose films on the surface of evaporation samples. The rheological results indicated the formation of a strong polymer-cement network, which may at least partially explain the reduction in evaporation rate. Similar trends were seen at W/C = 0.6.

The absence of bleeding water with both nanoclay or diutan gum addition did not curb water loss due to evaporation. In addition, considering the retarding effect of diutan gum on hydration [90], it would have

longer evaporation water loss time before setting. Therefore for practical purposes, neither nanoclay nor diutan gum provided resistance to plastic shrinkage. Therefore other methods are needed for mitigation in 3D concrete printing, e.g., curing agents.

3.4. CONCLUSIONS

This study evaluated the effect of attapulgite/palygorskite clay and diutan gum on the rheological and water transport properties of cement pastes. The key findings are as follows:

1. A monotonic decrease in bleeding was observed with the addition of nanoclay. Cement paste with nanoclay has higher particle interactions, thereby lowering permeability and increasing static yield stress.
2. Below a critical concentration, bleeding increased with increasing dosage of diutan gum. Above a critical level, the cement system exhibited a decrease in bleeding. The addition of diutan gum led to differing effects on yield stress and permeability, which marks the formation of diutan gum aggregates that could block the water flow path and mitigate bleeding.
3. Within the range studied, water retention was independent of nanoclay addition. Results of water retention correlated well with those of interstitial solution viscosity. Diutan gum results highlighted the formation of polymer aggregates as the origin of higher interstitial solution viscosity and higher water retention capacity.
4. The rate of constant evaporation period was independent of W/C ratio, and bleed water was not found to affect evaporation rate.
5. The nanoclay did not have a notable influence on evaporation water loss. Although diutan gum showed slightly lower evaporation rates, in practical terms neither nanoclay nor diutan gum

provided resistance to plastic shrinkage. Therefore, other methods will be needed to ensure proper curing for 3D concrete printing, e.g., curing agents.

CHAPTER FOUR

4. EVALUATION OF STRUCTURAL BUILD-UP OF FRESH CEMENT PASTES

4.1. INTRODUCTION

In oil well cementing, loss of circulation occurs when drilling fluid or cement slurry flows into weak geological formations instead of returning up the annulus. The formation where circulating fluid can be lost is called the thief zone. It has been shown that thixotropic cement slurries are effective for solving this issue [4]. After loss of circulation is detected, these slurries are prepared and pumped downhole to seal the formation. During pumping, its structure continuously breaks down, allowing it to flow. But once it enters the thief zone, the velocity of the leading-edge decreases and the structure begins to recover. The resistance of the slurry to flow increases as its structure builds up, effectively plugging the thief zone. A major factor for successful plugging is the rate of structural build-up immediately after the cessation of flow, especially during the first few minutes. Although linear models are commonly used to describe the early structural build-up, the behavior during the first few minutes is either not reported [109] or faster than the linear portion [35,39,110]. In this study, a simple non-linear thixotropic model is proposed.

Depending on the depth of the thief zone, thixotropic cement systems will experience different shear durations during pumping. Also, it is known that when pumping stops, there is residual stress that remains in the system [58]. Thus, it is also critical to know how shear time and residual stress during resting influence the behavior of structural build-up in fresh cementitious systems.

Two parameters, static yield stress measured by stress growth and elastic modulus measured by small amplitude oscillatory shear (SAOS), are widely used to characterize the structural build-up of cement slurries in the petroleum industry [4]. In contrast with a protocol like stress growth, in which rotational shear breaks down the structure of the material, SAOS is a non-perturbing test as the applied oscillatory strain amplitude is very low. This also makes SAOS less time consuming and simpler to run. [111] pointed out the similarity between elastic modulus and static yield stress development with time of plain cement paste and cement paste with high-range water-reducing admixture. However, Roussel et al. [35] suggest that these two parameter of standard cement paste may find different structural origins. Therefore it is necessary to examine both the static yield stress and elastic modulus evolution of different types of cement pastes, such as those modified with viscosity modifying admixtures, to elucidate the various origins of structural build-up. More evidence of discrepancy between static yield stress and elastic modulus evolution is presented in this study.

In the present study, we first present a simple thixotropy model to describe the non-linear structural build-up of static yield stress and storage modulus, measured by a stress growth protocol and SAOS, respectively. We utilize this model to examine how pre-shear and rest condition (time and stress applied) affect the structure of fresh cement paste. Then, the effects of two VMAs (nanoclay and diutan gum) on the structural build-up are compared.

4.2. MATERIALS AND METHODS

4.2.1. MATERIAL PROPERTIES

The cement used is a Class H oil well cement and its chemical and mineralogical compositions are reported in Table 2. The Blaine fineness is 323 m^2/kg. Distilled water is used in all mixes.

	SiO_2,%	Al_2O_3,%	Fe_2O_3,%	SO_3,%	CaO,%	MgO,%	Loss of Ignition, %	C/S	C/A	C_3S,%	C_2S,%	C_3A,%	C_4AF,%
Compound Amount	22.0	2.8	4.4	2.8	64.4	2.6	1.0	2.9	23.0	62.0	16.3	0	13.4

Table 2. Chemical composition of Class H oil well cement.

Two VMAs are investigated – a clay and a gum. A commercially available, highly purified form of the mineral attapulgite, or palygorskite, is the clay chosen for the study. It is needle-like in structure – 1.75 μm in length and 30 nm in diameter [112]. Therefore, it can be referred to as nanoclay. To disperse the nanoclay, it is blended with water in a Waring blender for 3 min to produce a suspension. A commercially available diutan gum gel whose solid content is 1% by mass is the gum chosen for this study. Diutan gum is a high molecular weight, microbial and anionic polysaccharide produced by aerobic fermentation. Diutan gum has two-rhamnose side chains and its molecular weight is about 2.88 to 5.18 million Daltons [113]. The mix compositions are given in Table 3. Mix compositions of pastes.. Pastes with 0.3% nanoclay powder and 2.5% diutan gum gel addition by mass of cement (labeled NC and DG) are tested. The solid volume fraction is kept constant for all mixes.

Mix	Cement (g)	Distilled water (g)	Nanoclay (g)	Diutan gum gel (g)	Solid volume fraction (%)
Cement	50	17	0	0	48.29
NC	49.82	17	0.15	0	48.29
DG	50	15.75	0	1.25	48.32

Table 3. Mix compositions of pastes.

All cement pastes are prepared using a hand mixer at a speed of 540 rpm. Cement pastes with nanoclay are prepared by adding the cement to the nanoclay suspension, then mixing for 3 min. Cement paste with diutan gum is prepared by adding cement to water, mixing for 1.5 min, adding diutan gum gel, then mixing for another 1.5 min. So the pastes prepared with the nanoclay and the diutan gum both have a total paste mixing time of 3 min.

After mixing, the pastes are covered with plastic film to prevent evaporation and left to rest at temperature 25 ± 3 °C for 95 min to make sure they are under the dormant period when tested. Before loading the sample into the rheometer for testing, the pastes are mixed with a hand mixer for 1 min to ensure a homogeneous state.

4.2.2. TESTING PROCEDURES

4.2.2.1. HEAT OF HYDRATION

The rate of hydration of pastes are measured in an isothermal calorimeter (TAM Air, Thermometric AB, Sweden) by monitoring the heat flow generated at a constant temperature of 25°C. For each sample, approximately 5 g of paste is added to a glass bottle and placed in the calorimeter. The signal takes 45 min to stabilize, thus the main peak due to dissolution is not completely captured. Each sample is replicated three times and the final hydration graphs are based on the average.

4.2.2.2. RHEOLOGICAL MEASUREMENTS

4.2.2.2.1. Equipment and geometry

Shear rheological tests are performed in a stress-controlled rotational rheometer (HAAKE MARS III, Thermo Fisher Scientific, USA) with a 4-blade vane geometry set at a constant temperature of 25°C. The dimensions are as follows: vane diameter is 22 mm, outer cup diameter is 26.4 mm and depth is 16 mm. The surface of the outer cylinder is covered with 150-grit adhesive sandpaper to prevent slip. All the measurements are performed at least three times to ensure the reproducibility of the results.

To obtain shear stress τ and shear strain rate $\dot{\gamma}$ from applied torque and measured angular velocity of the vane, respectively, the following geometric mean relationships are used:

$$\dot{\gamma}=\frac{2R_bR_c\Omega}{R_c^2-R_b^2} \tag{17}$$

$$\tau=\frac{1}{2\pi HR_b^2}\cdot A\cdot T \tag{18}$$

where R_b is the radius of the vane, R_c is the radius of the cup, and Ω is the angular velocity of the vane in Equation 17; T is the applied torque, H is the depth of the vane, and A is the calibrated stress factor (A = 0.69) in Equation 18.

4.2.2.2.2. Pre-shearing and resting protocols

As fresh cementitious materials are thixotropic, it is necessary to pre-shear the pastes to ensure that all samples are at a reproducible reference state at the start of each test. As shown in Figure 44, at 260 1/s the apparent viscosity reaches equilibrium at 1500 s. Different pre-shear times at 260 1/s are investigated and discussed in Section 4.1. Various shear stresses applied during resting are studied and discussed in Section 4.2.

4.2.2.2.3. Static yield stress test

To obtain the evolution of static yield stress, we perform stress growth measurements by applying deformation at a constant shear rate of 0.1 1/s. The shear stress progressively develops to a maximum value and then decays to an equilibrium value, as shown in Figure 42. The static yield stress is defined as the peak shear stress value [55]. As this method is destructive, we prepare a new sample for each yield stress measurement.

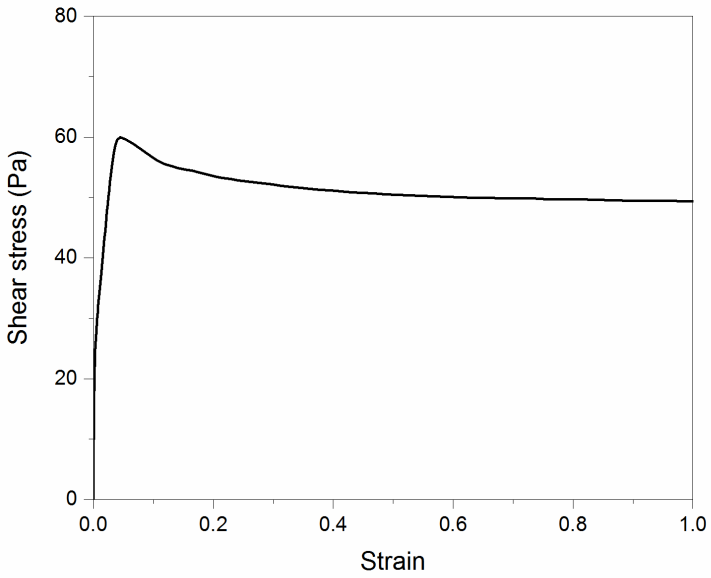

Figure 42. Typical shear stress vs strain when shearing a cement paste at a constant shear rate 0.1 1/s.

4.2.2.2.4. Small amplitude oscillatory shear (SAOS) test

To obtain the evolution of storage modulus, we perform SAOS time sweep measurements. The details of the method can be found elsewhere [114]. As an initial step, a strain sweep is conducted to determine the linear viscoelastic domain (LVED) where within the LVED the storage modulus G' is independent of applied shear strain amplitude, as shown in Figure 43. In a similar manner, a frequency sweep is performed

to determine the LVED, as well. Based on the sweeps, an angular frequency of 1 Hz and strain value of 0.0001 are chosen for the applied strain to measure storage modulus evolution.

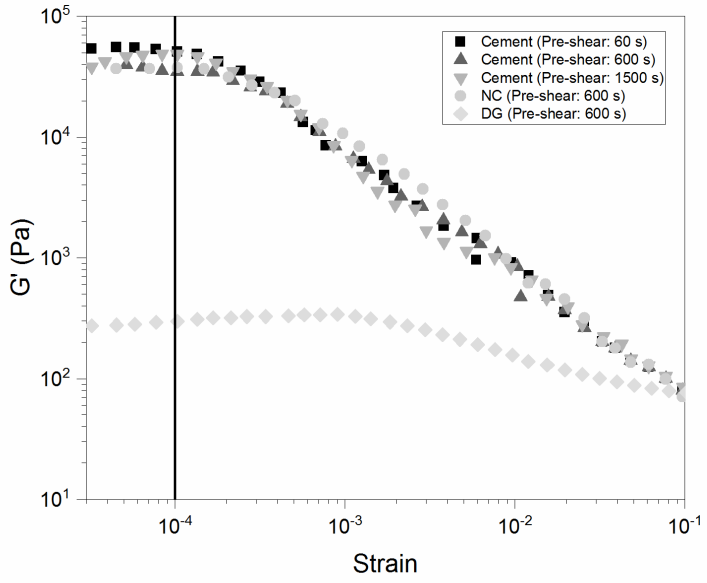

Figure 43. Storage modulus as a function of shear strain at angular frequency 1 Hz.

4.3. SIMPLE THIXOTROPY MODEL

Cheng and Evans [77] proposed an empirical thixotropy model to describe the time dependency of thixotropic materials. It consists of a kinetics model and a constitutive equation. The kinetics model describes the rate of change of structural parameter λ, and the constitutive equation expresses the rheological behavior for a given λ.

Based on the same framework as Cheng and Evans [77], our proposed kinetics model is controlled by a general relaxation process that reflects restoration of an equilibrium state from a non-equilibrium condition.

In the relaxation process, the rate of approach of equilibrium is proportional to the distance from equilibrium [115],

$$\frac{\partial\lambda}{\partial t}=-\frac{1}{\theta}\left(\lambda-\lambda_{equil}\right) \tag{19}$$

where λ_{equil} is the structure at equilibrium and θ is the relaxation time. The solution of this equation is

$$\lambda=\lambda_{equil}+(\lambda_0-\lambda_{equil})e^{-t/\theta} \tag{20}$$

Note that λ is a dimensionless parameter that varies between zero (fully broken down state) and unity (fully interconnected state). The structural parameter λ represents the degree of "structure" in a thixotropic system. As shown in a previous study [35], there exist two "structures" with different scales in cement pastes. They will be described briefly here:

1. Macroscopically, the static yield stress increases at rest due to flocculation and apparent viscosity decreases under shear flow due to de-flocculation [40]. If we neglect the effects of hydration, static yield stress is governed by particle force and particle arrangement from a first principle analysis of static yield stress, as proposed by R.J. Flatt and P. Bowen [36]. Distinguishing the origin of the exact origin of build-up of static yield stress is beyond the scope of this study. Thus, we described yield stress increase as a general flocculation process, which is in accordance with other publications [39,40]. λ_{flocs} represents the degree of flocculation in cement paste in this case.
2. Microscopically, at the strain limit of the LVED (an order of a few 10^{-4}), the relative movement of two neighboring cement particles has a range of a couple nm. The increase in strain beyond the LVED results in a significant drop in storage modulus, which can be associated to the breakage of links between cement particles that are a few nm [35]. [35] suggests that these links are calcium silicate hydrated (C-S-H) "bridges" at the pseudo contact zones [41]. So, we assume that the applied SAOS with a strain amplitude of 0.0001 probes the evolution of C-S-H nucleation. $\lambda_{C\text{-}S\text{-}H}$ represents the degree of C-S-H network in cement paste in this case.

Previous research [39,110] has shown that both static yield stress and storage modulus increase more rapidly at first and then increase linearly with resting time. So, the constitutive equations can be written as a function of static yield stress and storage modulus, respectively, as follows:

$$\tau=\tau_0+c\lambda_{flocs}+A_{thix}t \quad (21)$$

$$G'=G_0^{'}+c\lambda_{C\text{-}S\text{-}H}+G_{rigid}t \quad (22)$$

where τ_0 is initial static yield stress, G'_0 is initial storage modulus, c corresponds to the fully developed λ (λ=1) condition, A_{thix} is the rate of linear evolution of static yield stress and G_{rigid} is the rate of linear evolution of storage modulus. Good fitting with the model would support the existence of the two structures and corresponding kinetics and allow quantify the effect of pre-shear and VMA addition on each.

4.4. RESULTS AND DISCUSSIONS

4.4.1. EFFECT OF PRE-SHEAR

As pre-shear starts, we assume that λ decreases from unity to zero following equation (23):

$$\lambda_{flocs}=e^{-t/\theta} \quad (23)$$

We assume A_{thix} is negligible as the process is controlled by de-flocculation. Then, apparent viscosity evolution under constant shear rate can then be fitted from equation (24):

$$\eta=\eta_0+ce^{-t/\theta} \quad (24)$$

Figure 44 shows viscosity evolution of cement paste described by parameters η_0=0.33, c=0.51, and θ=322.58. Residual λ_{flocs} values at the end of each pre-shear time are shown in Table 4. As expected, shorter pre-shear time leaves a more intact structure. In the following section we will discuss how pre-shear and the corresponding λ_{flocs} effects the evolution of static yield stress and storage modulus.

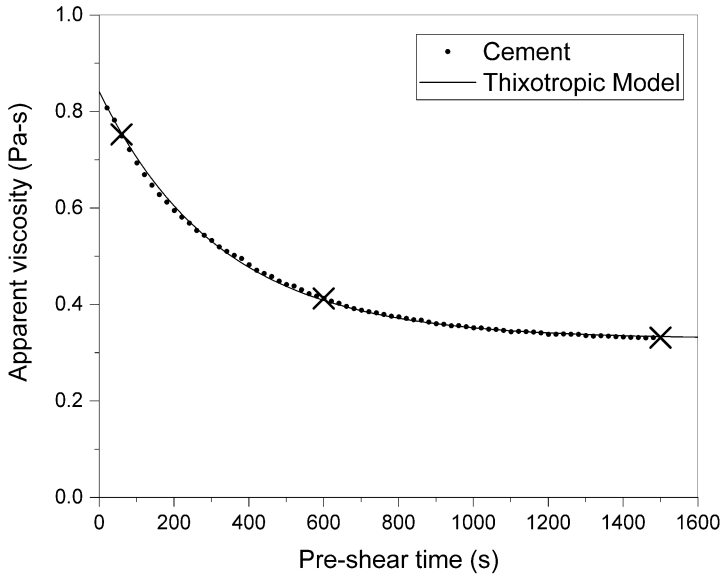

Figure 44. Apparent viscosity evolution of cement paste.

Pre-shear time (s)	60	600	1500
$\lambda_{flocs\_residual}$	0.83	0.16	0.01

Table 4. Residual structural parameter λ with different pre-shear times.

4.4.1.1. Effect of pre-shear on structural build-up obtained by static yield stress tests

During rest, λ_{flocs} will recover back from $\lambda_{flocs\_residual}$ to 1 following equation (25):

$$\lambda_{flocs}=1+(\lambda_{flocs\_residual}-1)e^{-t/\theta} \quad (25)$$

The thixotropy model then becomes:

$$\tau=\tau_0+c(1+(\lambda_{flocs\_residual}-1)e^{-t/\theta})+A_{thix}t \quad (26)$$

Figure 45 shows the experimental results for static yield stress evolution with the model fitting. And Table 5 presents the model parameters. Good fitting with the thixotropy model supports that there are two kinetics

of structural build-up at rest: structure evolves rapidly at first and then increases linearly. This is with the exception of the paste subjected to 60 s, which is linear throughout. After this relatively short shearing time, compared to 600 s and 1500 s, most of the floc structure remains unbroken ($\lambda_{flocs\_residual}$=0.83, Table 3). As $\lambda_{flocs\_residual}$ is so close to 1, λ_{flocs} evolution is difficult to detect and only the linear portion of the static yield stress evolution is captured.

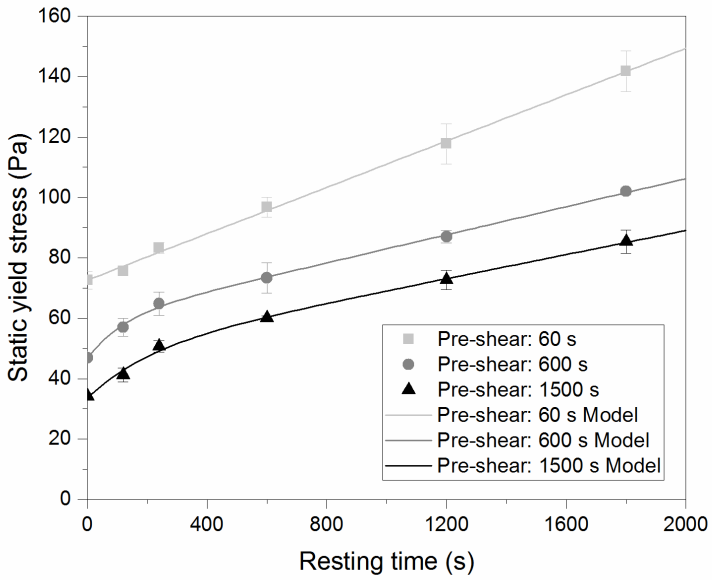

Figure 45. Evolution of static yield stress with different pre-shear durations.

Pre-shear conditions	$\lambda_{flocs\_residual}$	τ_0 (Pa)	Relaxation time θ (t)	c (Pa)	A_{thix} (Pa/s)
260 1/s-60 s	0.83	72.63	-	-	0.038
260 1/s-600 s	0.16	44.11	116.96	15.64	0.023
260 1/s-1500 s	0.01	33.34	204.92	15.86	0.020

Table 5. Thixotropic parameters of static yield stress tests with different pre-shear durations.

Figure 46 presents the static yield stress at t = 0 and A_{thix} as a function of $\lambda_{flocs\_residual}$. As expected, higher $\lambda_{flocs\_residual}$, corresponding to shorter pre-shear and a more intact floc structure, leads to higher initial stress. Also, lower $\lambda_{flocs\_residual}$ leads to lower A_{thix}, indicating the kinetics of rebuilding are relatively slow when the sample is subjected to a longer shearing time. Similar re-flocculation behavior has been observed by others in clay suspensions by monitoring floc size using scanning laser microscopy [116], where longer shearing time slowed the recovery of floc size.

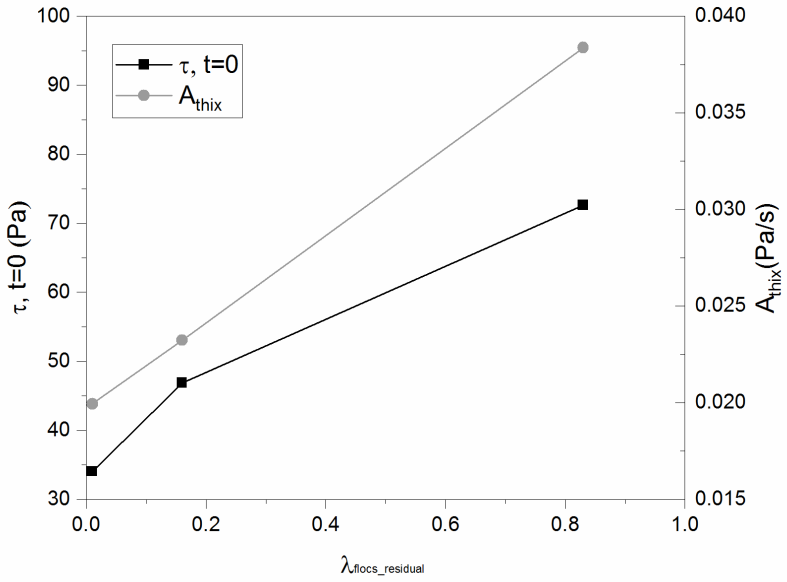

Figure 46. Static yield stress at t=0 and A_{thix} in dependence of residual λ.

4.4.1.2. Effect of pre-shear on structural build-up obtained by saos tests

Figure 47 shows the experimental results for storage modulus evolution with the model fitting. And Table 6 presents the model parameters. Here we assume that the initial storage modulus G_0'G'_0 is zero and $\lambda_{C\text{-}S\text{-}H\_residual}$ is zero for all pre-shear durations and the thixotropy model becomes,

$$G' = c\,(1-e^{-t/\theta}) + G_{rigid}\,t \quad (27)$$

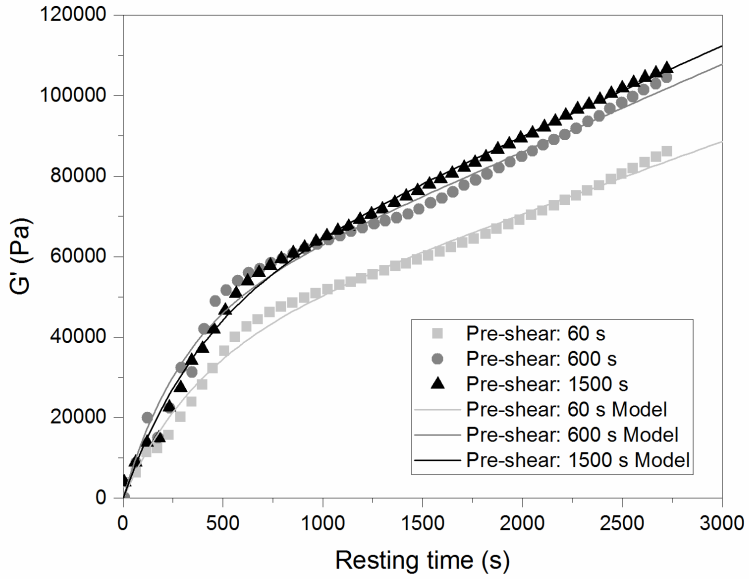

Figure 47. Evolution of storage modulus with different pre-shear durations.

Pre-shear conditions	Relaxation time θ (t)	c (Pa)	G_{rigid} (Pa/s)	L (1/s)
260 1/s-60 s	377.36	34788.23	17.95	0.00052
260 1/s-600 s	286.53	42449.35	21.79	0.00051
260 1/s-1500 s	386.10	45477.02	22.31	0.00049

Table 6.Thixotropic parameters of SAOS tests with different pre-shear durations.

From other works [35,110], there exists two structuration kinetics due to C-S-H nucleation evolution: a short-term percolation that occurs within a few hundred seconds and then afterwards a long-term

rigidification phase. The percolation process is mainly characterized by a relaxation process of $\lambda_{C\text{-}S\text{-}H}$ (parameter c and θ). The rigidification evolves linearly with time, which is characterized by G_{rigid}.

We first note that the rigidity of the percolated C-S-H "bridge" network (parameter c) is higher for 600 s and 1500 s compared with 60 s (Table 6). Longer shearing time leads to a decrease in the average floc size and an increase in floc number [27]. Furthermore, the spacing between agglomerates is a function of the solid volume fraction and size of the agglomerates. At a certain solid volume fraction, smaller particle size means smaller interparticle spacing [117,118]. Under longer shearing time, it would be possible for there to be more pseudo-contact points, which would provide more preferential sites for C-S-H nucleation and lead to a more percolated C-S-H network (parameter c). The difference in parameter c between 600 s and 1500 s is relatively moderate along with the relatively moderate decrease in the average floc size and an increase in floc number which is represented by residual λ_{flocs}

Moreover, to analyze the linear evolution with different shear durations, we define the linear evolution index L: $L=G_{rigid}/c$. L may be considered as an parameter that reflects the growth rate of C-S-H, which translates to either strengthening of the bond at each contact point or increase in the number of contact points in the formed percolated network. As shown in Table 5, although G_{rigid} increases along with c, L values are nearly the same with different shear durations. The relationship between G_{rigid} and c verifies the claim [35] that the origin of the linear evolution can be tied to the rigidification of the percolated network due to hydration.

Finally, in many thixotropic systems such as bentonite suspensions and mustard, measurement of storage modulus through SAOS shows quantitatively similar evolution as that of static yield stress [58]. Thus, as a less time consuming, non-perturbing test, it can be considered as a desirable approach to characterize stress-bearing ability over time for these thixotropic systems. However, for cement pastes, storage modulus has

quite different time evolutions compared to static yield stress in response to pre-shear due to the two different “structures” in the paste, as was discussed in Section 3.

4.4.2. EFFECT OF SHEAR STRESS DURING RESTING

To get reproducible results, zero stress is applied during rest. Note that it is very different to apply a zero shear rate after a pre-shear: as various residual stresses will remain in the paste at zero shear rate, the starting value of each static yield stress test will not be the same. So, the initial condition of the test will be ill-defined [119]. However, the stress is non-zero during resting in many applications. For example, in oil well cementing and concrete pumping, which are driven by a piston and thereby shear rate controlled, the stress at flow cessation is likely to be near the dynamic yield stress. If the static yield stress is dependent of the stress applied during resting, there will be a discrepancy between the stress needed to reinitiate flow and the static yield stress measured through rheometric methods performed after zero stress. Therefore, we applied different stresses during rest to examine its effect on static yield stress. Before performing the static yield stress measurement, we initialize the stress to 0 Pa for 5 s.

Figure 48 shows the results of static yield stress at different applied shear stress levels during rest for cement paste. It is similar to what is observed in other thixotropic materials [58], where the static yield stress is strongly dependent on the shear stress applied during rest. As shown in Figure 49, the peaks in the response occur at progressively higher stress and lower strain, indicating a stiffer structure is formed, as increasing stress is applied. It is likely due to the jamming introduced by shear stress [58]. In practice, the residual stress that remains in the material as flow stops would increase its static yield stress, thus increasing the stress needed to reinitiate flow. So, to accurately characterize the build-up behavior for various practical applications, such as cement pumping, extrusion and casting, by rheometric method, attention should be directed to the rest condition, i.e. stress controlled or shear rate controlled.

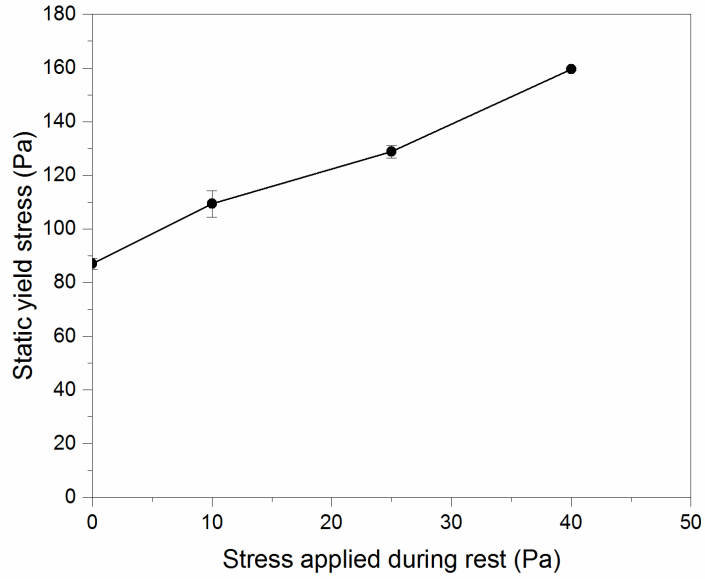

Figure 48. Influence of different shear stress levels on static yield stress at 20 min resting.

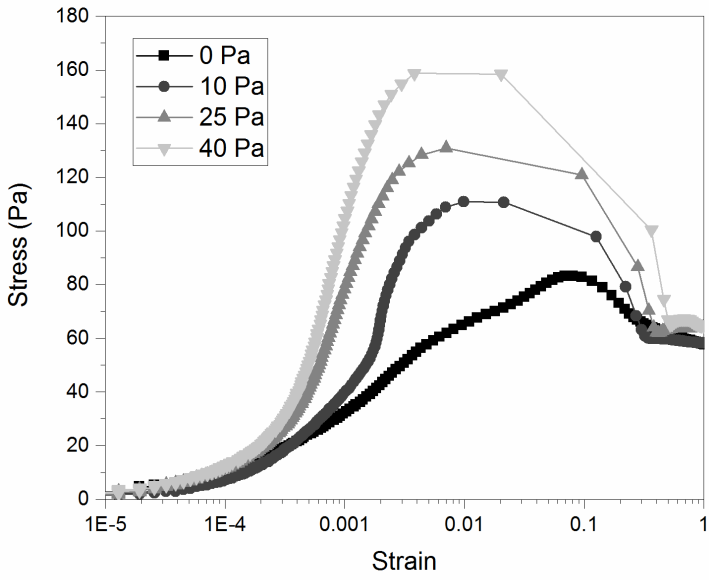

Figure 49. Stress vs. strain in static yield stress test with different shear stress applied during rest.

4.4.3. EFFECT OF VMAS

Here we compare the effect of clay and diutan gum on apparent viscosity, static yield stress and storage modulus evolution at various addition levels. We then discuss the differing mechanisms underlying the influence each of these VMAs have on these rheological parameters.

Figure 50 compares the apparent viscosity evolution of cement pastes modified with nanoclay and diutan gum against plain cement paste during pre-shear. It is apparent that unlike the control paste and paste with diutan gum, the paste modified with nanoclay shows two equilibrium states. The apparent viscosity reaches its first equilibrium state around 60 s, as shown in the inset of Figure 46. Then, the structure breaks down further and viscosity decays to its second equilibrium value around 600 s. The effect of nanoclay on thixotropic behavior at the first equilibrium state has been investigated in other studies [24,29,93,120], where the viscosity of the paste modified with nanoclay is higher than that of plain cement. However, as shear continues, the viscosity decays further and reaches the second equilibrium value, which approaches that of plain cement. The nanoclay carries a negative charge on the faces and a positive charge on the ends [88]. Nanoclay tends to associate with each other by electrical attraction between positively charged edges and negatively charged surfaces, or absorbed on oppositely charged surfaces of cement particles (i.e. C3S is positively charged in cement suspension [89]). This resultant structure leads to a higher initial viscosity, while under strong pre-shearing the viscosity decreases as the structure breaks down. As the nanoclay particles progressively separate and align in the direction of flow [121], the electrical repulsion between the negatively charged surfaces keeps them separate and thus further enhances shear thinning behavior. The second equilibrium state will be the focus of the study in this section to allow for comparison of structural build-up characteristics between mixes from the same initial apparent viscosity.

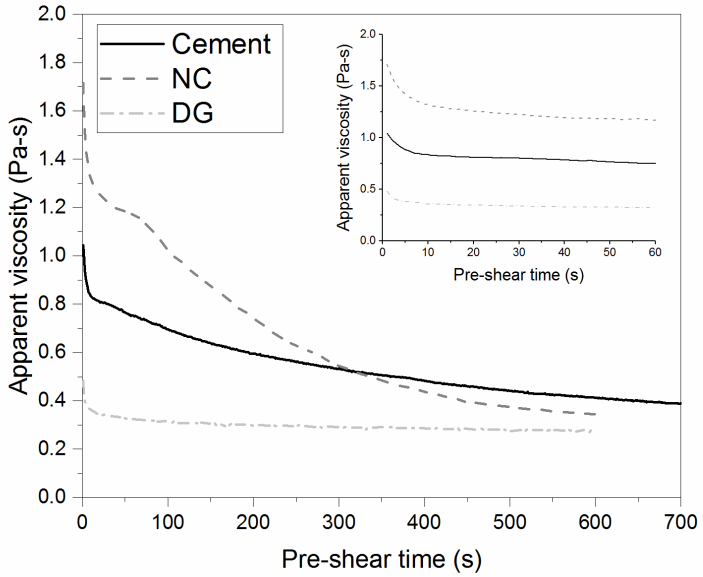

Figure 50. Apparent viscosity evolution of cement pastes with VMAs.

Figure 51 compares equilibrium apparent viscosity of pre-shear and static yield stress right after pre-shear between cement pastes modified with nanoclay and diutan gum. It is shown in Figure 51 (a) that with an increase in addition of nanoclay, apparent viscosity remains relatively constant while static yield stress increases. These results (Figure 50 and Figure 51) indicate that the addition of clays can lead to high shear thinning behavior and rapid structural rebuilding, making it an ideal thixotropy modifier. Further, the increase in structural rebuilding, i.e. static yield stress, can be controlled by addition level.

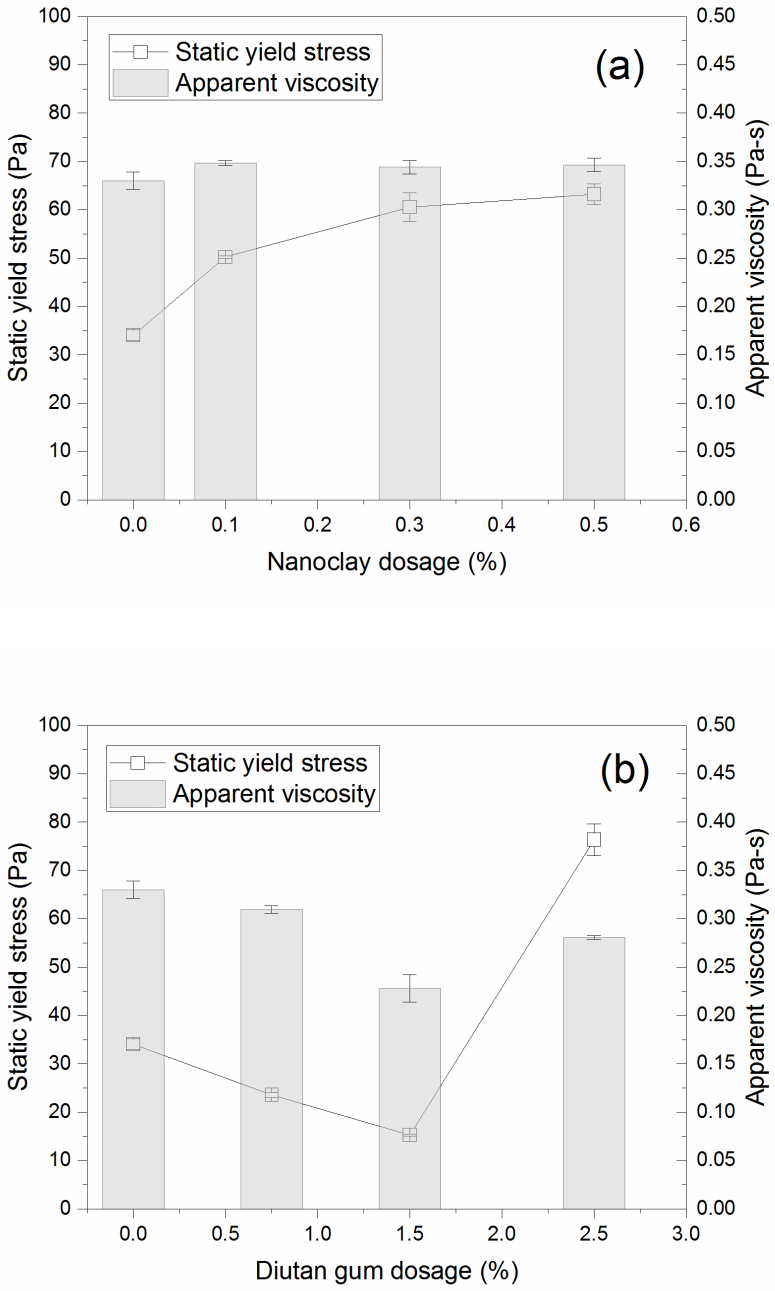

Figure 51. Apparent viscosity and yield stress as a function of nanoclay (a) and diutan gum (b) dosages.

In contrast to nanoclay, diutan gum shows quite a different trend. As shown in Figure 51 (b), below a critical concentration the static yield stress and apparent viscosity of the paste decreases with increasing dosage of

diutan gum. This behavior may be attributed to the alignment of molecules under high shear rate. Above a critical concentration, the cement system exhibits an increase in static yield stress and viscosity. This feature is also observed in polysaccharide solutions [97,122]. The existence of the critical concentration is likely due to the overlapping of polymer coils. Above this concentration, the polymer coils start to interpenetrate and entangle to form a new network of attractive interactions and, thus, the viscosity of the pore solution increases. This effectively increases the static yield stress and viscosity of the cement paste. This hypothesis will be examined in the following analysis.

Figure 52 and Table 7 report the static yield stress over time exhibited by each of the paste systems. It is apparent that the evolution differs significantly between the two VMAs. Compared to the plain paste, both nanoclay and diutan gum lead to an increase in static yield stress. The increase of static yield stress by the nanoclay can be mainly attributed to the initial yield stress (τ_0) jump, as shown in Figure 52, while A_{thix} is only slightly higher, as shown in Table 7. This is in accordance with the literature [100], where nanoclay shows an immediate effect on thixotropy and a relatively moderate growth over time. On the other hand, diutan gum results in a much more pronounced increase in A_{thix}. This remarkable time-dependent enhancing effect on structural build-up may be linked to the nature of interactions between particles in pastes containing diutan gum, which will be further discussed below.

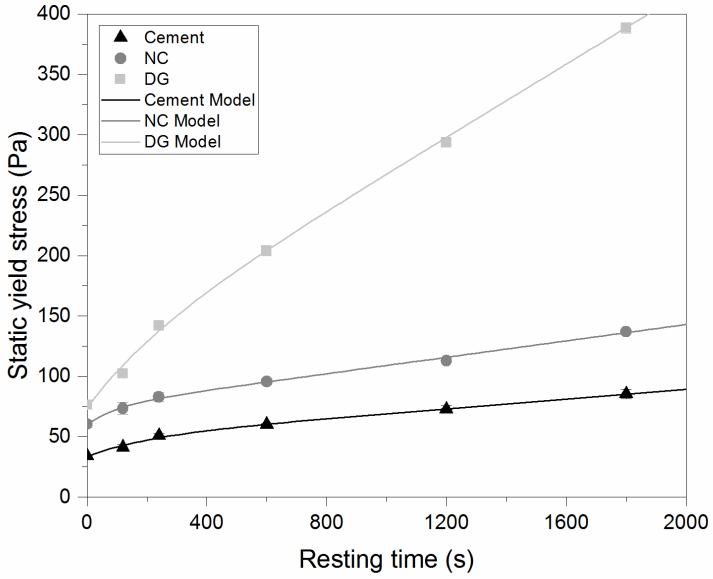

Figure 52. Evolution of static yield stress with different VMAs.

Mix	Pre-shear conditions	τ0 (Pa)	Relaxation time θ (t)	c (Pa)	Athix (Pa/s)
Cement	260 1/s-1500 s	33.34	204.92	15.86	0.020
NC	260 1/s-600 s	60.22	106.04	14.79	0.034
DG	260 1/s-600 s	73.98	238.10	42.12	0.151

Table 7. Thixotropic parameters of static yield stress tests with VMAs.

To better understand the interactions underlying structural build-up, we will look at shear stress evolution under shear, storage modulus and hydration kinetics presented in Figure 53, Figure 54, and Figure 55, respectively. Figure 53 shows the shear stress evolution of the pastes when subjected to an intermediate strain rate of 0.1 1/s at resting time 240 s. Firstly discussing diutan gum, it is shown that the stress within LVED associated with the breakage of the hydrates formed between flocculated cement grains becomes undetectable by the addition of diutan gum. This is in good agreement with the SAOS results, as shown in

Figure 54 (inset), in which G' of paste with diutan gum is smaller than the reference cement paste by two orders of magnitude. This suggests that diutan gum has a negative effect on the contribution of hydrate nucleation between cement particles and subsequently the mechanical behavior of the fresh suspension at low strains. In Figure 55, the heat flow results also show the retarding effect on hydration of diutan gum, namely in extending the dormant period.

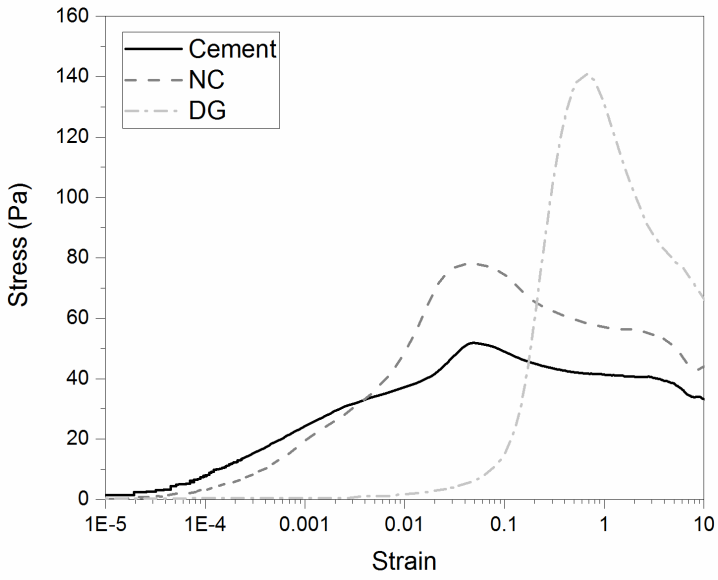

Figure 53. An example of stress vs. strain in static yield stress test for the reference cement paste and a paste containing nanoclay and diutan gum.

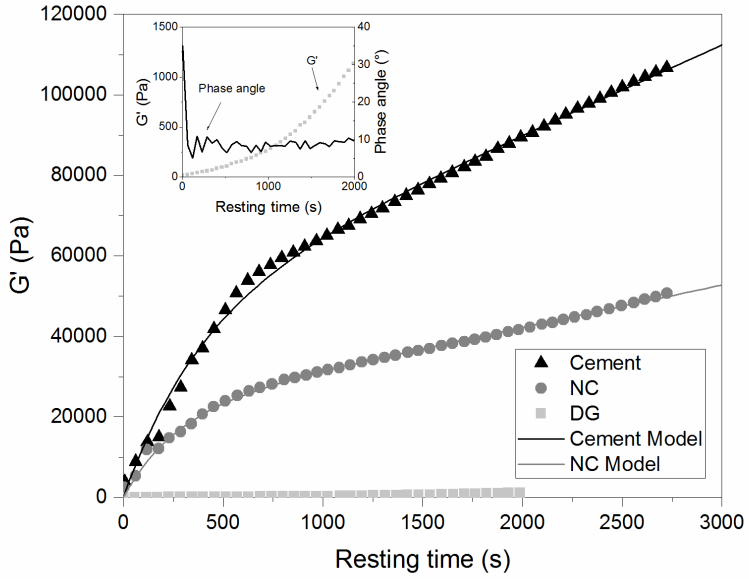

Figure 54. Evolution of storage modulus with different VMAs.

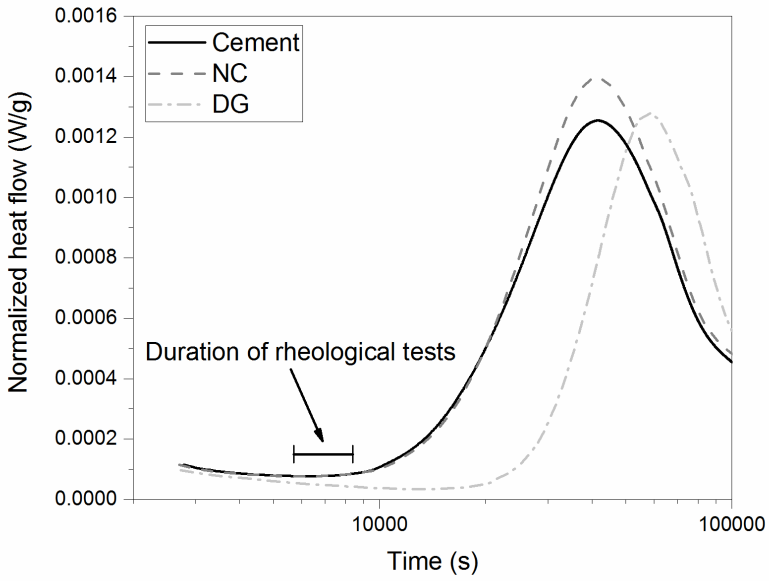

Figure 55. Influence of different VMAs on the heat flow of hydration.

Also note that the weak elastic network exists immediately after pre-shear as phase angle remains at a low level at the beginning of resting, as shown in Figure 54 (inset). In the strain sweep measurements, cement paste with diutan gum showed relatively high critical shear strain. This may indicate the enhanced particle–particle distance by the addition of diutan gum. The nucleation of hydrates is known to occur at pseudo-contact points between cement particles. Increasing the particle distance will slow down the nucleation of hydration by decreasing the number of pseudo-contract points. This supports that diutan gum can hinder nucleation of hydrates and contribute to the decrease in mechanical behavior at low strains. The critical strain of flow onset with diutan gum is approximately 0.7, as shown in Figure 53, which is a surprisingly high value for a mineral suspension. As proposed by [123], this peak is therefore tied to the formation of a new network of attractive interactions in the system able to support both high stresses and high stretching. This new interaction, likely as the result of interpenetration and entanglement of absorbed diutan gum molecules on cement particles, would be the source of rapid build-up of static yield stress, as shown in Figure 52.

The effect of the nanoclay is quite different. As shown in Figure 53, the paste with NC experiences maximum shear stress at a strain of approx. 0.05, which is comparable to that of the control paste. And at smaller strain of the order of a few 10^{-4}, within the LVED, the paste with NC has lower stress throughout. This is consistent with the storage modulus results, as shown in Figure 54, where the paste with NC exhibits lower G' than the control paste. Table 8 presents the model parameters for storage modulus evolution. The addition of nanoclay decreases relaxation time compared to the control paste, indicating that the nanoclay accelerates the percolation process. On the other hand, it decreases the storage modulus of the percolated structure and decelerates the rate of rigidification, as indicated by a lower c value and a lower G_{rigid} value, respectively. In work by Conte and Chaouche, it has been shown that the nanoclay increases storage modulus [11]. And in previous work, it has been shown that paste with NC exhibits higher storage modulus initially but then it falls below the control cement paste over time [10]. The lower G' value measured in the present study may be attributed to the relatively longer pre-shear period compared to the other studies,

which led to significant shear thinning due to deflocculation and/or breaking of C-S-H bridges. The relatively long shearing time was to ensure that we fulfill the assumption of the thixotropic model for the SAOS test, i.e. G_{rigid} and $\lambda_{CSH\_residual}$ are zero. Given that the mechanism of the nanoclays on the fresh state microstructure is not clear, their effect on storage modulus is also unclear and needs further investigation. However, it is shown in Table 8 that the linear evolution index L is the same with and without nanoclay. As this process is controlled by hydration rate, this is in good agreement with the results of isothermal calorimetry, where heat flow is almost the same in pastes with and without nanoclay within the time of interest, as shown in Figure 55. Similar effects have been observed in other work [24].

Mix	Pre-shear conditions	Relaxation time θ (t)	c (Pa)	G_{rigid} (Pa/s)	L (1/s)
Cement	260 1/s-1500 s	386.10	45477.02	22.31	0.000491
NC	260 1/s-600 s	266.67	21238.99	10.50	0.000494

Table 8. Thixotropic parameters of SAOS tests with VMAs.

For the practice of increasing the static yield stress evolution rate of cement paste, hydration accelerators can be used to achieve the same goal as VMAs by accelerating C-S-H formation. High temperatures, which strongly accelerate hydration, can also increase the rate of static yield stress evolution [124]. However, in these cases the increase in static yield stress may compromise workability. With VMAs, static yield stress and storage modulus are de-coupled, which means they enhance thixotropy without promoting any irreversible C-S-H bonds.

4.5. CONCLUSIONS

This study used two methods to monitor the structural build-up of cement-based materials, specifically through static yield stress and storage modulus measured through a stress growth protocol and SAOS,

respectively. Structural build-up is studied using a simple thixotropy model that describes the early non-linear behavior. Based on the results of this study, the following conclusions can be made:

1. We proposed a simple thixotropy model that exhibits good fitting with the experiment results of static yield stress and SAOS tests, which supports the assumption of the existence of the two structures (i.e. general floc and C-S-H nucleation) and corresponding kinetics. This model was used to quantify the effect of different pre-shearing times and VMA additions on the build-up of these two structures.
2. A longer pre-shearing time, associated with a more deflocculated structure, led to a lower initial static yield stress and decelerated the kinetics of rebuilding of static yield stress. At the same time, longer pre-shearing time led to higher storage modulus values, indicating a more percolated C-S-H network.
3. The shear stress applied during resting strongly influenced the static yield stress, likely due to jamming, where static yield stress increased with the stress applied during resting. Thus, this is important to consider when characterizing static yield stress evolution for specific applications, e.g. cementing, formwork pressure, and 3D printing.
4. Although both the nanoclay and the diutan gum were found to decrease storage modulus and increase static yield stress, overall, compared to the control paste starting from the same apparent viscosity, they had different effects on structural build-up kinetics. This was attributed to the differing mechanisms between the two VMAs.
5. Although both floc structure and C-S-H structure in cement paste develops over time, their responses to pre-shear condition and addition of VMAs are quite different. It highlights the necessity of using static yield stress test for monitoring the evolution of stress-bearing ability of cementitious materials, not just SAOS.

CHAPTER FIVE

5. EVALUATION OF PHASE EVOLUTION OF CEMENT PASTE

5.1. INTRODUCTION

For the application of oil well cementing, it is necessary to understand the phase evolution of the cement slurry during and after placement under down-hole conditions, as this has implications on the eventual sealing ability of the cement sheath. For deep-water applications, downhole temperatures and depths can reach (and exceed) 350 ºF [180 ºC] and 20000 ft [6000 m], respectively. There is also hydrostatic pressure and pumping pressure being exerted onto the material, which can reach up to 22 ksi [150 MPa]. Therefore it is necessary to perform characterization under elevated pressure and temperature conditions. As this presents a significant experimental challenge, especially in-situ and real-time, information on phase development of oil well cement slurries at such conditions is still lacking. Synchrotron x-ray diffraction (XRD) has been employed in several studies on cement-based systems to characterize the early stages of hydration [125–127], the influence of additives on select phases [128,129], and alternate cements [130–132]. Some studies have investigated oil well cement slurries with different mix designs and additives, including silica, retarding agents, calcium chloride, and white cement, at different temperatures and pressures [133–137]. Further, researchers have demonstrated the coupled effect of pressure and temperature on cement hydration kinetics and phase evolution. Jupe et al. [138] examined phase evolution at 0 ksi – 8.7 ksi [60 MPa], ≤ 176ºF [80ºC]; Pang et al. [139,140] implemented isotherma calorimetry analysis to study hydration kinetics under pressure ≤ 7.5 ksi [51.7 MPa] and temperature ≤ 140ºF [60ºC].

Numerous studies have demonstrated the potential of nanomaterials to enhance various properties of cement-based systems, including mechanical, rheological, and durability, as summarized in this review

paper [141]. As understanding of the effects and mechanisms of nanomaterials on the performance and microstructural properties of cement-based materials increases, researchers have begun to explore its use in specialized applications. These applications include nanosilica for impermeable coating [142], titanium dioxide nanoparticles for self-cleaning [143], Carbon nanotubes for self-sensing [144–146], and nanoclays as rheological modifiers [24,28,120]. It is possible to utilize nanomaterials for oil well cementing applications in order to tailor the flow and setting properties during the cementing process and reduce permeability to enhance sealing ability. In order to explore the suitability of nanomaterials in oil well cements, information on their impact on the phase evolution at elevated temperatures and pressures is needed. It is well accepted that nanomaterials have seeding effects that accelerate and promote the hydration of cement [147–149]. How this seeding effect influences the phase evolution at elevated pressure and temperature conditions has not been investigated thus far and was the focus of the present study.

In the present study, a deformation-DIA (D-DIA) apparatus was utilized that allowed XRD to be performed at temperatures up to 300ºF [149ºC] and pressures reaching up to approximately 15 ksi [100 MPa], for structural characterization. Fresh cement slurry was placed in the D-DIA with a synchrotron XRD setup and scanned every few minutes, thereby allowing real-time, in-situ measurements up to and shortly beyond setting. From the XRD patterns, the formation and decomposition of select crystalline phases were tracked over time, namely alite (C_3S), tetracalcium alumino ferrite (C_4AF), portlandite (CH), ettringite, monosulfate, and jaffeite. The influence of temperature and addition of nanomaterial on the evolution of various phases was investigated. Nano-sized attapulgite clay was investigated in this study considering the potential benefits it can introduce to the cementing process as a rheological modifier.

5.2. RESEARCH SIGNIFICANCE

Information on the phase evolution of oil well cement systems at elevated pressures and temperatures is still lacking due to experimental challenges in characterization. But this information is critical to improve the cementing process in terms of efficiency and safety during these operations. Also, to explore the potential use of nanomaterials to enhance cementing performance, characterization on the effect of seeding on the microstructural properties of the setting oil well cement slurry is needed. This study implements a synchrotron-based D-DIA setup that can capture the changes in the phase evolution at early age (shortly after mixing) due to elevated pressures and temperatures that simulate downhole conditions, as well as nanomaterial addition.

5.3. EXPERIMENTAL PROCEDURE

5.3.3. MATERIALS

Class A oil well cement (OWC) and tap water were used in all mixes. Class A OWC is considered ordinary grade, where the chemical composition is comparable to that of American Society for Testing and Materials (ASTM) Type I Portland cement [4]. The Blaine Fineness is 314 m^2/kg as measured through ASTM Standard Method C 204. And its chemical composition is presented in Table 9.

SiO_2,%	20.1
Al_2O_3,%	4.5
Fe_2O_3,%	4.9
SO_3,%	2.3
CaO,%	63
MgO,%	2.5
Na_2O,%	/

K_2O ,%	/
Loss of Ignition ,%	0.51
Total	97.3
C_3S,%	60
C_2A,%	4
$C_4AF + 2C_3A$,%	22

Table 9. Chemical composition of Class A oil well cement

Highly-purified attapulgite clays were added to select mixes at 0.5% by mass of cement. They are commercially available clays that are chemically exfoliated from bulk attapulgite to remove all impurities [19]. When dispersed, they are needle-like with an average length of 69.0 µin [1.75 µm] and diameter of .118 µin [3 nm]. Therefore it can be considered a nanomaterial and will be referred to as "nanoclay" herein. In separate studies, these clays have been demonstrated to greatly enhance the level of thixotropy of cements and concretes for specialized applications [23,26,150]. Thixotropic slurries that exhibit high flowability during pumping but then rapidly gel at rest can be beneficial for oil well cementing applications. Such properties would enable the material to effectively resist gas penetration from the adjacent formations during the cementing process. This period between the placement and setting of the cement sheath, known as transition time, is considered to be one of the states when the well is most vulnerable to gas migration [2]. Although primarily used as a rheological modifier, it is necessary to investigate the effect of the clays on other performance properties at the addition levels of interest. Previous studies have investigated compressive strength [151] and shrinkage [152]. In the present study, the focus is on phase evolution under elevated temperature and pressure.

Cement pastes were prepared by hand-stirring for 3 minutes in a 25 mL [25 cm^3] beaker with a metal spatula. When nanoclay was added, it was first blended with the mixing water in a Waring blender for 2 minutes then added as a suspension to the cement.

5.3.4. HIGH-PRESSURE, HIGH-TEMPERATURE SYNCHROTRON XRD SETUP

Monochromatic synchrotron XRD tests were performed at the Advanced Photon Source (APS) in Argonne National Laboratory (ANL) on bending magnet beamline 13-BM-D (GeoSoilEnvironCARS) in a deformation-DIA (D-DIA) apparatus. The D-DIA allowed for elevated pressures and temperatures to be applied to the sample during testing. A brief description of the experimental setup will be given here but the details can be found elsewhere [153,154].

The fresh slurry was loaded into the D-DIA within a cubic assembly, the schematic of which is shown in Figure 56. After mixing, the slurry was cast in a 0.12 in x 0.12 in [3 mm x 3 mm] PEEK cylindrical capsule. The capsule was vertically centered in the cubic assembly with PEEK plugs placed above and below. A layer of sodium chloride was added within to serve as a pressure marker. A graphite heater surrounded the capsule and plugs, through which electrical resistive heating was applied. In all test runs pressure was applied first, followed by temperature.

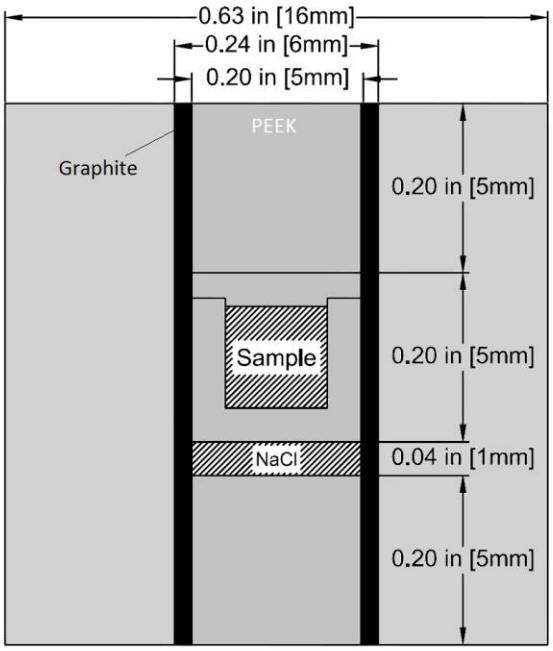

Figure 56. Schematic of the cubic sample cell assembly. Both the cube and the inner plugs are made of PEEK.

Figure 57. Sample loading in the D-DIA. The cube (with thermocouple wires protruding to the right) in the center is the assembly, in which the sample was located. Some of the square-tipped anvils can also be seen.

Pressure was introduced through a hydraulic press. Load was applied by a uniaxial hydraulic ram to the D-DIA, within which six anvils were configured to convert the uniaxial load into three orthogonal directions, thereby applying equal load to each face of the cubic assembly (Figure 57), achieving quasi-hydrostatic pressure. A constant load of 11 tons was maintained for all samples. Calibration was performed using the sodium chloride pressure marker to obtain a measure of the pressure experienced by the slurry sample. For each run, sodium chloride's lattice constant was obtained from its XRD patterns. The pressure was then determined from the lattice parameter of sodium chloride using Brown's equation of state [155]. Pressure can increase with temperature as the sample undergoes thermal expansion, or pressure can decrease with temperature as the material surrounding the sample, i.e. PEEK capsule, softens and relaxes. Therefore pressure marker measurements were taken in the middle and at the end of each run. Average marker readings indicated that the pressure of the sample was within 15 ksi [100 MPa] for all tests, with a standard deviation of 6.3 ksi [43.4 MPa]. Due to this uncertainty, effect of pressure was not the focus of this paper. Development of the experimental setup to improve pressure control is ongoing.

Heat was introduced to the sample by applying an electrical power through the top and bottom anvils. Once sufficient contact was made during loading, current passed through the graphite heater in the assembly and effectively heated the sample. Calibration was performed to obtain a relationship between applied power and temperature of the sample, where the latter was measured through thermocouples. In all subsequent tests, temperature was calculated based on the calibration.

From initial cement and water contact, it took approximately one hour to load the assembly into the D-DIA and reach the targeted temperature and pressure levels. Once these levels were met, continuous XRD scans using a MAR165 charge-couple area detector (approximately once every 200 s) were performed on the sample up to around 8 hours. Due to limitations beamline access and relatively long duration of each test run, one sample per mix and temperature was tested.

5.3.5. ISOTHERMAL CALORIMETRY

Rate of hydration was measured through isothermal calorimetry based on ASTM Standard Method C 1679 - 14. 0.18 oz (5 g) of cement paste, prepared using the same mixing protocol as the synchrotron XRD test, was cast in glass vials and loaded in the calorimeter (TA Instruments TAM Air) set at target temperature. The sample was loaded into the calorimeter at the same age at which heat was introduced to reach the target temperature during the synchrotron XRD tests – approximately 1 h after initial cement and water contact. As the heating rate was relatively fast in the synchrotron XRD test, within 5 min, it was assumed that the temperature history was consistent between the two test setups. Isothermal calorimetry was performed at atmospheric pressure and temperatures of 140 and 185ºF [60 and 85ºC]). At least three specimens were tested per mix and temperature condition, and the average was taken to be the representative value.

5.3.6. DATA ANALYSIS

The wavelength of x-ray used in this work was 0.3097 Å (E = 40.00 keV) and the incident beam was collimated to 0.3 x 0.3 mm. The raw images were converted to intensity versus d-spacing using FIT2D [156]. In selecting diffraction peaks for phase identification, the main criterion was that there was no significant overlap with other peaks. The d-spacing range between approximately 4.8 Å to 11 Å, which include all phases of interest, was chosen. The peaks that were used are presented in Table 10. The area of a single peak from each phase of interest was estimated by curve fitting with a mixture of Gaussian and Lorentzian functions. This integrated intensity (peak area) represents the amount of the phase as detected by the x-ray beam. The rapid time-resolved XRD pattern is presented in Figure 58 to show how the relative amounts of each phase vary during hydration. The high brilliance of the x-ray source at APS allowed for XRD patterns to be collected at a fine time resolution (approximately every 200 s). Also, since the slurry sample was loaded into the setup while in the fresh state, it was effectively cured in the D-DIA. Therefore

it was possible to track the crystalline phases in-situ and in real-time from very early ages to beyond setting. Scans were performed on each sample for approximately 8 hours.

Phase	Selected peak (hkl)	d-spacing (Å)	ICDD card no.
C_3S	201	5.93	42-551
C_4AF	001	≈7.25	30-226
Portlandite	001	4.9	4-733
Ettringite	100 or 110	9.72 or 5.61	41-1451
Monosulfate	006	4.78	42-62
Jaffeite	100	8.69	77-0960
Katoite	211	5.05	77-1713

Table 10. Diffraction Peaks Used in the Data Analysis

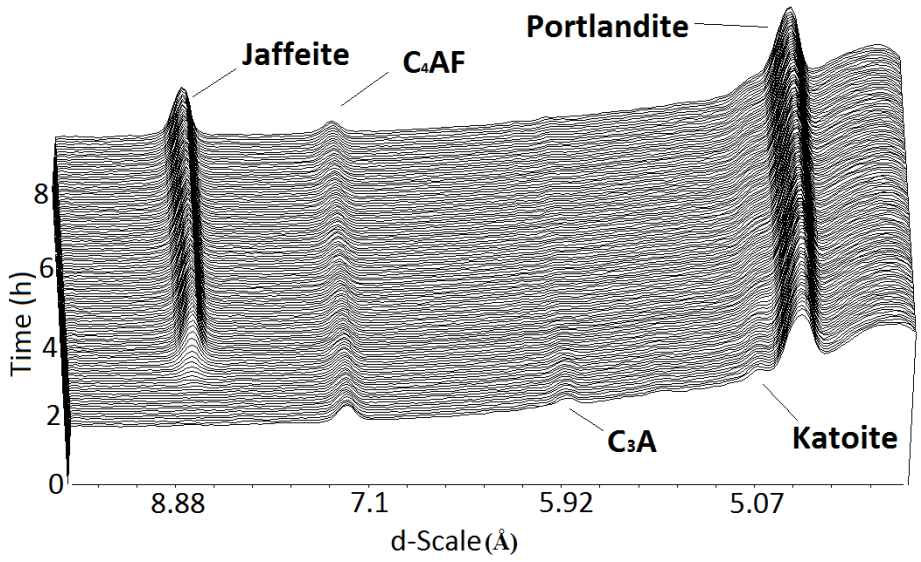

Figure 58. XRD patterns collected over 8 hours.

5.4. EXPERIMENTAL RESULTS AND DISCUSSION

5.4.1. EFFECT OF TEMPERATURE

XRD patterns of the samples were collected at temperatures of 140, 185, and 300ºF [60, 85, and 149ºC]. The effect of temperature on the presence of various phases in plain OWC pastes will be discussed here. All plots, including calorimetry results, were zeroed to the time shortly after the target temperature was met, approximately 1 hour after initial cement-water contact for all mixes. It is assumed that any changes in hydration may be considered negligible prior to this point. Generally, the XRD results capture the consumption of C_3S, ferrite, and gypsum, the conversion from ettringite to monosulfate, and the formation of portlandite and jaffeite.

Figure 59 shows the evolution of phases C_3S, ferrite, and gypsum at 140ºF [60ºC], each of which decrease over time due to the progression of hydration. The curves for these phases were very similar at 185ºF [85ºC] and so are not presented here. The decrease in gypsum was detectable from the beginning and a slight plateau was observed, in agreement with other studies [136,157], around 60 min. This deceleration is attributed to a layer on the surface of unhydrated cement grains that initially prevents the ingress of dissolved sulfates. The plateau was then followed by a rapid decrease until gypsum was completely consumed by 125 min. Although no significant differences in C_3S, ferrite, and gypsum were observed as

an effect of increasing the temperature from 140ºF [60ºC] to 185ºF [85ºC], there was an apparent change in phases ettringite and monosulfate.

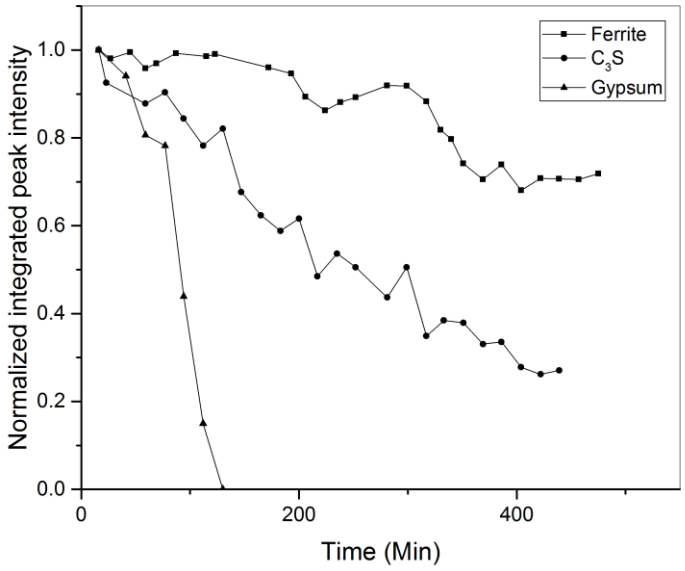

Figure 59. Evolution of C3S, ferrite, gypsum in plain OWC at 140ºF [60ºC].

The evolution of ettringite, monosulfate, and portlandite at 140ºF [60ºC] and 185ºF [85ºC] are presented in Figure 60 and Figure 61, respectively. Synchrotron XRD tests were supplemented with isothermal calorimetry tests, where the heat of hydration curves are superimposed with the XRD results, and will be discussed later. As shown in Figure 60, at 140ºF [60ºC] the decline of ettringite occurred simultaneously with the formation of monosulfate over time, up to 450 min, which marks the transformation of phase ettringite to phase monosulfate. This conversion did not begin immediately after gypsum was exhausted, in agreement with the observations of Jupe et al. [137]. This indicates that after the disappearance of solid gypsum, there was still SO_4^{2-} left in the sample. Monosulfate then remained stable until the end of the experiment. In comparison, at 185ºF [85ºC] (Figure 61), ettringite-monosulfate conversion occurred much more sharply, between 150 and 200 min, whereas at 140ºF [60ºC] it occurred over a period of approximately

300 min. The kinetics of ettringite decomposition and monosulfate formation are highly dependent on temperature and pressure [158]. Then, the intensity of monosulfate decreased, which is associated with the destabilization of monosulfate at 185ºF [85ºC].

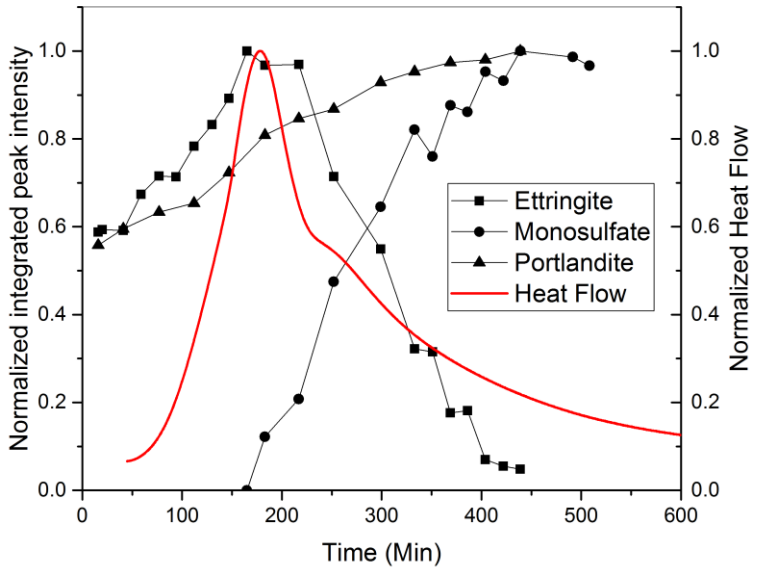

Figure 60. Evolution of ettringite, monosulfate, and portlandite in plain OWC at 140ºF [60ºC], superimposed with heat of hydration curve.

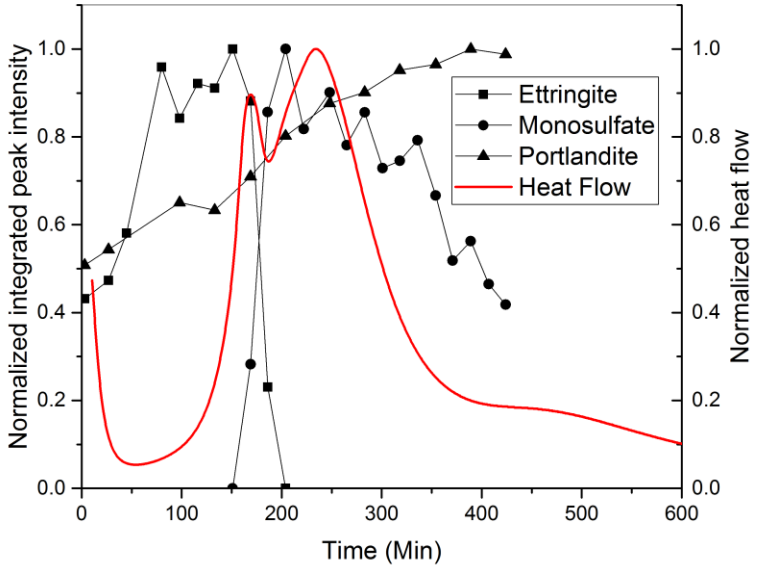

Figure 61. Evolution of ettringite, monosulfate, and portlandite in plain OWC at 185ºF [85ºC], superimposed with heat of hydration curve.

The occurrence of this conversion between ettringite to monosulfate is detectable through isothermal calorimetry, as well. Heat of hydration curves can exhibit two peaks. The first peak indicates silicate reaction, where the main products are C-S-H and CH. The second peak indicates aluminate reaction, namely conversion from ettringite to monosulfate. Therefore, the rate of conversion detected by XRD can be correlated to the second peak observed by calorimetry. At 185ºF [85ºC], shown in Figure 61, the second peak is very prominent and occurs at approximately the same time as the ettringite-monosulfate transformation measured by XRD. On the other hand, at 140ºF [60ºC], shown in Figure 60, there is no apparent second peak. Instead, there is a decrease in rate of deceleration, or a shoulder, that follows the first peak. This agrees with the XRD results, as the transformation from ettringite to monosulfate was found to occur much more gradually than it does at 185ºF [85ºC]. It should be noted that the difference in the duration and occurrence of the conversion may be attributed to the difference in pressures and heating rates between

the two test setups. Still, correlations were observable and the agreement between the XRD results and calorimetry results was good.

At 300ºF [149ºC], ettringite and monosulfate were not detectable. This is because their formation and decomposition occurred very rapidly during the heating period, as shown in Figure 62. There was also the appearance of phase katoite, which has been reported to result from the decomposition of monosulfate [159]. The integrated peak intensities of jaffeite, ferrite, portlandite, and C_3S at 300ºF [149ºC] are presented in Figure 63. The accelerating effect of temperature on alite consumption was much greater at 300ºF [149ºC] than at 140 and 185ºF [60 and 85ºC]. Also, a marked difference from the other two temperature conditions was the presence of jaffeite. The dramatic decline of alite occurred simultaneously with the formation of jaffeite, which continued steadily over time. Jaffeite is a crystalline form of calcium silicate hydrate (C-S-H), which has lower mechanical strength and higher permeability than amorphous C-S-H, and its formation is generally considered to be unfavorable [160]. However, it is possible to mitigate with silica addition [133].

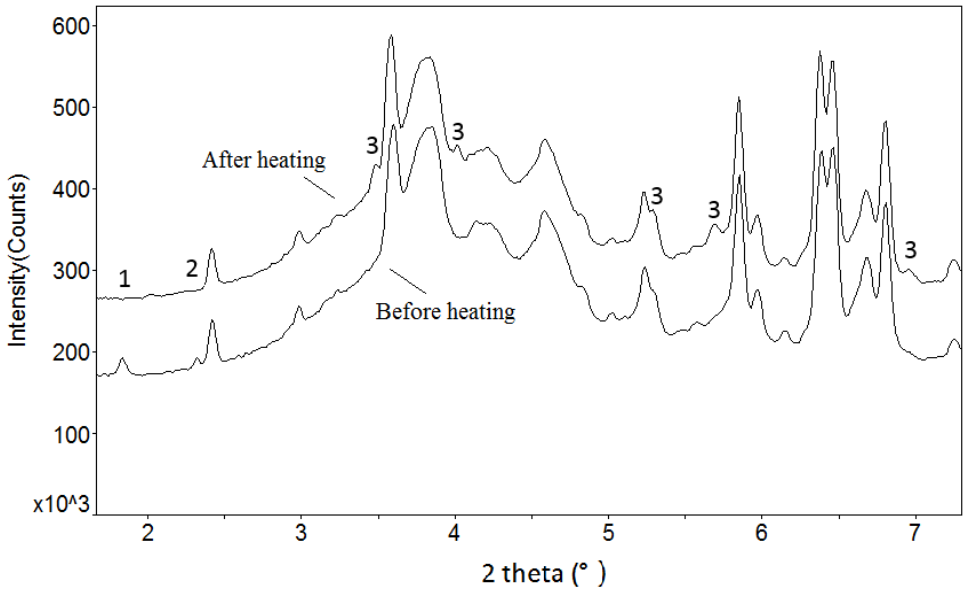

Figure 62. XRD patterns of plain OWC before and after heating to 300ºF [149ºC]. 1. Ettringite, 2. Gypsum, 3. Katoite.

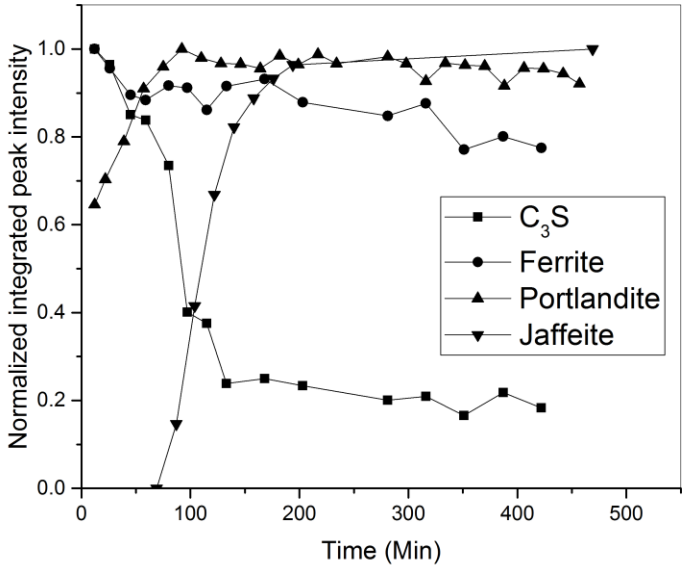

Figure 63. Evolution of jaffeite, ferrite, portlandite, and C3S in plain OWC at 300ºF [149ºC].

5.4.2. EFFECT OF NANO-ADDITION

OWC slurries with 0.5% addition of nanoclay by mass of cement were tested at temperatures of 140 and 300ºF [60 and 149ºC]. At 140ºF [60ºC], no measurable effect by the nanoclay was observed. This may have been due to the poorly defined peaks in the XRD patterns for the phases of interest, which made it difficult to observe any subtle differences. Figure 64 shows the heat of hydration curves of the cement pastes with and without clay at this temperature. The age and time of loading of the paste samples were kept consistent – loaded 15 min after mixing – to capture the effect of the clays. Comparing the two curves, slight differences can be observed – the first peak and subsequent shoulder are higher and occur sooner for the paste with clay than the control by approximately 15 min. The synchrotron XRD results

showed that the ettringite-monosulfate conversion occurred at the same rate. The acceleration in rate of hydration in the paste with clay this is captured through isothermal calorimetry would not have been detectable in the XRD results. However, it does provide evidence that the clays are introducing a seeding effect, although more investigation is needed to confirm.

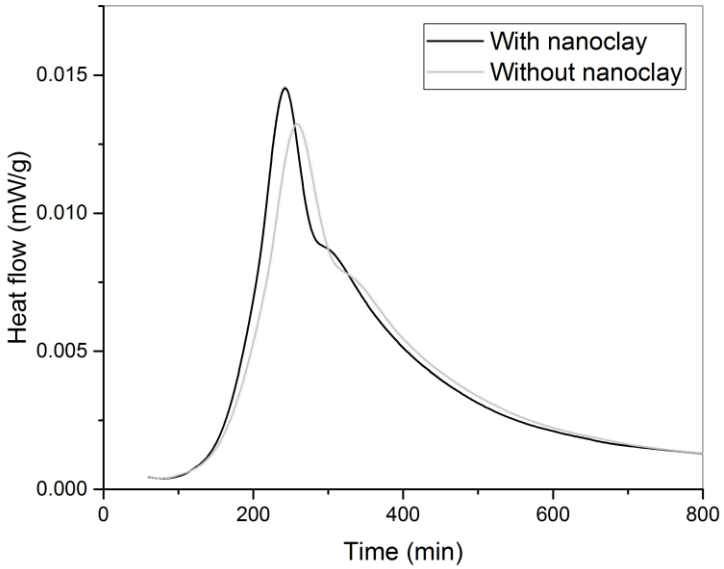

Figure 64. Heat of hydration curves at 140ºF [60ºC] in OWC with 0 and 0.5% nanoclay addition.

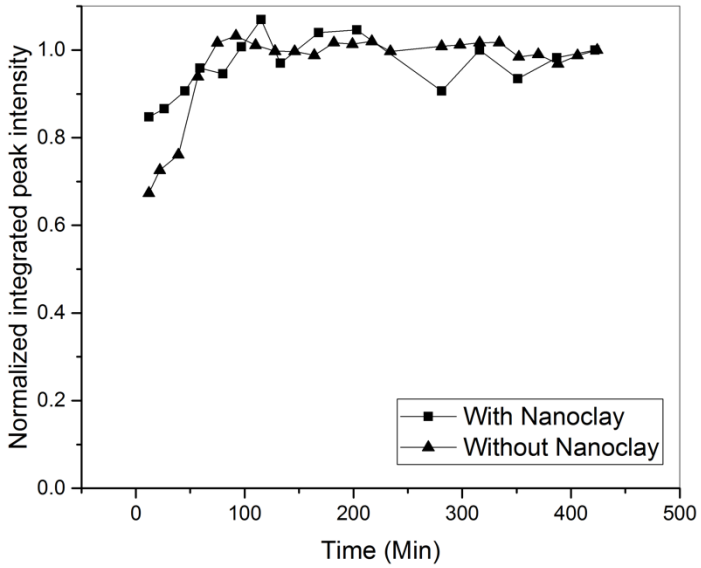

Figure 65. Formation of portlandite at 300ºF [149ºC] in OWC with 0 and 0.5% nanoclay addition.

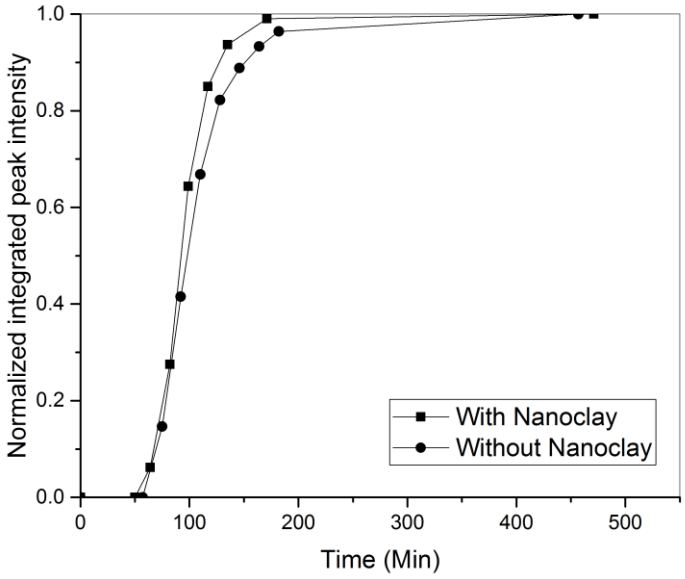

Figure 66. Formation of jaffeite at 300ºF [149ºC] in OWC with 0 and 0.5% nanoclay addition.

Jaffeite, which formed at 300ºF [149ºC], had a very well defined peak and the relative amounts were readily computed. The integrated peak intensities of portlandite and jaffeite at 300ºF [149ºC] are shown in Figure 65 and Figure 66, respectively, comparing slurries with and without nanoclay. As shown in Figure 65, the nanoclay led to a higher rate of portlandite formation very early on, indicating that it had an accelerating effect on hydration. Similarly, the XRD results presented in Figure 66 show that the nanoclay accelerated the formation of jaffeite. This may potentially be attributed to a seeding effect. As aforementioned, the formation of jaffeite is not desirable and the addition of silica may mitigate its formation - these ternary systems will be the topic of future work.

5.5. FURTHER RESEARCH

A limitation of the setup used in this study was the uncertainty in the pressure exerted on the slurry sample. Continued developmental work on the setup is planned to improve pressure control. Also, slurries incorporating silica, other classes of OWC, and other types of nanomaterials would be of interest, to see if the formation of jaffeite that is caused by the nanomaterial addition can be mitigated to improve mechanical properties.

5.6. CONCLUSIONS

This study investigated the influence of temperature and addition of nano-sized attapulgite clay on the phase evolution of Class A OWC slurries. From the synchrotron XRD and isothermal calorimetry tests, the following conclusions can be drawn:

The synchrotron XRD test setup effectively captures the consumption of C_3S, ferrite, and gypsum, the conversion from ettringite to monosulfate, and the formation of portlandite and jaffeite of fresh cement

slurries. Increasing temperature from 140ºF [60ºC] to 300ºF [149ºC] leads to acceleration in portlandite formation and ettringite-monosulfate conversion. At 300ºF [149ºC] the formation of jaffeite occurs.
The ettringite-monosulfate conversion at 140 [60ºC] and 300ºF [149ºC] in the XRD results agreed well with the appearance of the second peak in heat of hydration curves measured by isothermal calorimetry. Discrepancies between the results can be attributed to the difference in pressure and heating rate between the two test setups.

The nanoclays lead to measurable acceleration in jaffeite and portlandite formation at 300ºF [149ºC]. This can potentially be due to a seeding effect, which is commonly observed when incorporating nanomaterials into cementitious systems. As jaffeite is undesirable, leading to increase in permeability, this is an important mix design consideration when incorporating attapulgite clays or other nanomaterials for oil well cementing applications. Incorporating silica to mitigate jaffeite formation and promote amorphous C-S-H growth in systems modified with nanomaterials warrants investigation.

CHAPTER SIX

6. EVALUATION OF HARDENED PROPERTIES OF BLENDED CEMENT MORTARS

6.1. INTRODUCTION

The heterogeneity of concrete exists at all length scales, from the macro- to nanoscale. Nanomaterials can be used to modify the structure at the nanoscale to enhance the performance of cementitious materials at the macroscale. Given their significantly high specific surface area, nanomaterials exhibit remarkable changes in surface energy, surface morphology, chemical reactivity and mechanical properties. The novel properties of nanomaterials have roused considerable interest in nanomodification of cementitious materials in both the fresh and hardened states [141].

Nano-sized highly purified palygorskite clays, which are commonly used as a rheological modifier, can significantly increase the yield stress and shape stability of fresh state cementitious materials [24,25,90], which has been found to effectively reduce formwork pressure [23]. Studies have found that palygorskite clays improve the flocculation strength and floc size, which can explain the increase in yield stress [27,28]. And many other early-age properties have been investigated, including flowability [26], thixotropy [100] and chemical phase change [94]. However, the data on hardened properties are scarce, especially in the presence of dispersants.

Carbon nanotubes (CNTs) exhibit significantly enhanced mechanical properties, i.e. Young's modulus on the order of TPa and tensile strength on the order of GPa, as well as unique electrical and chemical

properties [141]. To leverage these properties, numerous studies have demonstrated the ability of CNTs to act as nano-reinforcement and enhance the mechanical properties of cement composites when effectively dispersed in the matrix [161–164]. However, very few studies exist in the literature regarding the effect of CNTs on the fresh state properties, especially in cementitious materials containing supplementary cementitious materials (SCMs).

Due to the complexity of SCMs with respect to chemical composition and physical properties, including specific gravity, particle size distribution and specific surface area, the results of SCMs on the rheology of fresh cement-based materials are inconsistent [165–173]. For example, Some studies [172,174] reported an increase in viscosity with fly ash while others show it leads to a decrease [165,168]. Given the prevalence of SCMs, there is a need to investigate the effect of these novel additives on blended systems.

This performance-based study aims to examine the effect of palygorskite clays and CNTs on the rheological and hardened properties of two different systems – a unitary cement mortar and a ternary mortar prepared with cement, fly ash and blast furnace slag. Moreover, the combined effect of palygorskite clays and CNTs was also studied to explore the potential of enhancing the various performance properties of cementitious materials through the addition of nanomaterials with different desired functions.

6.2. MATERIALS

Type I Portland Cement was used in all mixes. Type F fly ash and Grade 120 Blast furnace slag were used as SCMs to partially replace the cement. The chemical compositions are shown in Table 11. The particle size distribution of the binders is shown in Figure 67.The total specific surface area (SSA) of cement, FA and slag were 775, 794 and 1213 m^2/kg, respectively. D10, D50 and D90 are the particle size value where

10%, 50% and 90% of the particles are finer. They are 3.72, 18.82, and 45.17 μm for cement; 3.62, 20.60, and 111.18 μm for fly ash; and 2.41, 10.75, and 25.11 μm for slag. It could be seen that slag is finer than cement in both higher SSA and lower D10, D50 and D90 values. Fly ash has similar SSA and D10 as cement; however larger D90, indicating that fly ash has some large size particles.

Chemical Oxide	Type I Cement (%)	Type F Fly Ash (%)
SiO_2	19.2	47.2
Al_2O_3	5.0	23.4
Fe_2O_3	3.4	16.6
CaO	62.4	4
MgO	3.9	-
SO_3	2.7	1.3
Free Lime	1.0	-
Loss on ignition	2.6	2.1
CO_2	1.9	-

Table 11. Chemical composition of Type I Portland Cement and Type F Fly Ash.

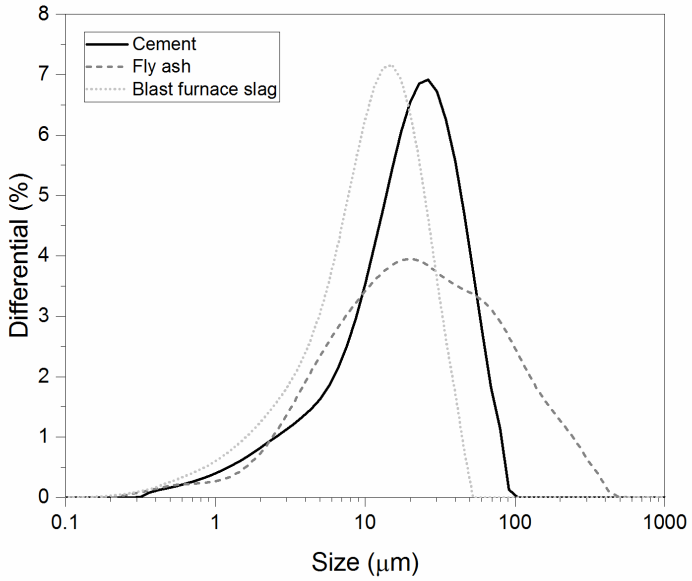

Figure 67. Particle size distributions of the cement, fly ash and blast furnace slag.

The effect of fly ash and blast furnace slag on 28 day compressive strength was evaluated in preliminary tests. The results of blended mortars with binders composed of 50% cement and different dosages of fly ash and/or blast furnace slag are shown in Figure 68. The control mix with 100% cement content is represented by the horizontal dotted line. As expected, fly ash reduced strength due to delayed pozzolanic reaction and dilution, while slag enhanced strength due to increased reactivity [175]. The grade of blast furnace slags were determined by their slag activity index, SP/P×100%, where P is compressive strength of portland-cement mortar cubes and SP is the compressive strength of mortar cubes made with the same mass of a blend that is 50 % slag cement and 50 % portland cement by mass [176]. The slag activity index of the slag in this study is 115 which can be classified as Grade 120 according to ASTM C989 [176]. To compare the effect of the nanomaterials on the two systems, cement versus blended, the strength of the base mix was fixed between the two. Figure 68 shows that the mix with 25% fly ash and 25% blast furnace slag replacement exhibited 28 day strength that was comparable to that of the 100% cement mortar, thus was selected for this study.

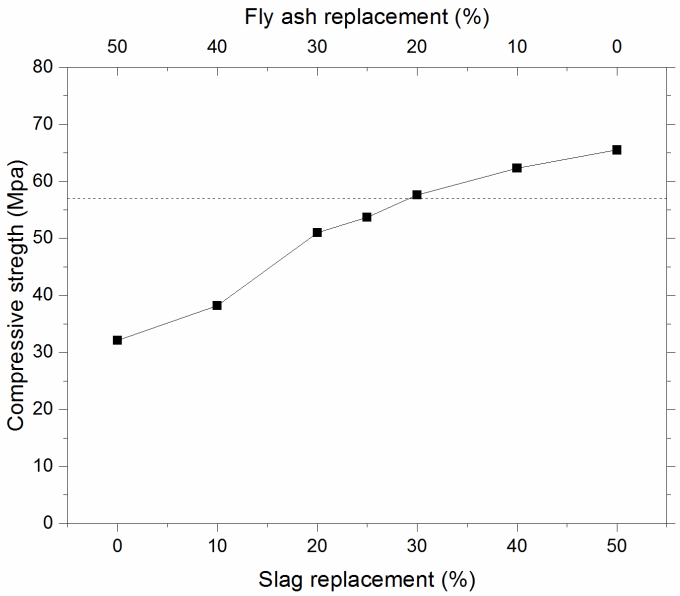

Figure 68. 28 day compressive strength results of blended mortars with binders composed of 50% cement and different dosages of fly ash and/or slag. Dashed line represents 100% cement mortar.

A commercially available, multiwalled carbon nanotube with a carbon purity of 90% was selected in order to explore materials that would be more cost-effective and suitable for large-scale application. The average diameter is 9.5 nm and the average length is 1.5 μm. The dosage of 0.01% CNTs by mass of cement was used in this study based on the results of previous work by other researchers [162,177,178]. To disperse the CNTs (dry, as received) they were combined in mixing water with a polycarboxylate-based superplasticizer at a dispersant-to-CNT mass ratio of 5, based on the results of a separate study [161]. The mixture was ultrasonicated in a high intensity ultrasonic processor for 1 hour at 40% amplitude. The power of the processor is 500 Watts. To avoid overheating and evaporation of water during ultrasonication, the metal beaker containing the mixture was partially immersed in an ice bath.

The clay was a highly purified form of palygorskite, or attapulgite. It has a specific gravity of 2.29 and is needle-like in structure (average length = 1.75 μm, average diameter = 30 nm). Based on previous work [23,93], 0.3% of palygorskite clays by mass of cement was used. To disperse the clays, they were blended in water in a Waring blender for 2 min to produce a stable suspension.

Mixes	Cement (C)	Fly ash (F)	Slag (S)	Surfactant	Carbon nanotubes (CNT)	Palygorskite clays (PAL)
100C_0	100	0	0	0.05	0	0
100C_0.01CNT	100	0	0	0.05	0.01	0
100C_0.3PAL	100	0	0	0.05	0	0.3
100C_0.01CNT_0.3PAL	100	0	0	0.05	0.01	0.3
50C25F25S_0	50	25	25	0.05	0	0
50C25F25S_0.01CNT	50	25	25	0.05	0.01	0
50C25F25S_0.3PAL	50	25	25	0.05	0	0.3
50C25F25S_0.01CNT_0.3PAL	50	25	25	0.05	0.01	0.3

Table 12. Mix proportions of all the samples (wt.% of binder).

The mix designs are presented in Table 12. All mortars had a water-to-binder (w/b) = 0.5 and sand-to-binder (s/b) = 2 for rheological, electrical and compressive measurements. All pastes had a w/b ratio = 0.43 for tensile tests. The mixing protocols are summarized in Table 13.

Table 13. Mixing protocols.

Mixing methods	Mixing procedures			
	0	0.01CNT	0.3PAL	0.01CNT_0.3PAL
Rheological properties measurements / Mixing by hand	Mix sand and binder materials (i.e. cement, fly ash and slag) for 1min			
	Add aqueous surfactant solution containing all mixing water, mix for 6 min	Add aqueous surfactant-CNTs solution containing half of mixing water, mix for 3 min	Add aqueous surfactant solution containing half of mixing water, mix for 3 min	Add aqueous surfactant-CNTs solution containing half of mixing water, mix for 3 min
		Add the remaining water, mix for 3 min	Add palygorskite clays suspension with the remaining mixing water, mix for 3 min	Add palygorskite clays suspension with the remaining mixing water, mix for 3 min
Hardened properties measurements / Mixing by a Hobart mixer	Mix sand and binder materials (i.e. cement, fly ash and slag) at low speed of 139 rpm for 1 min			
	Add aqueous surfactant solution containing all mixing water, mix for 2 min at low speed	Add aqueous surfactant-CNTs solution containing half of mixing water, mix for 1 min at low speed	Add aqueous surfactant solution containing half of mixing water, mix for 1 min at low speed	Add aqueous surfactant-CNTs solution containing half of mixing water, mix for 1 min at low speed
		Add the remaining water, mix for 1 min at low speed	Add palygorskite clays suspension with the remaining mixing water, mix for 1 min at low speed	Add palygorskite clays suspension with the remaining mixing water, mix for 1 min at low speed
	Scrape the bowl, mix at medium speed of 285 rpm for 8 min			

6.3. PRELIMINARY WORK ON WORKABILITY OF BLENDED CEMENT MORTARS

6.3.1. MEASUREMENT OF RHEOLOGICAL PROPERTIES

All rheological characterization was performed on a temperature-controlled, stress-controlled rotational rheometer with a parallel-plate geometry. The top plate was 60 mm in diameter and the base plate was set at a constant temperature of 25°C. To prevent slip, 120-grit adhesive sandpaper was applied to both surfaces. To load the sample for testing, first the fresh mortar sample was placed on the base plate. Then the top plate was vertically displaced to squeeze the sample until the targeted initial gap height of 4 mm was reached. Once the initial gap was reached, excess sample was trimmed away.

The rheological test started with a pre-shear of 50 1/s for 120 s to ensure that all the samples were at a reproducible reference state. The sample was left to rest for 120 s to allow for stress relaxation before i) a linear shear ramp to obtain a flow curve and ii) tack test to obtain normal force evolution were applied. The protocol is summarized in Figure 69 and would be explained in detail below.

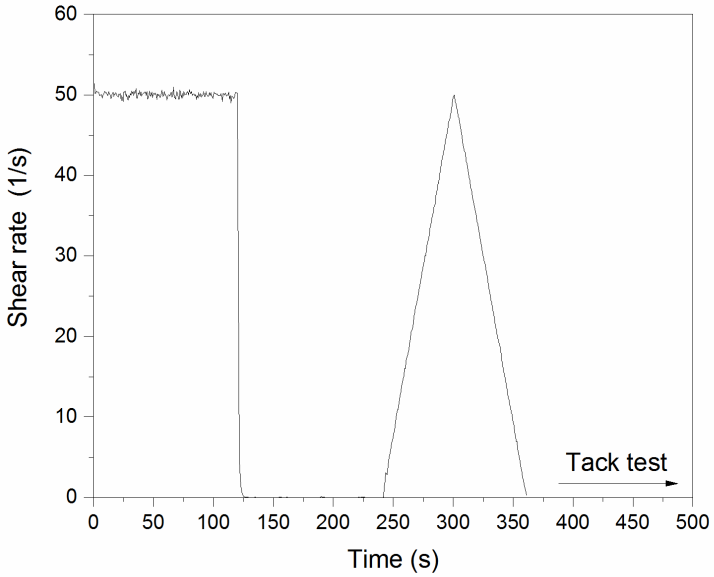

Figure 69. Rheological properties protocol.

6.3.2. RHEOLOGICAL PROPERTIES

The results of plastic viscosity and yield stress are presented in Figure 70, and the results of static cohesion are presented in Figure 71.

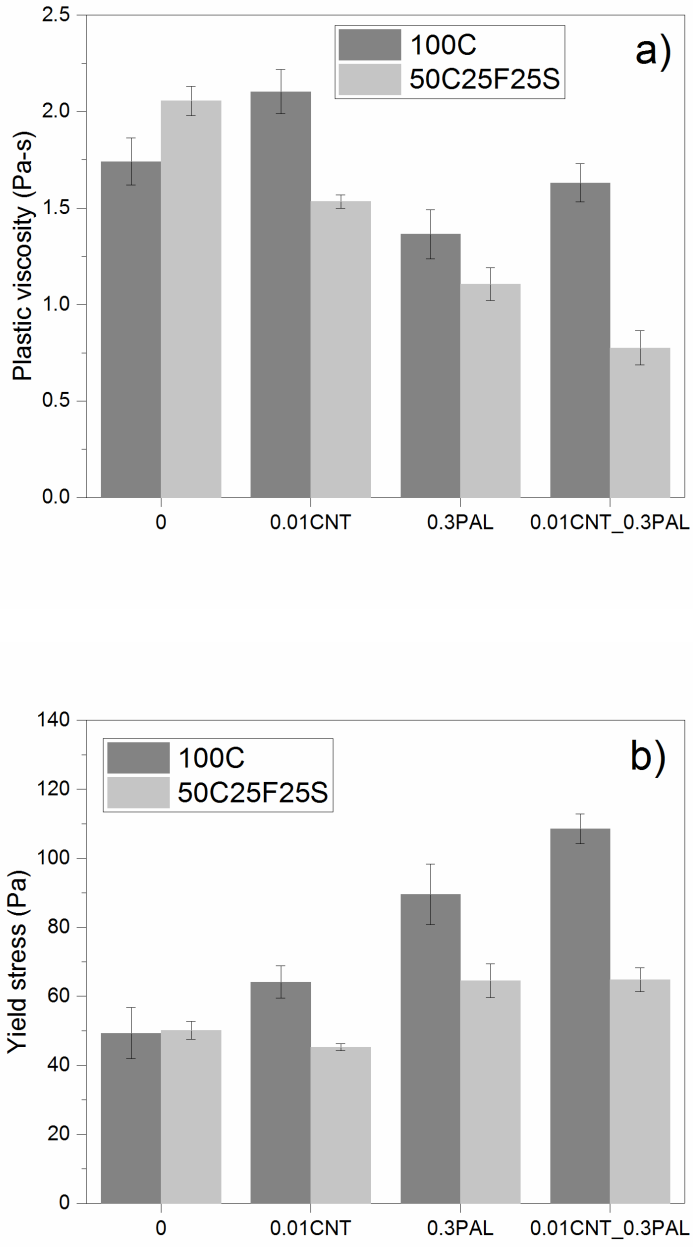

Figure 70. Effect of palygorskite clays and CNTs on the rheological properties of cement mortar and ternary mortar with 25% fly ash and 25% slag replacement of cement: (a) plastic viscosity and (b) yield stress.

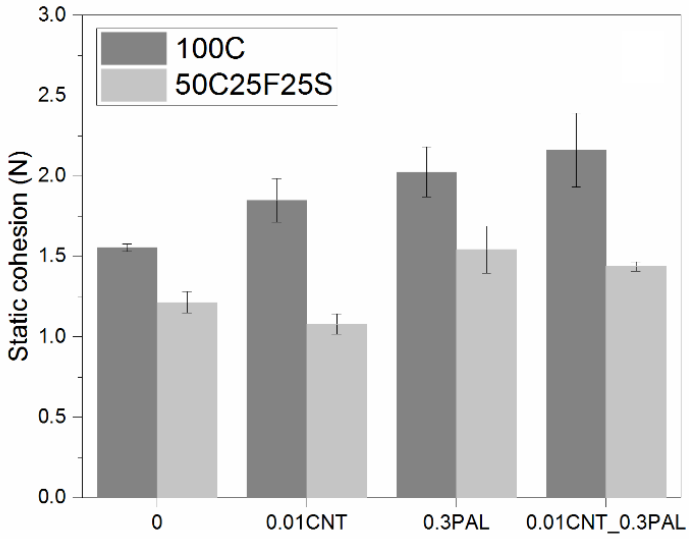

Figure 71. Effect of palygorskite clays and CNTs on the static cohesion of cement mortar and ternary mortar with 25% fly ash and 25% slag replacement of cement.

It is worth pointing out that the replacement of cement with fly ash and blast furnace slag does not have a notable effect on plastic viscosity, yield stress and static cohesion compared to the control cement mortar. Several factors potentially increase the rheological parameters: i) the lower specific gravity of fly ash and slag leads to a higher solid volume fraction of the mixture at a constant water-solid ratio on a mass basis [179]; ii) higher specific surface area improves the particle packing and reduces the inter-particle spacing [165,180]; iii) the angular geometry of slag enhances the friction between particles [165,167]; iv) SCMs can absorb superplasticizer and increase demand to maintain the same workability [166]. On the other hand, some factors decrease the rheological parameters: i) fly ash and blast furnace slag, which have lower hydraulic activity, dilute the active cement composition [170,174]; ii) coarse fly ash lowers the particle density and reduces particle connections [180]; iii) the spherical shape of fly ash reduces friction among particles, which is referred to as a “ball bearing” effect [169,172]. Our results show the overall effect of

these factors introduced by the SCMs is not notable, i.e. comparable to the control mortar. But CNTs and palygorskite clays have substantially different effects on each of the two systems, i.e. 100C and 50C255F25S, which would be discussed herein.

Starting with the effect of palygorskite clays, they increase the yield stress and static cohesion, which is consistent with other work [26,28,100,120]. As the palygorskite clays carry a negative charge on the faces and a positive charge on the ends [88], they tend to bond with each other by electrical attraction between opposite charges. Palygorskite clay's negatively charged surface can also associate with the surface of C_3S which is positively charged in cement suspensions [181]. However, the increasing effect is more apparent in the cement mortar than the ternary mortar - 81% vs 29% for yield stress and 30% and 27% for static cohesion in 100C and 50C25F25S, respectively. Similarly, for plastic viscosity, as shown in Figure 70 a), the addition of palygorskite clays reduce the plastic viscosity more significantly in the ternary mortar compared to the cement mortar – 46% versus 22%, respectively. This demonstrates that the palygorskite clays have the same effect on both systems but to different degrees, which would be important to consider in mix design. On the other hand, it was observed that the CNTs have opposing effects on each of the measured rheological parameters between the two systems. As shown in Figure 70 and Figure 71, for plastic viscosity, yield stress and static cohesion, CNTs lead to higher values in the cement mortars but lower values in the ternary mortars. It is unclear why the CNTs have these opposing effects and requires further investigation. But similarly to the palygorskite clays, it highlights the importance of considering the binder system when utilizing additives with exceptional surface properties like CNTs, which can have complex physical and chemical effects. Although base mixes may exhibit similar rheological parameters, the addition of CNTs combined with chemical admixtures can lead to differing effects on the resultant rheology depending on the mix constituents.

It should be noted that in all the studied cement systems, palygorskite clays increase yield stress and static cohesion but decrease plastic viscosity. The presence of superplasticizer combined with palygorskite clays in our mixtures can partially explain this. Some self-consolidating concrete applications require opposing effects on yield stress and plastic viscosity to get high workability during casting and low formwork pressure at rest. For this reason, a combination of superplasticizers and viscosity modifying admixtures (VMAs) is commonly used [31]. In this study, we found that combining superplasticizer and palygorskite clays can also achieve this goal - higher yield stress but lower plastic viscosity compared to the reference mortar.

Finally, combining palygorskite clays and CNTs shows a superimposing effect. When CNTs and clays have the same effect, i.e. increasing or decreasing, the combination amplifies the effect. When CNTs and clays have opposing effects, the gains offset the losses. This may indicate that no significant interaction occurs between the CNTs and clays in the fresh state.

It is interesting to note that yield stress results have a direct correlation with static cohesion in all studied systems. Some publications [70,71] have established the relationship between static cohesion with yield stress and plastic viscosity in squeeze flow, as illustrated in equation 28,

$$F_{max} = \frac{2\pi R^3 \tau_0}{3h_m} + \frac{3\pi\eta_{pl} R^4 V}{2{h_m}^3} \quad (28)$$

where F_{max} is the static cohesion, R is the radius of mortar sample, h_m is the plate distance at the maximum normal force F_{max}, and V is the pulling velocity of the plate.

In equation 29, the first term on the right-hand side is related to yield stress while the second one is related to plastic viscosity. In this study, since the pulling velocity of the plate is very low, 10 μm/s, the contribution of the second term is trivial (0.09%). Thus, the equation 29 becomes

$$F_{max} = \frac{2\pi R^3 \tau_0}{3h_m} \tag{29}$$

The static cohesion values measured directly by the tack test are compared against those derived from yield stress in Figure 72. They follow the same trend in both 100C and 50C25F25S but the values measured directly by the tack test were higher (1.87 times), which is in agreement with other work [70,71]. This can be attributed to a pinning effect related to the flow history [182] and that the static cohesion includes the weight of the sample whereas the yield stress does not [183].

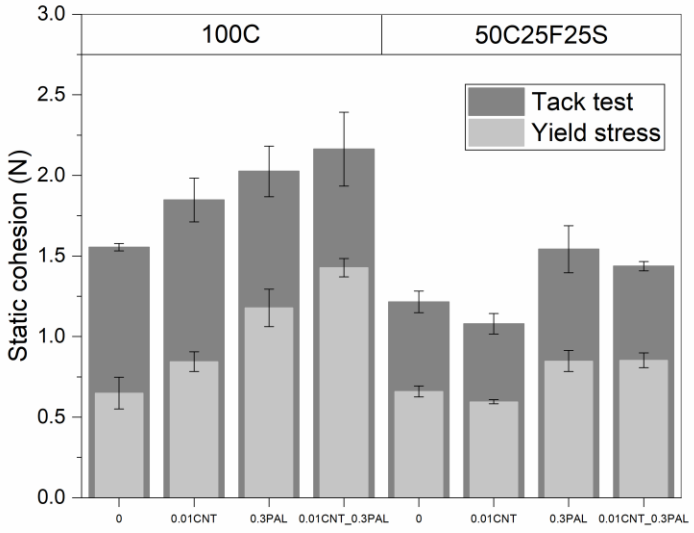

Figure 72. Static cohesion of different blended systems measured directly by tack test and calculated using yield stress in the flow curve.

6.4. HARDENED PROPERTIES OF BLENDED CEMENT MORTAR

6.4.1. MEASUREMENT METHODS OF HARDENED PROPERTIES

6.4.1.1. ELECTRICAL RESISTIVITY

The bulk electrical resistivity was measured using an electrical resistivity meter (RCON, Giatec, Canada), where two plate electrodes were placed on each end of the sample. The uniaxial measurements were performed at a single frequency of 1 kHz. The conductive gel was applied to ensure good electrical contact between the electrodes and specimen. The schematic of the setup is shown in Figure 73.

The mortar test specimens were cast in 50.8 mm cubic molds, demolded after 24 hours and cured in 100% relative humidity for 7 or 28 days. After wet curing the samples were air dried at a relative humidity of 50 ± 4% for 24 hours prior to testing.

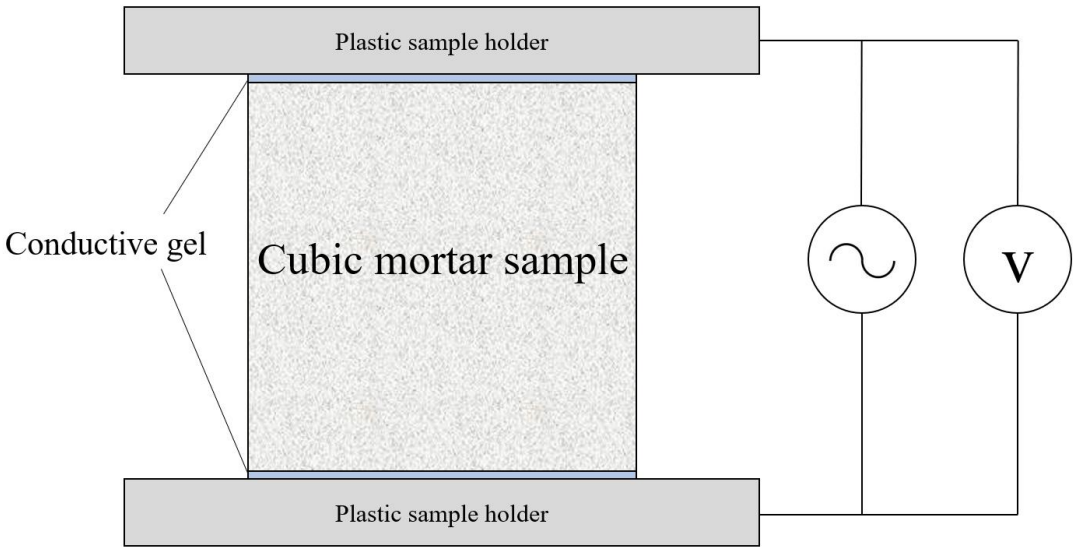

Figure 73. A schematic of electrical resistivity meter.

6.4.1.2. COMPRESSIVE STRENGTH

Following the electrical resistivity tests, compressive strength tests were conducted on the same samples. The loading rate was set as 890 N/s according to the procedure recommended by ASTM C109 [184].

6.4.1.3. TENSILE STRENGTH

Direct tensile strength was evaluated by performing the direct tension tests in accordance with AASHTO T132 [185] on dogbone-shaped paste samples with a 25.4 mm x 25.4 mm tapered cross-section. The loading rate was set at 5 mm/min.

In all the tests, at least three samples per mixture were tested and the average was taken to be the representative value. Error bars are included in all plots.

6.4.2. RESULTS OF HARDENED PROPERTIES

In addition to the fresh state, the influence of the palygorskite clay and CNT on the hardened state properties of the cement and blended systems were measured and the results are discussed herein.

6.4.2.1. COMPRESSIVE STRENGTH

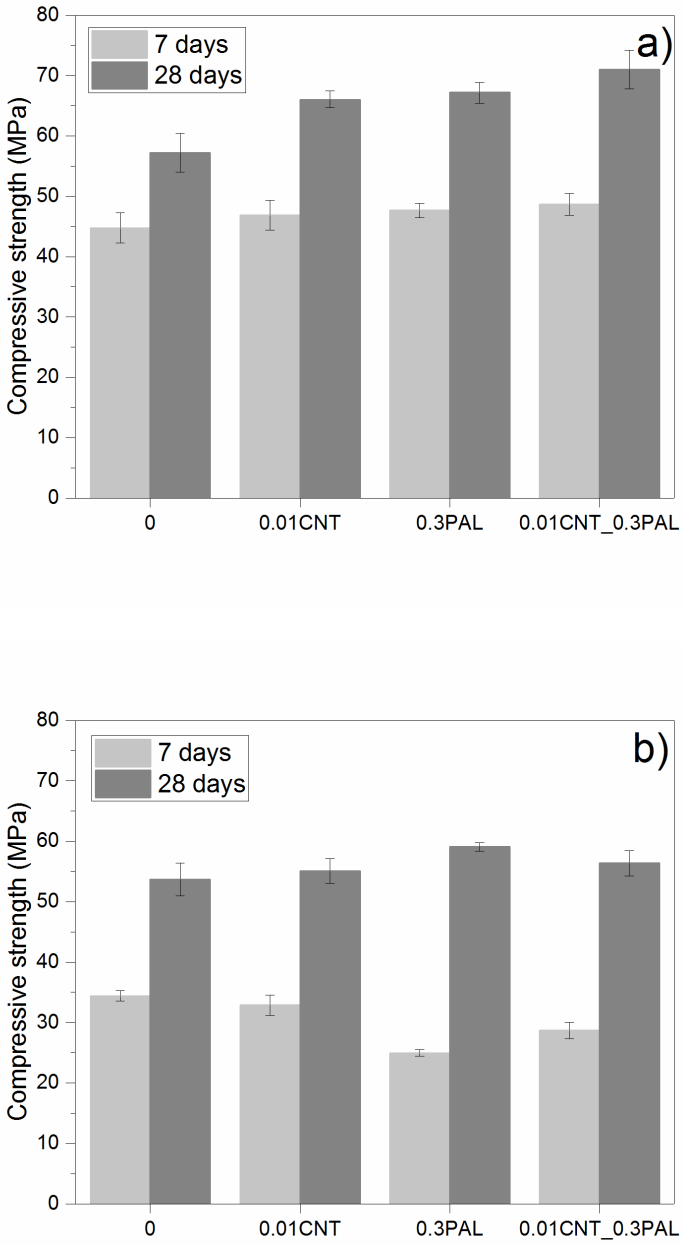

Figure 74. Compressive strength of a) cement mortar (100C) and b) fly ash-blast furnace slag-cement mortar (50C25F25S).

Figure 74 shows the 7 and 28 day compressive strength results of cement and blended mortar systems modified with palygorskite clays and CNTs. Figure 74 a) shows that at 7 days both the palygorskite clays

and CNTs increase the compressive strength of 100% cement mortar. At 28 days, the increase is more pronounced, where the CNTs, palygorskite clays, and the combination increase strength by 15, 17, and 24%, respectively, compared to the control. In contrast, as shown in Figure 74 b), the increase in the 28 day strength of the blended mortar is less significant at 3, 10, and 5% with the addition of CNTs, palygorskite clays and combination, respectively. As shown in cement mortar results, the CNTs and palygorskite clays enhancing effect increased along with the hydration. The poorer enhancing effect of blended mortar may attribute to the lower hydraulic activity of fly ash which dilutes the active cement composition. In general, similar to what was observed in the rheological results, the combination of the nanoadditives had a superimposing effect.

CNTs have been shown to modify the microstructure of cement paste. In a study by Konsta-Gdoutos et all, nanoindentation results showed that CNTs caused a shift in the distribution of phases to decrease porosity and increase the frequency of high stiffness calcium silicate hydrate (CSH) [178]. Further, Gdoutos et al. found that CNTs can improve the fracture and mechanical properties of cement mortars [186]. Therefore, the enhancing effect by the CNTs on the 100% cement mortar system captured in the present study agrees with the findings of other work. However, the same enhancing effect is not captured in the blended systems. The reason for this is unclear, and there is much less literature on the influence of CNTs in systems incorporating SCMs [187]. It should be the topic of future work.

Palygorskite clay is added to cement-based materials primarily to modify their rheology. However, results indicate that it can improve the mechanical properties, as well, especially at later ages. Results of Figure 74 a) show that the palygorskite clay and CNT have comparable effects on 28 day strength. Further, in Figure 74 b) it is shown that in the blended system, the palygorskite clay leads to a greater increase in 28 day strength than the CNT. This may be attributed to the clay acting as an effective rheological modifier to

improve suspension stability by enhancing segregation resistance [188], which would ultimately improve mechanical performance. . In addition, due to the hydrophilic nature of the palygorskite clay, they are expected to be more readily dispersible than CNTs.

6.4.2.2. ELECTRICAL RESISTIVITY

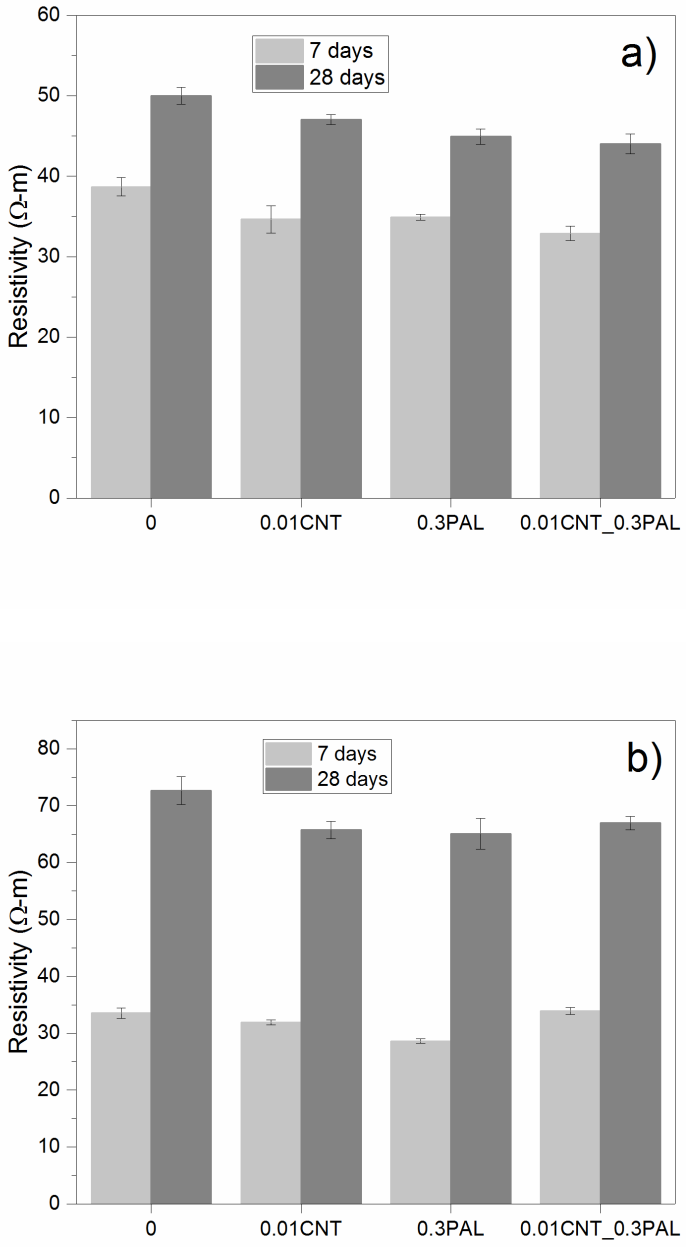

Figure 75. Electrical resistivity of a) cement mortar (100C) and b) fly ash-blast furnace slag-cement mortar (50C25F25S).

The results of electrical resistivity in the cement and blended systems are shown in Figure 75. It is apparent that the blended systems (Figure 75 a)) exhibit higher resistivity than the cement systems (Figure 75 b)).

Resistivity measurements of concrete depends on many factors, including the composition of the binder phases, the composition of the liquid phase and connectivity (or tortuosity) of the pore network [189]. In particular, hydroxide concentration is critical to the resistivity [190]. Therefore the higher overall resistivity of the blended systems may be partially attributed to the low alkali and hydroxide concentrations resulting from the incorporation of fly ash and slag. Due to the dependence of resistivity on binder composition, it is not possible to directly compare the cement samples against the blended samples. However, we can determine the influence of the nanomaterials on resistivity in the two groups of samples separately to gain some insight on how they refine pore structure, as well as to make correlations to compressive strength results.

Under unsealed conditions, water can evaporate out of the cement matrix. And degree of water loss would depend on the pore structure. An open, unpercolated microstructure would undergo high moisture loss, while a closed, highly percolated microstructure would undergo limited moisture loss. Water is characterized by a high conductivity, especially relative to cements, which are inherently insulating. Therefore, upon drying, a highly percolated microstructure, i.e. low permeability, would lead to low resistivity, and vice versa. The palygorskite clay and CNT both slightly decrease resistivity in both cement and blended systems, which may indicate the nanomaterials are refining pore structure. In fact, there is good agreement between the compressive strength and electrical conductivity results. Comparing the two sets of results, i.e. Figure 74 and Figure 75, similar inverse correlation trends can be observed – higher strength is associated with lower resistivity, and vice versa.

6.4.2.3. TENSILE STRENGTH

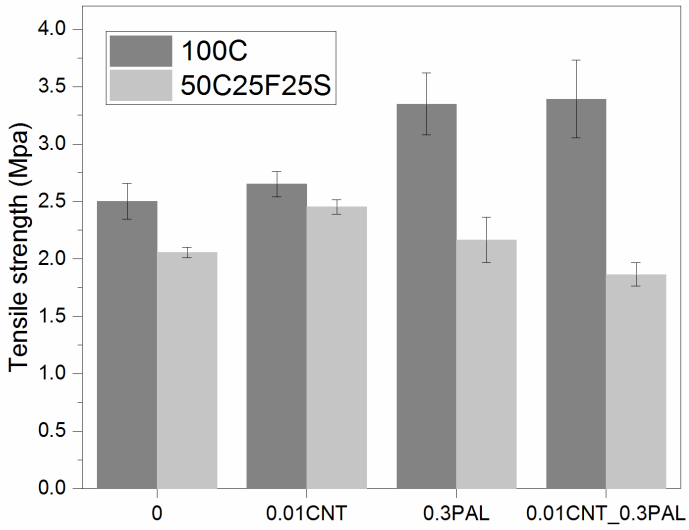

Figure 76. Direct tensile strength results at 28 days.

The 28 days direct tensile strength results are shown in Figure 76. The CNTs are found to increase tensile strength overall. However, a more pronounced effect is observed in the blended system than the cement – approximately 19% increase compared to the control. This is in contrast to their effect on compressive strength, where the enhancing effect of the CNTs was greater in the cement system than in the blended (Figure 74). This discrepancy may be partially attributed to the differing effect CNTs have on paste versus mortar systems, where the tensile strength test was performed on paste and the compressive strength test on mortar [186]. Also, the CNTs can modify the phase distribution of the matrix [178] but also can be having a reinforcing effect [191,192]. These mechanisms can lead to differences in performance under compression versus tension.

The palygorskite clays lead to a substantial increase in tensile strength in the cement system, approximately 33% compared to the control, and less so in the blended system. This, again, may be attributed to effective

dispersion and improved suspension stability, which would enhance the matrix properties. In fact, a similar trend was observed in the compressive strength results (Figure 74).

Looking at the effect of combining palygorskite clays and CNTs, theref is an increase in the cement system of 36% compared to the control. This is likely tied to the influence of the palygorskite clay, where the tensile strengths of 100C_0.3PAL and 100C_0.3PAL_0.01CNT are comparable. On the other hand, there is a slight decrease in tensile strength in the ternary system (50C25F25S_0.01CNT_0.3PAL) compared to the control (50C25F25S). This suggests that the palygorskite clays are hindering the reinforcing effect of the CNTs, possibly through disrupting the bonding. More work is needed to better understand the underlying mechanism.

6.4.3. SUMMARY

Figure 77 shows a summary of the rheological and hardened properties in the studied mixtures. Figure 77 presented the effect of CNT and clays (PAL) addition in two mortar systems: cement mortar in (a) and fly ash-blast furnace slag-cement mortar in (b). The parameters such as yield stress, plastic viscosity, static cohesion, tensile and compressive strength are compared before CNT/PAL addition (100% in magnitude) and after CNT/PAL addition. Except for the plastic viscosity, all the measured parameters (i.e. yield stress, static cohesion, compressive strength at 28 days and tensile strength at 28 days) were found to be highest for the combination of palygorskite clay and CNTs in the cement mortar compared with the control. It indicates some degree of synergy, as shown in green in Figure 77 a), where the mix combining palygorskite clay and CNTs envelop the other mixes. In comparison, there does not seem to be any apparent synergy in the blended system, as shown in Figure 77 b).

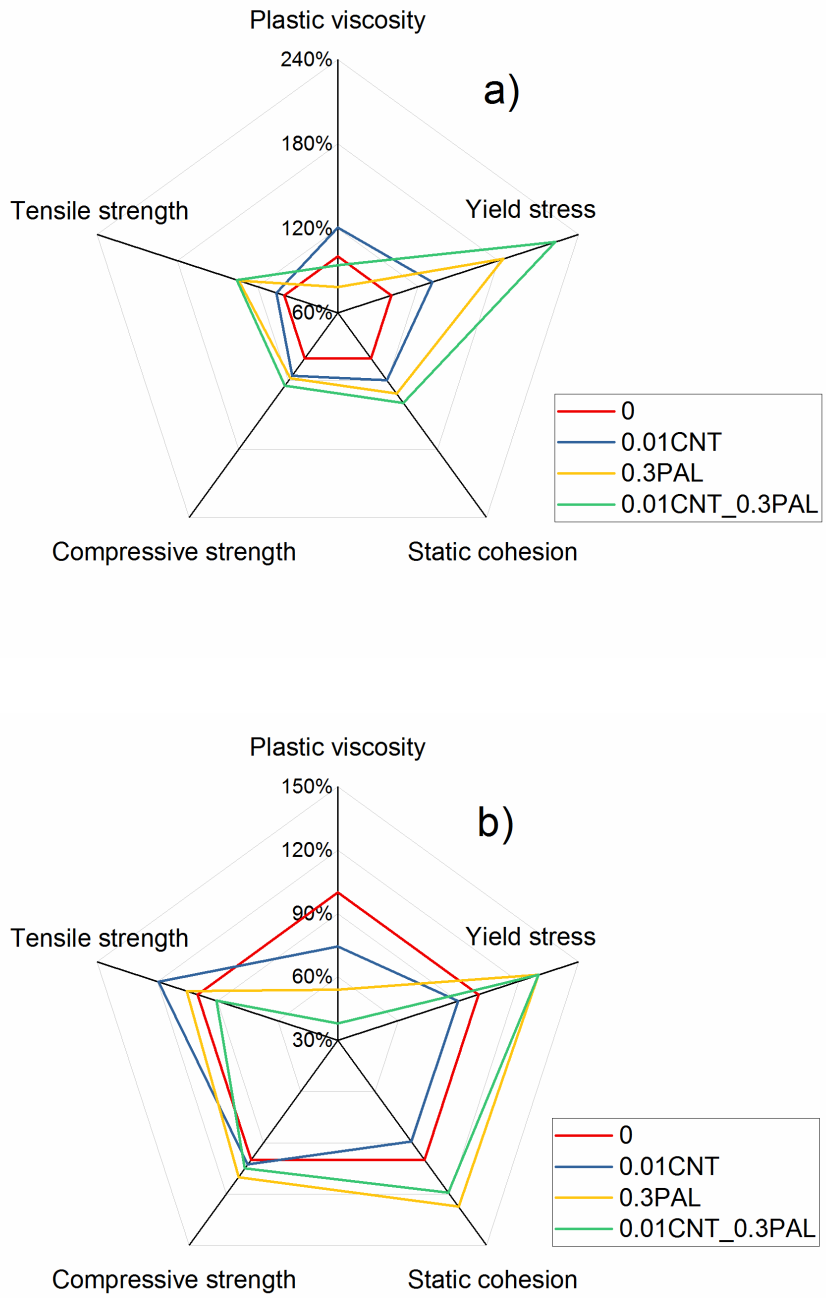

Figure 77. Summary of effect of palygorskite clays and CNTs on rheological properties and hardened properties a) cement mortar (100C) and b) fly ash-blast furnace slag-cement mortar (50C25F25S).

6.5. CONCLUSIONS

This study evaluated the effect of palygorskite clays and CNTs on the rheological and hardened properties of cement pastes and mortars incorporating fly ash and blast furnace slag. Results indicate the following conclusions:

1. Shear rheological and tack test results show that although the cement system and ternary system exhibited similar rheological parameters, i.e. yield stress, plastic viscosity and static cohesion, the introduction of additives had differing effects on each system. Palygorskite clays led to a more substantial i) increase in yield stress and static cohesion and ii) decrease in plastic viscosity in the cement system compared to the ternary system. CNTs increased all measured rheological parameters in the cement mortars and decreased them in the ternary mortars.

2. The rheological results highlight the importance of considering the binder system when utilizing additives with exceptional surface properties like CNTs and palygorskite clays. Although base mixes may exhibit similar rheological parameters, the incorporation of additives combined with chemical admixtures can lead to differing effects on the resultant rheology depending on the mix constituents.

3. Combining CNTs and palygorskite clays led to a superimposed effect on the rheological parameters, suggesting little interaction between the two additives in the fresh state.

4. Although palygorskite clays are utilized primarily to modify rheology, they can improve mechanical properties. In this study their effect was found to be comparable to or greater than that of the CNTs. This can be partially attributed to enhanced suspension stability and dispersibility of the palygorskite clays.

CHAPTER SEVEN

7. CONCLUSIONS AND FUTURE WORK

This chapter summarizes the main findings of this study by separating them into the following four sections: (1) the relationship between rheological and water transport properties of cement pastes; (2) a new non-linear thixotropy model is presented to describe the structural build-up process; (3) Synchrotron x-ray diffraction method of evaluating phase evolution at elevated temperature/pressure; (4) hardened properties of blended cement system.

7.1. THE RELATIONSHIP BETWEEN RHEOLOGICAL AND WATER TRANSPORT PROPERTIES OF CEMENT PASTES

The influence of nanoclay and diutan gum on bleeding has different working mechanisms. Nanoclay addition lowers the bleeding level and slows down the rate of bleeding due to the stronger particle interactions and denser cement filter cake it forms. This also leads to an increase in static yield stress. In contrast to nanoclay's effect on particle interaction, the diutan gum's effect on bleeding is more complex and may be attributed to three different mechanisms: (1) particle interaction: Above a critical concentration, at a concentration of 1.5%, diutan gum increases the static yield stress and decreases the bleeding level dramatically. (2) Above the critical concentration, an exponential rise in interstitial solution viscosity is found. The viscous drag force causes a progressive local reorganization of the cement paste system which leads to a sudden increase in bleeding rate. (3) At 4% concentration, although a decrease occurs in static yield, there is no apparent bleeding. The absence of bleeding may be attributed to diutan gum aggregates, which block the water flow path completely.

The influence of nanoclay and diutan gum on water retention was evaluated. Although clays have high water sorption capacity (nanoclay water sorption capacity of 200% by mass), water retention was independent of nanoclay addition. Diutan gum results highlighted the formation of polymer aggregates as the origin of higher interstitial solution viscosity and higher water retention capacity. Moreover, Darcy's law cannot be applied to the water retention results because the paste undergoes drying (approx. 25% of water is pulled from the cement paste by the filter paper) and Darcy's law requires the paste to be saturated. Furthermore, we found that water retention correlates well with those of interstitial solution viscosity and have the different tendency with apparent viscosity.

The influence of nanoclay and diutan gum on evaporation was determined. The rate of constant evaporation period was independent of W/C ratio, and bleed water was not found to affect evaporation rate. The nanoclay did not have a notable influence on evaporation water loss. Although diutan gum showed slightly lower evaporation rates, in practical terms, neither nanoclay nor diutan gum provided resistance to plastic shrinkage.

Future work

This section investigated the effect of nanoclay and diutan gum on water transport properties and identify the relationship between rheological and water transport properties of cement pastes. More work should be done in these fields:

1. Water movement in response to a gradient of pressure is complex and needs further investigation. Neutron imaging is a powerful method for quantifying water transport inside cement paste. It can

be used for clarifying the diutan gum and nanoclay effect on the water retention test and help in the interpretation of water retention results from standard water retention tests.

2. The formwork free 3D printed concrete would suffer from rapid evaporation of water. The excessive water loss would affect surface moisture of 3D printed concrete. The inter-layer strength of 3D printed concrete should be evaluated by controlling the water transport properties, i.e., evaporation, bleeding and water retention.
3. This study found neither nanoclay nor diutan gum provided resistance to plastic shrinkage. Therefore, other methods will be needed to ensure proper curing for 3D concrete printing, e.g., curing agents.

7.2. A NEW NON-LINEAR THIXOTROPY MODEL IS PRESENTED TO DESCRIBE THE STRUCTURAL BUILD-UP PROCESS

A simple thixotropy model was proposed. The new non-linear model exhibits good fitting with the experiment results of static yield stress and SAOS tests, which supports the assumption of the existence of the two structures (i.e., general floc and C-S-H nucleation) and corresponding kinetics.

$$\tau=\tau_0+c\lambda_{flocs}+A_{thix}t \tag{30}$$

$$G'=G'_0+c\lambda_{C\text{-}S\text{-}H}+G_{rigid}t \tag{31}$$

where $\tau 0$ is initial static yield stress, G'_0 is initial storage modulus, c corresponds to the fully developed λ ($\lambda=1$) condition, Athix is the rate of linear evolution of static yield stress and Grigid is the rate of linear evolution of storage modulus. This model was used to quantify the effect of different pre-shearing times and VMA additions on the build-up of these two structures.

Pre-shearing time leads to a different response regarding static yield stress and storage modulus. A longer pre-shearing time, associated with a more deflocculated structure, led to a lower initial static yield stress and decelerated the kinetics of rebuilding of static yield stress. At the same time, longer pre-shearing time led to higher storage modulus values, indicating a more percolated C-S-H network.

The results showed the necessity of using static yield stress test for monitoring the evolution of stress-bearing ability. SAOS, as a less time consuming, non-perturbing test, it can be considered as a desirable approach to characterize stress-bearing ability over time for these thixotropic systems. However, for cement pastes, storage modulus has entirely different time evolutions compared to static yield stress due to the two different "structures" in the paste. It highlights the necessity of using static yield stress test for monitoring the evolution of stress-bearing ability of cementitious materials, not just SAOS.

The shear stress applied during resting strongly influenced the static yield stress. The study proposed that anisotropic microstructures, which are induced by pre-shearing flow, is held by the stress during resting. Hence, jamming at a given sustained stress may induce a change in the microstructure, which was evident by the linear increase in static yield stress with increasing sustained stress levels. Thus, this is important to consider when characterizing static yield stress evolution for specific applications, e.g., cementing, formwork pressure, and 3D printing.

Nanoclay and diutan gum have a different effect on the attractive interactions of cement particles. Although both nanoclay and diutan gum were found to decrease storage modulus and increase static yield stress, overall, compared to the control paste starting from the same apparent viscosity, they had different effects on structural build-up kinetics. This was attributed to the differing mechanisms between the two VMAs.

Future work

This section demonstrated the validity of the non-linear build-up model and found that the shear stress applied during resting strongly influenced the static yield stress. There are many avenues for future work:

1. Since superplasticizers and hydration accelerate have great influence on the rheological properties, such as yield stress, viscosity, and thixotropy, the influence of these admixtures is to be explored by utilizing the non-linear model.
2. The static yield stress is strongly dependent on the sustained stress applied to the cement paste during rest. In 3D concrete printing, as the layer of fresh concrete filament is deposited, the influence of its self-weight (and weight of the subsequent layer above it) on the printed structures would be investigated.

7.3. SYNCHROTRON XRD METHOD OF EVALUATING PHASE EVOLUTION AT ELEVATED TEMPERATURE/PRESSURE

A cubic cell was developed for the test at high temperature and pressure. The cubic assembly consists of a PEEK cylindrical capsule, plugs, a layer of sodium chloride as pressure marker and a graphite heater. In the experiment, the slurry was cast in a PEEK cylindrical capsule. The capsule was vertically centered in the cubic assembly with PEEK plugs placed above and below. A layer of sodium chloride was added within to serve as a pressure marker. A graphite heater surrounded the capsule and plugs, through which electrical resistive heating was applied. In all test runs pressure was applied first, followed by temperature.

The influence of temperature on phase change was captured. The synchrotron XRD test setup effectively captures the consumption of C3S, ferrite, and gypsum, the conversion from ettringite to monosulfate, and the formation of portlandite and jaffeite of fresh cement slurries. Increasing temperature from 60ºC to 149ºC leads to an acceleration in portlandite formation and ettringite-monosulfate conversion. At 149ºC the formation of jaffeite occurs.

The seeding effect of nanoclay is observed. The nanoclays lead to a measurable acceleration in jaffeite and portlandite formation at 149ºC. This can potentially be due to a seeding effect, which is commonly observed when incorporating nanomaterials into cementitious systems.

Future work

This study investigated the influence of temperature and addition of nano-sized attapulgite clay on the phase evolution of oil well cement slurries. The following work should be done in the future:

1. As jaffeite is undesirable, leading to increasing in permeability, this is an important mix design consideration when incorporating attapulgite clays or other nanomaterials for oil well cementing applications. The method of mitigating jaffeite formation and promote amorphous C-S-H growth in systems would be explored.
2. The influence of pressure on the rheological properties of cement slurry should be investigated to give a comprehensive understanding of the effect of VMAs under the extreme oil well conditions.

7.4. HARDENED PROPERTIES OF BLENDED CEMENT SYSTEM

Results indicate that although the nanoclays are utilized primarily to modify rheology, they can also enhance mechanical properties. Nanoclays led to an increase in yield stress and static cohesion and

decrease in plastic viscosity in the blended cement systems. For compressive and tensile strength, the nanoclays effect was found to be comparable to or greater than that of the CNTs. This can be partially attributed to enhanced suspension stability and dispersibility of the nanoclays.

REFERENCES

[1] F. Ridi, E. Fratini, P. Baglioni, Cement: A two thousand year old nano-colloid, J. Colloid Interface Sci. 357 (2011) 255–264. doi:10.1016/j.jcis.2011.02.026.

[2] BP, Deepwater Horizon Accident Investigation Report, 2010.

[3] A Tricky Task: Cementing an Oil Well - Graphic - NYTimes.com, (n.d.). https://archive.nytimes.com/www.nytimes.com/interactive/2010/05/08/us/20100508-rig-diagram.html?_r=0 (accessed May 31, 2018).

[4] E.B. Nelson, D. Guillot, Well cementing., Schlumberger, 2006. https://books.google.com/books/about/Well_Cementing.html?id=FblqPAAACAAJ (accessed June 28, 2017).

[5] J. Desbrieres, Cement cake properties in static filtration. Influence of polymeric additives on cement filter cake permeability, Cem. Concr. Res. 23 (1993) 347–358. doi:10.1016/0008-8846(93)90100-N.

[6] B. Khoshnevis, R. Dutton, Innovative Rapid Prototyping Process Makes Large Sized, Smooth Surfaced Complex Shapes in a Wide Variety of Materials, Mater. Technol. 13 (1998) 53–56. doi:10.1080/10667857.1998.11752766.

[7] B. Khoshnevis, Automated construction by contour crafting—related robotics and information technologies, Autom. Constr. 13 (2004) 5–19. doi:10.1016/j.autcon.2003.08.012.

[8] T.T. Le, S.A. Austin, S. Lim, R.A. Buswell, R. Law, A.G.F. Gibb, T. Thorpe, Hardened properties of high-performance printing concrete, Cem. Concr. Res. 42 (2012) 558–566. doi:10.1016/j.cemconres.2011.12.003.

[9] S. Lim, R.A. Buswell, T.T. Le, S.A. Austin, A.G.F. Gibb, T. Thorpe, Developments in construction-scale additive manufacturing processes, Autom. Constr. 21 (2012) 262–268. doi:10.1016/j.autcon.2011.06.010.

[10] F. Bos, R. Wolfs, Z. Ahmed, T. Salet, Additive manufacturing of concrete in construction:

potentials and challenges of 3D concrete printing, Virtual Phys. Prototyp. 11 (2016) 209–225. doi:10.1080/17452759.2016.1209867.

[11] A. Kazemian, X. Yuan, E. Cochran, B. Khoshnevis, Cementitious materials for construction-scale 3D printing: Laboratory testing of fresh printing mixture, Constr. Build. Mater. 145 (2017) 639–647. doi:10.1016/J.CONBUILDMAT.2017.04.015.

[12] E. Lloret, A.R. Shahab, M. Linus, R.J. Flatt, F. Gramazio, M. Kohler, S. Langenberg, Complex concrete structures: Merging existing casting techniques with digital fabrication, CAD Comput. Aided Des. 60 (2015) 40–49. doi:10.1016/j.cad.2014.02.011.

[13] J.G. Sanjayan, B. Nematollahi, M. Xia, T. Marchment, Effect of surface moisture on inter-layer strength of 3D printed concrete, Constr. Build. Mater. 172 (2018) 468–475. doi:10.1016/j.conbuildmat.2018.03.232.

[14] D. Bülichen, J. Kainz, J. Plank, Working mechanism of methyl hydroxyethyl cellulose (MHEC) as water retention agent, Cem. Concr. Res. 42 (2012) 953–959. doi:10.1016/j.cemconres.2012.03.016.

[15] K.H. Khayat, Viscosity-enhancing admixtures for cement-based materials — An overview, Cem. Concr. Compos. 20 (1998) 171–188. doi:10.1016/S0958-9465(98)80006-1.

[16] W. Schmidt, H.J.H. Brouwers, H.-C. Kühne, B. Meng, The Working Mechanism of Starch and Diutan Gum in Cementitious and Limestone Dispersions in Presence of Polycarboxylate Ether Superplasticizers, Appl. Rheol. 23 (n.d.). doi:10.3933/ApplRheol-23-52903.

[17] W. Wang, A. Wang, Recent progress in dispersion of palygorskite crystal bundles for nanocomposites, Appl. Clay Sci. 119 (2016) 18–30. doi:10.1016/j.clay.2015.06.030.

[18] H.H. Murray, Overview — clay mineral applications, Appl. Clay Sci. 5 (1991) 379–395. doi:10.1016/0169-1317(91)90014-Z.

[19] ACTI-GEL® 208 - Acti-Gel, (n.d.). https://acti-gel.com/acti-gel/ (accessed April 24, 2018).

[20] E. Galan, Properties and Applications of Palygorskite-Sepiolite Clays, Clay Miner. 31 (1996) 443–453. doi:10.1180/claymin.1996.031.4.01.

[21] A. Ginez, Attapulgite as a Suspension Control Agent and Rheology Modifier in Flowables, in: Pestic. Formul. Appl. Syst. Glob. Pest Control Formul. Next Millenn. Ninet. Vol., ASTM International, 1999: pp. 108-108–10. doi:10.1520/STP14286S.

[22] T. Voigt, J.-J. Mbele, K. Wang, S.P. Shah, Using Fly Ash, Clay, and Fibers for Simultaneous Improvement of Concrete Green Strength and Consolidatability for Slip-Form Pavement, J. Mater. Civ. Eng. 22 (2010) 196–206. doi:10.1061/(ASCE)0899-1561(2010)22:2(196).

[23] J.H. Kim, M. Beacraft, S.P. Shah, Effect of mineral admixtures on formwork pressure of self-consolidating concrete, Cem. Concr. Compos. 32 (2010) 665–671. doi:10.1016/j.cemconcomp.2010.07.018.

[24] S. Kawashima, M. Chaouche, D.J. Corr, S.P. Shah, Rate of thixotropic rebuilding of cement pastes modified with highly purified attapulgite clays, Cem. Concr. Res. 53 (2013) 112–118. doi:10.1016/j.cemconres.2013.05.019.

[25] Y. Qian, S. Kawashima, Use of creep recovery protocol to measure static yield stress and structural rebuilding of fresh cement pastes, Cem. Concr. Res. 90 (2016) 73–79. doi:10.1016/j.cemconres.2016.09.005.

[26] Z. Quanji, G.R. Lomboy, K. Wang, Influence of nano-sized highly purified magnesium alumino silicate clay on thixotropic behavior of fresh cement pastes, Constr. Build. Mater. 69 (2014) 295–300. doi:10.1016/j.conbuildmat.2014.07.050.

[27] R.D. Ferron, S. Shah, E. Fuente, C. Negro, Aggregation and breakage kinetics of fresh cement paste, Cem. Concr. Res. 50 (2013) 1–10. doi:10.1016/j.cemconres.2013.03.002.

[28] N.A. Tregger, M.E. Pakula, S.P. Shah, Influence of clays on the rheology of cement pastes, Cem. Concr. Res. 40 (2010) 384–391. doi:10.1016/j.cemconres.2009.11.001.

[29] T. Conte, M. Chaouche, Rheological behavior of cement pastes under Large Amplitude Oscillatory Shear, Cem. Concr. Res. 89 (2016) 332–344. doi:10.1016/j.cemconres.2016.07.014.

[30] J. Plank, Applications of biopolymers and other biotechnological products in building materials, Appl. Microbiol. Biotechnol. 66 (2004) 1–9. doi:10.1007/s00253-004-1714-3.

[31] M. Palacios, R.J. Flatt, 20 – Working mechanism of viscosity-modifying admixtures, in: Sci. Technol. Concr. Admixtures, 2016: pp. 415–432. doi:10.1016/B978-0-08-100693-1.00020-5.

[32] L. Xu, H. Gong, M. Dong, Y. Li, Rheological properties and thickening mechanism of aqueous diutan gum solution: Effects of temperature and salts, Carbohydr. Polym. 132 (2015) 620–629. doi:10.1016/J.CARBPOL.2015.06.083.

[33] K.H. Khayat, N. Mikanovic, Viscosity-enhancing admixtures and the rheology of concrete, in: Underst. Rheol. Concr., Elsevier, 2012: pp. 209–228. doi:10.1533/9780857095282.2.209.

[34] E. Üzer, J. Plank, Impact of welan gum stabilizer on the dispersing performance of polycarboxylate superplasticizers, Cem. Concr. Res. 82 (2016) 100–106. doi:10.1016/j.cemconres.2015.12.009.

[35] N. Roussel, G. Ovarlez, S. Garrault, C. Brumaud, The origins of thixotropy of fresh cement pastes, Cem. Concr. Res. 42 (2012) 148–157. doi:10.1016/j.cemconres.2011.09.004.

[36] R.J. Flatt, P. Bowen, Yodel: A Yield Stress Model for Suspensions, J. Am. Ceram. Soc. 89 (2006) 1244–1256. doi:10.1111/j.1551-2916.2005.00888.x.

[37] R.J. Flatt, P. Bowen, Electrostatic repulsion between particles in cement suspensions: Domain of validity of linearized Poisson–Boltzmann equation for nonideal electrolytes, Cem. Concr. Res. 33 (2003) 781–791. doi:10.1016/S0008-8846(02)01059-1.

[38] N. Roussel, A. Lemaître, R.J. Flatt, P. Coussot, Steady state flow of cement suspensions: A micromechanical state of the art, Cem. Concr. Res. 40 (2010) 77–84. doi:10.1016/j.cemconres.2009.08.026.

[39] N. Roussel, Steady and transient flow behaviour of fresh cement pastes, Cem. Concr. Res. 35 (2005) 1656–1664. doi:10.1016/j.cemconres.2004.08.001.

[40] N. Roussel, A thixotropy model for fresh fluid concretes: Theory, validation and applications, Cem. Concr. Res. 36 (2006) 1797–1806. doi:10.1016/j.cemconres.2006.05.025.

[41] R.J. Flatt, Dispersion forces in cement suspensions, Cem. Concr. Res. 34 (2004) 399–408. doi:10.1016/j.cemconres.2003.08.019.

[42] G. Sant, C.F. Ferraris, J. Weiss, Rheological properties of cement pastes: A discussion of structure formation and mechanical property development, Cem. Concr. Res. 38 (2008) 1286–1296. doi:10.1016/j.cemconres.2008.06.008.

[43] H. Sleiman, A. Perrot, S. Amziane, A new look at the measurement of cementitious paste setting by Vicat test, Cem. Concr. Res. 40 (2010) 681–686. doi:10.1016/J.CEMCONRES.2009.12.001.

[44] S. Amziane, A. Perrot, T. Lecompte, A novel settling and structural build-up measurement method, Meas. Sci. Technol. 19 (2008) 105702. doi:10.1088/0957-0233/19/10/105702.

[45] S. Amziane, A. Perrot, The plate test carried out on fresh cement-based materials:How and why?, Cem. Concr. Res. 93 (2017) 1–7. doi:10.1016/J.CEMCONRES.2016.12.002.

[46] ASTM D3080/D3080M, Standard Test Method for Direct Shear Test of Soils Under Consolidated Drained Conditions, ASTM Int. (2011). doi:10.1520/D3080_D3080M-11.

[47] J.J. Assaad, J. Harb, Y. Maalouf, Measurement of yield stress of cement pastes using the direct shear test, J. Nonnewton. Fluid Mech. 214 (2014) 18–27. doi:10.1016/j.jnnfm.2014.10.009.

[48] R. Alfani, G.L. Guerrini, Rheological test methods for the characterization of extrudable cement-based materials—A review, Mater. Struct. 38 (2005) 239–247. doi:10.1007/BF02479349.

[49] R.J.M. Wolfs, F.P. Bos, T.A.M. Salet, Early age mechanical behaviour of 3D printed concrete: Numerical modelling and experimental testing, Cem. Concr. Res. 106 (2018) 103–116. doi:10.1016/J.CEMCONRES.2018.02.001.

[50] G. Lu, K. Wang, Investigation into Yield Behavior of Fresh Cement Paste: Model and Experiment, ACI Mater. J. 107 (2010) 12–19. https://s3.amazonaws.com/academia.edu.documents/40688619/2010-ACI-rheology-LuG.pdf?AWSAccessKeyId=AKIAIWOWYYGZ2Y53UL3A&Expires=1527388662&Signature=U4Mo0nvCIxuxC02BS20LLn4ulPo%3D&response-content-disposition=inline%3Bfilename%3DInvestigation_into_Yield (accessed May 26, 2018).

[51] ASTM D2166/D2166M - 16, Standard Test Method for Unconfined Compressive Strength of Cohesive Soil, ASTM Int. (2016). doi:10.1520/D2166_D2166M-16.

[52] T. Voigt, T. Malonn, S.P. Shah, Green and early age compressive strength of extruded cement mortar monitored with compression tests and ultrasonic techniques, Cem. Concr. Res. 36 (2006) 858–867. doi:10.1016/j.cemconres.2005.09.005.

[53] J. Assaad, J.J., Harb, Assessment of thixotropy of fresh mortars by triaxial and unconfined compression testing, Adv. Civ. Eng. Mater. (2012) 1–19. doi:10.1520/ACEM104469.

[54] P. Coussot, Q.D. Nguyen, H.T. Huynh, D. Bonn, Avalanche Behavior in Yield Stress Fluids, Phys. Rev. Lett. 88 (2002) 175501. doi:10.1103/PhysRevLett.88.175501.

[55] P. V. Liddel, D. V. Boger, Yield stress measurements with the vane, J. Nonnewton. Fluid Mech. 63 (1996) 235–261. doi:10.1016/0377-0257(95)01421-7.

[56] A.W. Saak, H.M. Jennings, S.P. Shah, The influence of wall slip on yield stress and viscoelastic measurements of cement paste, Cem. Concr. Res. 31 (2001) 205–212. doi:10.1016/S0008-8846(00)00440-3.

[57] C. Derec, G. Ducouret, A. Ajdari, F. Lequeux, Aging and nonlinear rheology in suspensions of polyethylene oxide–protected silica particles, Phys. Rev. E - Stat. Physics, Plasmas, Fluids, Relat. Interdiscip. Top. 67 (2003) 9. doi:10.1103/PhysRevE.67.061403.

[58] G. Ovarlez, X. Chateau, Influence of shear stress applied during flow stoppage and rest period on the mechanical properties of thixotropic suspensions, AIP Conf. Proc. 1027 (2008) 1042–1044. doi:10.1103/PhysRevE.77.061403.

[59] M. Fourmentin, P. Faure, S. Rodts, U. Peter, D. Lesueur, D. Daviller, P. Coussot, NMR observation of water transfer between a cement paste and a porous medium, Cem. Concr. Res. 95 (2017) 56–64. doi:10.1016/j.cemconres.2017.02.027.

[60] Y. Qian, S. Kawashima, Distinguishing dynamic and static yield stress of fresh cement mortars through thixotropy, Cem. Concr. Compos. 86 (2018) 288–296. doi:10.1016/J.CEMCONCOMP.2017.11.019.

[61] M. Fourmentin, G. Ovarlez, P. Faure, U. Peter, D. Lesueur, D. Daviller, P. Coussot, Rheology of lime paste - a comparison with cement paste, Rheol. Acta. 54 (2015) 647–656.

doi:10.1007/s00397-015-0858-7.

[62] A.W. Saak, H.M. Jennings, S.P. Shah, A generalized approach for the determination of yield stress by slump and slump flow, Cem. Concr. Res. 34 (2004) 363–371. doi:10.1016/j.cemconres.2003.08.005.

[63] N. Roussel, P. Coussot, "Fifty-cent rheometer" for yield stress measurements: From slump to spreading flow, J. Rheol. (N. Y. N. Y). 49 (2005) 705–718. doi:10.1122/1.1879041.

[64] N. Roussel, Correlation between Yield Stress and Slump: Comparison between Numerical Simulations and Concrete Rheometers Results, Mater. Struct. 39 (2007) 501–509. doi:10.1617/s11527-005-9035-2.

[65] N. Tregger, L. Ferrara, S.P. Shah, Identifying viscosity of cement paste from mini-slump-flow test, ACI Mater. J. 105 (2008) 558–566. doi:10.14359/20197.

[66] K.H. Khayat, A.F. Omran, S. Naji, P. Billberg, A. Yahia, Field-oriented test methods to evaluate structural build-up at rest of flowable mortar and concrete, Mater. Struct. 45 (2012) 1547–1564. doi:10.1617/s11527-012-9856-8.

[67] P. Coussot, S. Boyer, Determination of yield stress fluid behaviour from inclined plane test, Rheol. Acta. 34 (1995) 534–543. doi:10.1007/BF00712314.

[68] O.H. Wallevik, D. Feys, J.E. Wallevik, K.H. Khayat, Avoiding inaccurate interpretations of rheological measurements for cement-based materials, Cem. Concr. Res. 78 (2015) 100–109. doi:10.1016/J.CEMCONRES.2015.05.003.

[69] Y.O. Mohamed Abdelhaye, M. Chaouche, H. Van Damme, The tackiness of smectite muds. 1. The dilute regime, Appl. Clay Sci. 42 (2008) 163–167. doi:10.1016/j.clay.2008.01.018.

[70] A. Kaci, R. Bouras, V.T. Phan, P.A. Andréani, M. Chaouche, H. Brossas, Adhesive and rheological properties of fresh fibre-reinforced mortars, Cem. Concr. Compos. 33 (2011) 218–224. doi:10.1016/j.cemconcomp.2010.10.009.

[71] G. Meeten, Constant-force squeeze flow of soft solids, Rheol. Acta. 41 (2002) 557–566. doi:10.1007/s00397-002-0241-3.

[72] N. Roussel, Understanding the rheology of concrete, Woodhead Publishing, 2012. http://www.sciencedirect.com.ezproxy.cul.columbia.edu/science/book/9780857090287 (accessed April 17, 2017).

[73] H. Okamura, M. Ouchi, Self-Compacting Concrete, J. Adv. Concr. Technol. 1 (2003) 5–15. http://www.j-act.org/headers/1_5.pdf (accessed May 29, 2018).

[74] N. Roussel, Rheology of fresh concrete: From measurements to predictions of casting processes, Mater. Struct. Constr. 40 (2007) 1001–1012. doi:10.1617/s11527-007-9313-2.

[75] American Society for Testing and Materials, ASTM C1611/C1611M: Standard Test Method for Slump Flow of Self-Consolidating Concrete, (n.d.). https://compass.astm.org/EDIT/html_annot.cgi?C1611+14 (accessed May 31, 2018).

[76] G.H. TATTERSALL, Structural Breakdown of Cement Pastes at Constant Rate of Shear, Nature. 175 (1955) 166–166. doi:10.1038/175166a0.

[77] D.C.-H. Cheng, F. Evans, Phenomenological characterization of the rheological behaviour of inelastic reversible thixotropic and antithixotropic fluids, Br. J. Appl. Phys. 16 (1965) 1599–1617. doi:10.1088/0508-3443/16/11/301.

[78] H.-J. Kuzel, Initial hydration reactions and mechanisms of delayed ettringite formation in Portland cements, Cem. Concr. Compos. 18 (1996) 195–203. doi:10.1016/0958-9465(96)00016-9.

[79] A. Perrot, T. Lecompte, H. Khelifi, C. Brumaud, J. Hot, N. Roussel, Yield stress and bleeding of fresh cement pastes, Cem. Concr. Res. 42 (2012) 937–944. doi:10.1016/j.cemconres.2012.03.015.

[80] S. Ghourchian, M. Wyrzykowski, P. Lura, The bleeding test: A simple method for obtaining the permeability and bulk modulus of fresh concrete, Cem. Concr. Res. 89 (2016) 249–256. doi:10.1016/j.cemconres.2016.08.016.

[81] P. Mehta, P.J.M. Monteiro, Concrete: Microstructure, Properties, and Materials, McGraw-Hill Education, 2006.

[82] R. Pei, J. Liu, S. Wang, Use of bacterial cell walls as a viscosity-modifying admixture of concrete, Cem. Concr. Compos. 55 (2015) 186–195. doi:10.1016/J.CEMCONCOMP.2014.08.007.

[83] Standard DIN 18555-7, Testing of mortars containing mineral binders; determination of water retentivity of freshly mixed mortar by the filter plate method, Dtsch. Inst. Für Normung. (2000). https://standards.globalspec.com/std/88279/din-18555-7 (accessed February 19, 2018).

[84] L. Patural, P. Porion, H. Van Damme, A. Govin, P. Grosseau, B. Ruot, O. Devès, A pulsed field gradient and NMR imaging investigations of the water retention mechanism by cellulose ethers in mortars, Cem. Concr. Res. 40 (2010) 1378–1385. doi:10.1016/j.cemconres.2010.04.001.

[85] S. Ghourchian, M. Wyrzykowski, L. Baquerizo, P. Lura, Susceptibility of Portland cement and blended cement concretes to plastic shrinkage cracking, Cem. Concr. Compos. 85 (2018) 44–55. doi:10.1016/j.cemconcomp.2017.10.002.

[86] T. Poinot, A. Govin, P. Grosseau, Importance of coil-overlapping for the effectiveness of hydroxypropylguars as water retention agent in cement-based mortars, Cem. Concr. Res. 56 (2014) 61–68. doi:10.1016/j.cemconres.2013.11.005.

[87] T.S. Tan, T.H. Wee, S.A. Tan, C.T. Tam, S.L. Lee, A consolidation model for bleeding of cement paste, Adv. Cem. Res. 1 (1987) 18–26. doi:10.1680/adcr.1987.1.1.18.

[88] E. Cao, R. Bryant, D.J.A. Williams, Electrochemical Properties of Na–Attapulgite, J. Colloid Interface Sci. 179 (1996) 143–150. doi:10.1006/jcis.1996.0196.

[89] A. Zingg, F. Winnefeld, L. Holzer, J. Pakusch, S. Becker, L. Gauckler, Adsorption of polyelectrolytes and its influence on the rheology, zeta potential, and microstructure of various cement and hydrate phases, J. Colloid Interface Sci. 323 (2008) 301–312. doi:10.1016/j.jcis.2008.04.052.

[90] S. Ma, Y. Qian, S. Kawashima, Experimental and modeling study on the non-linear structural build-up of fresh cement pastes incorporating viscosity modifying admixtures, Cem. Concr. Res. 108 (2018) 1–9. doi:10.1016/j.cemconres.2018.02.022.

[91] Y. Fan, S. Zhang, S. Kawashima, S.P. Shah, Influence of kaolinite clay on the chloride diffusion property of cement-based materials, Cem. Concr. Compos. 45 (2014) 117–124. doi:10.1016/j.cemconcomp.2013.09.021.

[92] S. Ma, Y. Qian, S. Kawashima, Performance-based study on the rheological and hardened properties of blended cement mortars incorporating palygorskite clays and carbon nanotubes, Constr. Build. Mater. 171 (2018) 663–671. doi:10.1016/j.conbuildmat.2018.03.121.

[93] S. Kawashima, P. Hou, D.J. Corr, S.P. Shah, Modification of cement-based materials with nanoparticles, Cem. Concr. Compos. 36 (2013) 8–15. doi:10.1016/j.cemconcomp.2012.06.012.

[94] S. Ma, T. Yu, Y. Wang, M. Chaouche, S. Kawashima, Phase Evolution of Oil Well Cements with Nano-additive at Elevated Temperature/Pressure, ACI Mater. J. 113 (2016). doi:10.14359/51689104.

[95] C.-K. Loh, T.-S. Tan, T.-S. Yong, T.-H. Wee, An experimental study on bleeding and channelling of cement paste and mortar, Adv. Cem. Res. 10 (1998) 1–16. doi:10.1680/adcr.1998.10.1.1.

[96] N. Massoussi, E. Keita, N. Roussel, The heterogeneous nature of bleeding in cement pastes, Cem. Concr. Res. 95 (2017) 108–116. doi:10.1016/j.cemconres.2017.02.012.

[97] C. Brumaud, H. Bessaies-Bey, C. Mohler, R. Baumann, M. Schmitz, M. Radler, N. Roussel, Cellulose ethers and water retention, Cem. Concr. Res. 53 (2013) 176–184. doi:10.1016/j.cemconres.2013.06.010.

[98] C. Marliere, E. Mabrouk, M. Lamblet, P. Coussot, How water retention in porous media with cellulose ethers works, Cem. Concr. Res. 42 (2012) 1501–1512. doi:10.1016/j.cemconres.2012.08.010.

[99] A. Pierre, A. Perrot, V. Picandet, Y. Guevel, Cellulose ethers and cement paste permeability, Cem. Concr. Res. 72 (2015) 117–127. doi:10.1016/j.cemconres.2015.02.013.

[100] S. Kawashima, J.H. Kim, D.J. Corr, S.P. Shah, Study of the mechanisms underlying the fresh-state response of cementitious materials modified with nanoclays, Constr. Build. Mater. 36 (2012) 749–757. doi:10.1016/j.conbuildmat.2012.06.057.

[101] J. Xu, A. Wang, Electrokinetic and Colloidal Properties of Homogenized and Unhomogenized Palygorskite in the Presence of Electrolytes, J. Chem. Eng. Data. 57 (2012) 1586–1593. doi:10.1021/je300213u.

[102] L. Patural, P. Marchal, A. Govin, P. Grosseau, B. Ruot, O. Devès, Cellulose ethers influence on water retention and consistency in cement-based mortars, Cem. Concr. Res. 41 (2010) 46–55. doi:10.1016/j.cemconres.2010.09.004.

[103] Y. Ohama, Polymer-based admixtures, Cem. Concr. Compos. 20 (1998) 189–212. doi:10.1016/S0958-9465(97)00065-6.

[104] C.B. Skaggs, W.G. Rakitsky, S.F. Whitaker, Applications of Rheological Modifiers and Superplasticizers in Cementitious Systems, Spec. Publ. 148 (1994) 189–208. doi:10.14359/4276.

[105] P. Lura, B. Pease, G.B. Mazzotta, F. Rajabipour, J. Weiss, Influence of Shrinkage-Reducing Admixtures on Development of Plastic Shrinkage Cracks, ACI Mater. J. 104 (2007) 187–194. doi:10.14359/18582.

[106] G.W. Scherer, Theory of Drying, J. Am. Ceram. Soc. 73 (1990) 3–14. doi:10.1111/j.1151-2916.1990.tb05082.x.

[107] J. Hu, Z. Ge, K. Wang, Influence of cement fineness and water-to-cement ratio on mortar early-age heat of hydration and set times, Constr. Build. Mater. 50 (2014) 657–663. doi:10.1016/J.CONBUILDMAT.2013.10.011.

[108] S.-T. Lin, R. Huang, Effect of viscosity modifying agent on plastic shrinkage cracking of cementitious composites, Mater. Struct. 43 (2010) 651–664. doi:10.1617/s11527-009-9518-7.

[109] P. Billberg, Form pressure generated by self-compacting concrete : influence of thixotropy and structural behaviour at rest, Royal Institute of Technology, Dept. of Civil and Structural Engineering, 2006.

[110] A.M. Mostafa, A. Yahia, New approach to assess build-up of cement-based suspensions, Cem. Concr. Res. 85 (2016) 174–182. doi:10.1016/j.cemconres.2016.03.005.

[111] Q. Yuan, D. Zhou, K.H. Khayat, D. Feys, C. Shi, On the measurement of evolution of structural build-up of cement paste with time by static yield stress test vs. small amplitude oscillatory shear test, Cem. Concr. Res. 99 (2017) 183–189. doi:10.1016/j.cemconres.2017.05.014.

[112] ACTI-GEL® 208 - Active Minerals International, LLC, (n.d.). http://www.acti-gel.com/acti-gel-

208#hw (accessed April 21, 2017).

[113] M. Sonebi, Rheological properties of grouts with viscosity modifying agents as diutan gum and welan gum incorporating pulverised fly ash, Cem. Concr. Res. 36 (2006) 1609–1618. doi:10.1016/j.cemconres.2006.05.016.

[114] M.A. Schultz, L.J. Struble, Use of oscillatory shear to study flow behavior of fresh cement paste, Cem. Concr. Res. 23 (1993) 273–282. doi:10.1016/0008-8846(93)90092-N.

[115] A.I. Malkin, A.I. Isayev, Rheology : concepts, methods, and applications, n.d. https://books.google.com/books?id=66ARDQAAQBAJ&pg=PA47&lpg=PA47&dq=This+assumption+immediately+leads+to+the+following+first-order+kinetic+equation&source=bl&ots=C0sKaoYyqm&sig=MkJ2uyjsuxEbbZ-9Utd_rGrmCXc&hl=en&sa=X&ved=0ahUKEwiH6JLWzr7TAhWBdSYKHXQfDugQ6AE (accessed April 24, 2017).

[116] S.-Y. Yoon, Y. Deng, Flocculation and reflocculation of clay suspension by different polymer systems under turbulent conditions, J. Colloid Interface Sci. 278 (2004) 139–145. doi:10.1016/j.jcis.2004.05.011.

[117] J.H. Kim, H.J. Yim, R.D. Ferron, *In situ* measurement of the rheological properties and agglomeration on cementitious pastes, J. Rheol. (N. Y. N. Y). 60 (2016) 695–704. doi:10.1122/1.4954251.

[118] T. Hao, R.E. Riman, Calculation of interparticle spacing in colloidal systems, J. Colloid Interface Sci. 297 (2006) 374–377. doi:10.1016/j.jcis.2004.10.014.

[119] G. Ovarlez, 2 – Introduction to the rheometry of complex suspensions, in: Underst. Rheol. Concr., 2012: pp. 23–62. doi:10.1533/9780857095282.1.23.

[120] S. Kawashima, M. Chaouche, D.J. Corr, S.P. Shah, Influence of purified attapulgite clays on the adhesive properties of cement pastes as measured by the tack test, Cem. Concr. Compos. 48 (2014) 35–41. doi:10.1016/j.cemconcomp.2014.01.005.

[121] S.H. Change, M.E. Ryan, R.K. Gupta, The effect of pH, ionic strength, and temperature on the

rheology and stability of aqueous clay suspensions, Rheol. Acta Rheol Acta. 32 (1993) 263–269. https://link.springer.com/content/pdf/10.1007%2FBF00434190.pdf (accessed December 18, 2017).

[122] R. Lapasin, S. Pricl, Rheology of Industrial Polysaccharides: Theory and Applications, Springer US, 1995. https://books.google.com/books/about/Rheology_of_Industrial_Polysaccharides_T.html?id=_JvkmQEACAAJ (accessed April 19, 2017).

[123] C. Brumaud, R. Baumann, M. Schmitz, M. Radler, N. Roussel, Cellulose ethers and yield stress of cement pastes, Cem. Concr. Res. 55 (2014) 14–21. doi:10.1016/j.cemconres.2013.06.013.

[124] J.-Y. Petit, K.H. Khayat, E. Wirquin, Coupled effect of time and temperature on variations of yield value of highly flowable mortar, Cem. Concr. Res. 36 (2006) 832–841. doi:10.1016/j.cemconres.2005.11.001.

[125] S. Rashid, P. Barnes, J. Bensted, X. Turrillas, Conversion of calcium aluminate cement hydrates re-examined with synchrotron energy-dispersive diffraction, J. Mater. Sci. Lett. 13 (1994) 1232–1234. doi:10.1007/BF00270944.

[126] C. Evju, S. Hansen, Expansive properties of ettringite in a mixture of calcium aluminate cement, Portland cement and β-calcium sulfate hemihydrate, Cem. Concr. Res. 31 (2001) 257–261. doi:10.1016/S0008-8846(00)00495-6.

[127] S.M. Clark, P. Barnes, A comparison of laboratory, synchrotron and neutron diffraction for the real time study of cement hydration, Cem. Concr. Res. 25 (1995) 639–646. doi:10.1016/0008-8846(95)00052-E.

[128] M. Merlini, G. Artioli, C. Meneghini, T. Cerulli, A. Bravo, F. Cella, The early hydration and the set of Portland cements: In situ X-ray powder diffraction studies, Powder Diffr. 22 (2007) 201–208. doi:10.1154/1.2754713.

[129] H.J. Weyer, I. Müller, B. Schmitt, D. Bosbach, A. Putnis, Time-resolved monitoring of cement hydration: Influence of cellulose ethers on hydration kinetics, Nucl. Instruments Methods Phys.

Res. Sect. B Beam Interact. with Mater. Atoms. 238 (2005) 102–106. doi:10.1016/J.NIMB.2005.06.026.

[130] P.J. Williams, J.J. Biernacki, C.J. Rawn, L. Walker, J. Bai, Microanalytical and Computational Analysis of Class F Fly Ash, ACI Mater. J. 102 (2005) 330–337. doi:10.14359/14712.

[131] R. Snellings, G. Mertens, Ö. Cizer, J. Elsen, Early age hydration and pozzolanic reaction in natural zeolite blended cements: Reaction kinetics and products by in situ synchrotron X-ray powder diffraction, Cem. Concr. Res. 40 (2010) 1704–1713. doi:10.1016/J.CEMCONRES.2010.08.012.

[132] J.E. Oh, P.J.M. Monteiro, S.S. Jun, S. Choi, S.M. Clark, The evolution of strength and crystalline phases for alkali-activated ground blast furnace slag and fly ash-based geopolymers, Cem. Concr. Res. 40 (2010) 189–196. doi:10.1016/J.CEMCONRES.2009.10.010.

[133] A.C. Jupe, A.P. Wilkinson, K. Luke, G.P. Funkhouser, Class H cement hydration at 180 °C and high pressure in the presence of added silica, Cem. Concr. Res. 38 (2008) 660–666. doi:10.1016/j.cemconres.2007.12.004.

[134] S.L. Colston, P. Barnes, A.C. Jupe, S.D.M. Jacques, C. Hall, P. Livesey, J. Dransfield, N. Meller, G.C. Maitland, An in situ synchrotron energy-dispersive diffraction study of the hydration of oilwell cement systems under high temperature/autoclave conditions up to 130 °C, Cem. Concr. Res. 35 (2005) 2223–2232. doi:10.1016/j.cemconres.2004.09.005.

[135] A.C. Jupe, A.P. Wilkinson, G.P. Funkhouser, Simultaneous study of mechanical property development and early hydration chemistry in Portland cement slurries using X-ray diffraction and ultrasound reflection, Cem. Concr. Res. 42 (2012) 1166–1173. doi:10.1016/J.CEMCONRES.2012.05.013.

[136] A.C. Jupe, A.P. Wilkinson, K. Luke, G.P. Funkhouser, Class H oil well cement hydration at elevated temperatures in the presence of retarding agents: An in situ high-energy X-ray diffraction study, Ind. Eng. Chem. Res. 44 (2005) 5579–5584. doi:10.1021/ie049085t.

[137] A.C. Jupe, A.P. Wilkinson, K. Luke, G.P. Funkhouser, Slurry Consistency and In Situ Synchrotron X-Ray Diffraction During the Early Hydration of Portland Cements With Calcium

Chloride, J. Am. Ceram. Soc. 90 (2007) 2595–2602. doi:10.1111/j.1551-2916.2007.01806.x.

[138] A.C. Jupe, A.P. Wilkinson, G.P. Funkhouser, Oil-Well Cement and C3S Hydration Under High Pressure as Seen by In Situ X-Ray Diffraction, Temperatures ≤80°C with No Additives, J. Am. Ceram. Soc. 94 (2011) 1591–1597. doi:10.1111/j.1551-2916.2010.04284.x.

[139] X. Pang, W. Cuello Jimenez, B.J. Iverson, Hydration kinetics modeling of the effect of curing temperature and pressure on the heat evolution of oil well cement, Cem. Concr. Res. 54 (2013) 69–76. doi:10.1016/j.cemconres.2013.08.014.

[140] X. Pang, C. Meyer, R. Darbe, G.P. Funkhouser, Modeling the Effect of Curing Temperature and Pressure on Cement Hydration Kinetics, ACI Mater. J. 110 (2013) 137–148. doi:10.14359/51685528.

[141] F. Sanchez, K. Sobolev, Nanotechnology in concrete – A review, Constr. Build. Mater. 24 (2010) 2060–2071. doi:10.1016/j.conbuildmat.2010.03.014.

[142] P. Hou, X. Cheng, J. Qian, R. Zhang, W. Cao, S.P. Shah, Characteristics of surface-treatment of nano-SiO2 on the transport properties of hardened cement pastes with different water-to-cement ratios, Cem. Concr. Compos. 55 (2015) 26–33. doi:10.1016/J.CEMCONCOMP.2014.07.022.

[143] J. Chen, S. Kou, C. Poon, Photocatalytic cement-based materials: Comparison of nitrogen oxides and toluene removal potentials and evaluation of self-cleaning performance, Build. Environ. 46 (2011) 1827–1833. doi:10.1016/J.BUILDENV.2011.03.004.

[144] B. Han, X. Yu, E. Kwon, A self-sensing carbon nanotube/cement composite for traffic monitoring, Nanotechnology. 20 (2009) 445501. doi:10.1088/0957-4484/20/44/445501.

[145] X. Yu, E. Kwon, A carbon nanotube/cement composite with piezoresistive properties, Smart Mater. Struct. 18 (2009) 055010. doi:10.1088/0964-1726/18/5/055010.

[146] F. Azhari, N. Banthia, Cement-based sensors with carbon fibers and carbon nanotubes for piezoresistive sensing, Cem. Concr. Compos. 34 (2012) 866–873. doi:10.1016/J.CEMCONCOMP.2012.04.007.

[147] G. Land, D. Stephan, The influence of nano-silica on the hydration of ordinary Portland cement, J.

Mater. Sci. 47 (2012) 1011–1017. doi:10.1007/s10853-011-5881-1.

[148] T. Sato, F. Diallo, Seeding Effect of Nano-CaCO 3 on the Hydration of Tricalcium Silicate, Transp. Res. Rec. J. Transp. Res. Board. 2141 (2010) 61–67. doi:10.3141/2141-11.

[149] J.J. Thomas, H.M. Jennings, J.J. Chen, Influence of Nucleation Seeding on the Hydration Mechanisms of Tricalcium Silicate and Cement, J. Phys. Chem. C. 113 (2009) 4327–4334. doi:10.1021/jp809811w.

[150] and S.P.S. Bekir Yilmaz Pekmezci, Thomas Voigt, Kejin Wang, Low Compaction Energy Concrete for Improved Slipform Casting of Concrete Pavements, ACI Mater. J. (2007) 104(3), 251-258. http://search.proquest.com/docview/197939265/abstract/492F76830ED64E87PQ/1?accountid=10226 (accessed May 20, 2015).

[151] N. Garg, K. Wang, Comparing the performance of different commercial clays in fly ash-modified mortars, J. Sustain. Cem. Mater. 1 (2012) 111–125. doi:10.1080/21650373.2012.745217.

[152] X. Gao, S. Kawashima, X. Liu, S.P. Shah, Influence of clays on the shrinkage and cracking tendency of SCC, Cem. Concr. Compos. 34 (2012) 478–485. doi:10.1016/J.CEMCONCOMP.2012.01.002.

[153] Y. Wang, T. Uchida, F. Westferro, M.L. Rivers, N. Nishiyama, J. Gebhardt, C.E. Lesher, S.R. Sutton, High-pressure x-ray tomography microscope: Synchrotron computed microtomography at high pressure and temperature, Rev. Sci. Instrum. 76 (2005) 073709. doi:10.1063/1.1979477.

[154] Y. Wang, W.B. Durham, I.C. Getting, D.J. Weidner, The deformation-DIA: A new apparatus for high temperature triaxial deformation to pressures up to 15 GPa, Rev. Sci. Instrum. 74 (2003) 3002–3011. doi:10.1063/1.1570948.

[155] J.M. Brown, The NaCl pressure standard, J. Appl. Phys. 86 (1999) 5801. doi:10.1063/1.371596.

[156] A.P. Hammersley, S.O. Svensson, M. Hanfland, A.N. Fitch, D. Hausermann, Two-dimensional detector software: From real detector to idealised image or two-theta scan, High Press. Res. 14 (1996) 235–248. doi:10.1080/08957959608201408.

[157] K. Luke, F.P. Glasser, Chemical Changes Occurring During the Early Hydration of PFA-OPC Mixtures, MRS Proc. 65 (1985) 173. doi:10.1557/PROC-65-173.

[158] H.F.W. Taylor, Cement chemistry, 1997.

[159] N. Meller, K. Kyritsis, C. Hall, The hydrothermal decomposition of calcium monosulfoaluminate 14-hydrate to katoite hydrogarnet and β-anhydrite: An in-situ synchrotron X-ray diffraction study, J. Solid State Chem. 182 (2009) 2743–2747. doi:10.1016/j.jssc.2009.07.029.

[160] P. Barnes, J. Bensted, Structure and Performance of Cements, Second Edition, CRC Press, 2002. https://books.google.com/books/about/Structure_and_Performance_of_Cements_Sec.html?id=6wPpkyrWE5oC&pgis=1 (accessed September 2, 2015).

[161] M.S. Konsta-Gdoutos, Z.S. Metaxa, S.P. Shah, Highly dispersed carbon nanotube reinforced cement based materials, Cem. Concr. Res. 40 (2010) 1052–1059. doi:10.1016/j.cemconres.2010.02.015.

[162] M.S. Konsta-Gdoutos, C.A. Aza, Self sensing carbon nanotube (CNT) and nanofiber (CNF) cementitious composites for real time damage assessment in smart structures, Cem. Concr. Compos. 53 (2014) 162–169. doi:10.1016/j.cemconcomp.2014.07.003.

[163] B.S. Sindu, S. Sasmal, S. Gopinath, A multi-scale approach for evaluating the mechanical characteristics of carbon nanotube incorporated cementitious composites, Constr. Build. Mater. 50 (2014) 317–327. doi:10.1016/j.conbuildmat.2013.09.053.

[164] R. Siddique, A. Mehta, Effect of carbon nanotubes on properties of cement mortars, Constr. Build. Mater. 50 (2014) 116–129. doi:10.1016/j.conbuildmat.2013.09.019.

[165] I. Mehdipour, A. Kumar, K.H. Khayat, Rheology, hydration, and strength evolution of interground limestone cement containing PCE dispersant and high volume supplementary cementitious materials, Mater. Des. 127 (2017) 54–66. doi:10.1016/j.matdes.2017.04.061.

[166] K.H. Khayat, A. Yahia, M. Sayed, Effect of Supplementary Cementitious Materials on Rheological Properties, Bleeding, and Strength of Structural Grout, ACI Mater. J. 105 (2008) 585–593. doi:10.14359/20200.

[167] S. Sadati, K.H. Khayat, Rheological and hardened properties of mortar incorporating high-volume ground glass fiber, Constr. Build. Mater. 152 (2017) 978–989. doi:10.1016/j.conbuildmat.2017.07.065.

[168] K. Vance, A. Kumar, G. Sant, N. Neithalath, The rheological properties of ternary binders containing Portland cement, limestone, and metakaolin or fly ash, Cem. Concr. Res. 52 (2013) 196–207. doi:10.1016/j.cemconres.2013.07.007.

[169] O. Boukendakdji, E.-H. Kadri, S. Kenai, Effects of granulated blast furnace slag and superplasticizer type on the fresh properties and compressive strength of self-compacting concrete, Cem. Concr. Compos. 34 (2012) 583–590. doi:10.1016/j.cemconcomp.2011.08.013.

[170] M. Adjoudj, K. Ezziane, E.H. Kadri, T.-T. Ngo, A. Kaci, Evaluation of rheological parameters of mortar containing various amounts of mineral addition with polycarboxylate superplasticizer, Constr. Build. Mater. 70 (2014) 549–559. doi:10.1016/j.conbuildmat.2014.07.111.

[171] A. Kashani, R. San Nicolas, G.G. Qiao, J.S.J. van Deventer, J.L. Provis, Modelling the yield stress of ternary cement–slag–fly ash pastes based on particle size distribution, Powder Technol. 266 (2014) 203–209. doi:10.1016/j.powtec.2014.06.041.

[172] C.K. Park, M.H. Noh, T.H. Park, Rheological properties of cementitious materials containing mineral admixtures, Cem. Concr. Res. 35 (2005) 842–849. doi:10.1016/j.cemconres.2004.11.002.

[173] A.I. Laskar, S. Talukdar, Rheological behavior of high performance concrete with mineral admixtures and their blending, Constr. Build. Mater. 22 (2008) 2345–2354. doi:10.1016/j.conbuildmat.2007.10.004.

[174] P. Hou, S. Kawashima, K. Wang, D.J. Corr, J. Qian, S.P. Shah, Effects of colloidal nanosilica on rheological and mechanical properties of fly ash–cement mortar, Cem. Concr. Compos. 35 (2013) 12–22. doi:10.1016/j.cemconcomp.2012.08.027.

[175] B. Lothenbach, K. Scrivener, R.D. Hooton, Supplementary cementitious materials, Cem. Concr. Res. 41 (2011) 1244–1256. doi:10.1016/j.cemconres.2010.12.001.

[176] ASTM C989/C989M, Standard Specification for Slag Cement for Use in Concrete and Mortars,

(2017). doi:10.1520/C0989_C0989M-17.

[177] R. Hamzaoui, A. Bennabi, S. Guessasma, R. Khelifa, N. Leklou, Optimal Carbon Nanotubes Concentration Incorporated in Mortar and Concrete, Adv. Mater. Res. 587 (2012) 107–110. doi:10.4028/www.scientific.net/AMR.587.107.

[178] M.S. Konsta-Gdoutos, Z.S. Metaxa, S.P. Shah, Multi-scale mechanical and fracture characteristics and early-age strain capacity of high performance carbon nanotube/cement nanocomposites, Cem. Concr. Compos. 32 (2010) 110–115. doi:10.1016/j.cemconcomp.2009.10.007.

[179] S. Mansoutre, P. Colombet, H. Van Damme, Water retention and granular rheological behavior of fresh C3S paste as a function of concentration11This paper was originally submitted to Advanced Cement Based Materials. It was received at the Editorial Office of Cement and Concrete Research on 27 Augu, Cem. Concr. Res. 29 (1999) 1441–1453. doi:10.1016/S0008-8846(99)00129-5.

[180] D.P. Bentz, C.F. Ferraris, M.A. Galler, A.S. Hansen, J.M. Guynn, Influence of particle size distributions on yield stress and viscosity of cement–fly ash pastes, Cem. Concr. Res. 42 (2012) 404–409. doi:10.1016/j.cemconres.2011.11.006.

[181] A. Zingg, F. Winnefeld, L. Holzer, J. Pakusch, S. Becker, L. Gauckler, Adsorption of polyelectrolytes and its influence on the rheology, zeta potential, and microstructure of various cement and hydrate phases, J. Colloid Interface Sci. 323 (2008) 301–312. doi:10.1016/j.jcis.2008.04.052.

[182] P. Coussot, Yield stress fluid flows: A review of experimental data, J. Nonnewton. Fluid Mech. 211 (2014) 31–49. doi:10.1016/j.jnnfm.2014.05.006.

[183] Q. Barral, G. Ovarlez, X. Chateau, J. Boujlel, B. Rabideau, P. Coussot, Adhesion of yield stress fluids, Soft Matter. (2010) 1343–1351. doi:10.1039/b922162j.

[184] ASTM C109 / C109M - 16a, Standard Test Method for Compressive Strength of Hydraulic Cement Mortars, 2016. doi:10.1520/C0109_C0109M-16A.

[185] AASHTO T 132-87, Standard Method of Test for Tensile Strength of Hydraulic Cement Mortars, 2013. http://www.techstreet.com/standards/aashto-t-132-87-2013?product_id=1320947 (accessed

September 1, 2017).

[186] E.E. Gdoutos, M.S. Konsta-Gdoutos, P.A. Danoglidis, Portland cement mortar nanocomposites at low carbon nanotube and carbon nanofiber content: A fracture mechanics experimental study, Cem. Concr. Compos. 70 (2016) 110–118. doi:10.1016/J.CEMCONCOMP.2016.03.010.

[187] A. Chaipanich, T. Nochaiya, W. Wongkeo, P. Torkittikul, Compressive strength and microstructure of carbon nanotubes–fly ash cement composites, Mater. Sci. Eng. A. 527 (2010) 1063–1067. doi:10.1016/J.MSEA.2009.09.039.

[188] Y. Qian, S. Kawashima, Flow onset of fresh mortars in rheometers: Contribution of paste deflocculation and sand particle migration, Cem. Concr. Res. 90 (2016) 97–103. doi:10.1016/j.cemconres.2016.09.006.

[189] S.W. Tang, X.H. Cai, Z. He, W. Zhou, H.Y. Shao, Z.J. Li, T. Wu, E. Chen, The review of early hydration of cement-based materials by electrical methods, Constr. Build. Mater. 146 (2017) 15–29. doi:10.1016/j.conbuildmat.2017.04.073.

[190] R. Spragg, C. Villani, K. Snyder, D. Bentz, J. Bullard, J. Weiss, Factors That Influence Electrical Resistivity Measurements in Cementitious Systems, Transp. Res. Rec. J. Transp. Res. Board. 2342 (2013) 90–98. doi:10.3141/2342-11.

[191] R.K. Abu Al-Rub, B.M. Tyson, A. Yazdanbakhsh, Z. Grasley, Mechanical Properties of Nanocomposite Cement Incorporating Surface-Treated and Untreated Carbon Nanotubes and Carbon Nanofibers, J. Nanomechanics Micromechanics. 2 (2012) 1–6. doi:10.1061/(ASCE)NM.2153-5477.0000041.

[192] B.M. Tyson, R.K. Abu Al-Rub, A. Yazdanbakhsh, Z. Grasley, Carbon Nanotubes and Carbon Nanofibers for Enhancing the Mechanical Properties of Nanocomposite Cementitious Materials, J. Mater. Civ. Eng. 23 (2011) 1028–1035. doi:10.1061/(ASCE)MT.1943-5533.0000266.